Development and Experimental Characterization of Ultrasonic Phased Arrays for Nondestructive Evaluation

by

Arthur C. Clay

Submitted to the Department of Civil and Environmental Engineering
in partial fulfillment of the requirements for the degree of

Master of Science in Civil and Environmental Engineering

at the

MASSACHUSETTS INSTITUTE OF TECHNOLOGY

February 1998

Author . . . .
Department of Civil and Environmental Engineering
January 23, 1998

Certified by . . . .
Shi-Chang Wooh
Assistant Professor of Civil and Environmental Engineering
Thesis Supervisor

Accepted by . . . .
Joseph M. Sussman
Chairman, Departmental Committee on Graduate Students

Development and Experimental Characterization of Ultrasonic Phased Arrays for Nondestructive Evaluation

by

Arthur C. Clay

Submitted to the Department of Civil and Environmental Engineering
on January 23, 1998, in partial fulfillment of the
requirements for the degree of
Master of Science in Civil and Environmental Engineering

Abstract

The application of phased arrays to solid materials (as opposed to tissue) is extremely challenging because of mode conversion, complex geometry, varying material properties and increased wave speed. For NDE applications, particularly civil infrastructure, one is primarily interested in having a well defined and directed beam with good steerability to accurately locate defects. Since the effect of certain key phased array parameters on the wave propagation behavior in solid media has not been experimentally characterized, the most important prerequisite for applying these sensors to infrastructure is to develop a system which can be used to calibrate and assess the beam steering performance of the sensor.

A solid platform for this research has been developed by the author with the following objectives in mind:

- to design and develop a prototype phased array system, including hardware, and transducer
- to develop a calibrating device whereby the behavior of the phased array may be characterized and assessed for performance
- to verify experimentally an optimum parameter configuration for phased array steering based on a theoretical model

Several transducers were fabricated and tested with various combinations of active elements, interelement spacings and steering angles. The experimental directivities showed good agreement with the theoretical prediction in terms of steerability and main lobe width. It was also proven that increasing number of elements improved the beam directivity as did an increase in spacing up to approximately a half wavelength.

Thesis Supervisor: Shi-Chang Wooh
Title: Assistant Professor of Civil and Environmental Engineering

Acknowledgments

Prof. Shi-Chang Wooh deserves a standing ovation for an absolutely spectacular five-star performance as my thesis advisor. I would like to express my sincere appreciation for his guidance, encouragement, enthusiasm and everlasting confidence in me. He has had a tremendously positive impact on my life and is truly the most inspiring and influential person I have ever met.

My parents have been incredibly supportive, particularly during the numerous stumbling blocks I encountered during my research. They never gave up hope in me and always urged me onward. I am very thankful for their confidence and belief in me.

I gratefully credit Lawrence Azar for his active participation and contribution to my research. He selflessly sacrificed many days and nights to help me acquire data and fabricate sensors. He also helped tackle some major obstacles along the way. I am extremely appreciative for his phased array numerical simulation program which is used in the results section of the thesis.

Working with Kecheng "Coach" Wei on this project has been a rewarding and enjoyable experience. He is a great friend, not to mention a very talented computer programmer. I would like to thank Coach for his assistance in designing the pulser circuitry as well as his motor control and data acquisition program.

My other team member, Yijun Shi, provided a useful model for predicting the theoretical pressure distribution of the phased array. His study of the various phased array parameters helped provide the basis and direction of my research. His work has certainly helped to consummate this thesis.

Ji-yong Wang also put in a big effort to assist in sensor fabrication. I am especially grateful for his participation since he was also working hard to meet a thesis deadline.

Stephen Rudolph richly deserves kudos for his expert craftsmanship and machining skills. I appreciate the timeliness of delivery and professional appearance of the various components that he assembled. I am also grateful for his advice on various practical issues such as experimental setups and design details.

A 1975 alumnus of MIT, Stephen Chapman has been incredibly helpful during my three years here in the Boston area. As my "campus connection", I have benefited enormously from his insight and practical advice regarding many important issues lying outside of my research.

I am also thankful for the sponsorship from the Korea Highway Corporation. I enjoyed collaborating with the Project Manager, Dr. Chang-Guen Lee, during his visits to the U.S.

Finally, I would like to extend thanks and appreciation to all my friends who helped make my experience all the more memorable here at MIT, especially Gerry Grippo, Jeff Roth, Marc Carlin, Oguz Gunes, Brian Hearing, Katie Adams, Andrew Walsh, Yong-Tae "Phil" Yoon, Casey Kim and Karen Veroy. In one way or another, they helped me get through it all.

Biographical Note

The author received his Bachelor's Degree from Bucknell University, Lewisburg, PA, where he majored in Civil Engineering (1989-1993). Afterwards, he earned an advanced degree at the Massachusetts Institute of Technology (1994–1998). While pursuing the Master's Degree, he was actively involved in competitive cycling with the MIT Cycling Team. He also held positions at the Institute as Teaching Assistant and Graduate Researcher. Outside of MIT, he held part time work for Summit Education (Wellesley, MA) as a private tutor, and for the Smith Group (Cambridge, MA) as a publication assistant.

His academic interests include experimental and theoretical ultrasonic NDE, structural analysis and control, steel and concrete design and behavior of construction materials. He is a member of the Tau Beta Pi National Academic Honor Society. In his spare time, the author enjoys competitive cycling, traveling and skiing. The author is formerly from Glen Ridge, NJ and currently resides in Framingham, MA. Mr. Clay is currently working at R/D Tech, located in Waltham, MA, where he is responsible for applications, probe development, and support of commercial phased array systems. Following is a current list of publications.

1. S. C. Wooh, A. Clay and C. Wei, "Ultrasonic phased array transducers for nondestructive evaluation of steel structures," *SEM Spring Conference,* Bellevue, WA, June 1997.

2. S. C. Wooh and A. Clay, "High-speed monitoring of surface defects in rail tracks using ultrasonic Doppler effect," *Review of Progress in Quantitative Nondestructive Evaluation,* D. O. Thompson and D. E. Chimenti eds., Plenum Press, New York, 1997.

3. S. C. Wooh, C. Wei and A. Clay, "Short-time Fourier transform of continuous wave Doppler signals," *Materials Research Society*, 1997 Fall Conference, Boston, MA, December 1997.

4. S. C. Wooh, A. Clay, Y. Shi and C. Wei, "Development of ultrasonic sensors

for nondestructive evaluation of fracture critical steel bridges," interim report submitted to *The Korea Highway Corporation*, December 1996.

5. S. C. Wooh and A. Clay, "Potential applications of ultrasonic NDE methods for rail condition assessment," working paper 96-4, submitted to the *Association of American Railroads*, December 1996.
6. A. C. Clay, S. C. Wooh and L. Azar, "Ultrasonic beam steerability and directivity for linear phased arrays," to be submitted to the *Journal of Nondestructive Evaluation.*
7. S. C. Wooh, A. Clay, and C. Wei, "Doppler-based ultrasound for detection of surface discontinuities on a rapidly moving object," to be submitted to *Research in Nondestructive Evaluation.*

Contents

List of Figures

List of Tables

Chapter 1

Introduction

This chapter provides the background for the thesis by addressing the problems encountered in aging materials and infrastructure. The emphasis is placed on the motivation for nondestructive evaluation (NDE), which is the governing body of techniques and principles used to examine materials, components and structures in order to ascertain their usefulness without inducing damage. For completeness, a brief review of the principles, merits and limitations of the state of the art NDE techniques is included. The focus will then shift to ultrasonic testing methods, examining the motivation for extensive research and development in this area. As an alternative to the traditional ultrasonic techniques, the rationale for investigating ultrasonic phased array sensors in long-distance NDE applications will be presented. The final section contains a synopsis of the thesis structure.

1.1 The Role of NDE in Civil Infrastructure

In an age where civil infrastructure is tantamount to the vitality of our nation, the demand for accurate and reliable methods of assessment plays an increasingly important role. The application of NDE as a tool in detecting, locating and monitoring damage cannot be emphasized enough. Without it, proper repair and rehabilitation or closure of suspect areas would go unnoticed, possibly leading to disaster. At the same time, accurate sizing of internal and external damage is important to avoid the economic penalty of scrapping otherwise structurally safe components and to minimize the risk of failure of apparently sound ones.

By definition, civil infrastructure (CIS) includes all industrial and public mass transportation infrastructure (such as highways, railways, bridges, airports, subways and mass transit systems), buildings and structures of all kind, telecommunication facilities, chemical and power plants, and so on. Unfortunately, many of the CIS are aging and exhibiting various stages of decay and sometimes, failure. For example, it has been estimated that over 40% of the nation's bridges have been classified as structurally deficient or functionally obsolete (USDOT, 1985).

Most of the deterioration and decay is a result of damage to the structure. The severity and extent of damage provides a measure of the structural integrity. Even before its final assembly and service life, there are many potential sources triggering the eventual demise of the structure. Improper design specifications, such as sharp changes in member geometry, for example, can create high stress concentrations. The individual components and members of the structure often contain inherent flaws due to raw material impurities and foreign inclusions. During the fabrication and erection process, additional flaws may appear as a result of careless handling or improper welding and fastening of structural members. Consequently, quality assurance and control (QA/QC) is a key issue in detecting flaws that have been introduced during the manufacturing and production process. In Table 1.1, a summary of the common sources of flaws, triggering damage both before and after the useful service life of a structure, is provided.

During the service life of the structure, service-induced damage will inevitably exacerbate any flaws that are present up to this point. Structural fatigue due to cyclic loading will inevitably produce cracks. Corrosion may severely weaken a member since the effective area is reduced, diminishing its useful strength. The coupling of excessive stress in a corrosive environment results in an accelerated stress-corrosion cracking, often leading to collapse or failure. Dynamic and impact loading can cause severe warping, bending or buckling. The net result is that infrastructure deteriorates with time, mostly resulting from the aging of the materials, excessive use, overloading,

Category	Process	Flaw type
Inherent flaws	material production	raw material impurities foreign inclusions density variation
Fabrication	rolling	change in thickness
	sintering	porosity
	curing	porosity, non-uniform areas
	welding	voids, porosity
	adhesive bonds	debonding, delamination
	erection/handling	foreign inclusions
Service life	fatigue	cracking
	impact	deformation, cracking, breakage
	corrosion	dimensional loss
	stress-induced corrosion	accelerated stress-corrosion cracking

Table 1.1: Flaws resulting from various processes in civil infrastructure.

climate and environmental conditions, lack of sufficient maintenance, and lack of proper inspection methods. All of these factors contribute to the obsolescence of the structural system as a whole.

The failure of a structure is often initiated from a crack-like defect and is large enough to cause a major reduction in strength. Elementary principles of fracture mechanics may be used to predict the so-called critical crack size (Charlesworth and Temple, 1989):

$$a_c = \frac{2WE}{\pi\sigma^2} \tag{1.1}$$

where a_c is the theoretical critical crack size, W is the work of fracture of the solid, E is the elastic modulus, and σ is the applied stress. The most severe defect is usually one that is oriented perpendicular to the principal applied stresses; the critical defect parameter is its through-wall extent. Accurate and reliable measurement of this parameter is of great importance in ensuring the structural integrity of many components. Upon locating and characterizing such defects, repair, retrofit, rehabilitation, and replacement become necessary actions to be considered in order to ensure the safety of the public (Scalzi *et al.*, 1990).

In order to safeguard against these failures, many state and federal administrations mandate routine facility maintenance and inspection programs. Figure 1.1 illustrates the ideal life cycle of a structure and the role of NDE in its maintenance. During and after the construction of a facility, an immediate inspection of the material and connection members should be followed to ensure the design strength of the structure. Furthermore, the structural condition should be monitored during service life, followed by detailed inspection to address the problems and identify the needs for repair or replacement. Consequently, a significant amount of government funding is directed toward advancing the technology associated with structural maintenance, aiming to provide accurate information for intelligent decision making.

1.2 State of the Art NDE Techniques

Having described the mechanisms which cause damage as well as the need for NDE in order to safeguard against failure, it is fitting to provide a brief and general review of some of the common methods available which are useful in identifying, locating, and characterizing structural damage and defects. Although the methods presented are capable of characterizing a wide range of defect sizes with varying degrees of sensitivity, it should be emphasized that no single method is suitable for all possible applications. For completeness, several key references are included, which address the current research issues.

A general classification of all the techniques applied today would be difficult to assemble since they all share common traits, advantages and limitations. Nonetheless, the following list includes the mainstream inspection and monitoring methods currently employed, based primarily on the physical principle of operation:

- Visual/Optical Testing (VT)
- Liquid Penetrant Testing (PT)
- Magnetic Particle Inspection (MPI)
- Eddy Current (EC)

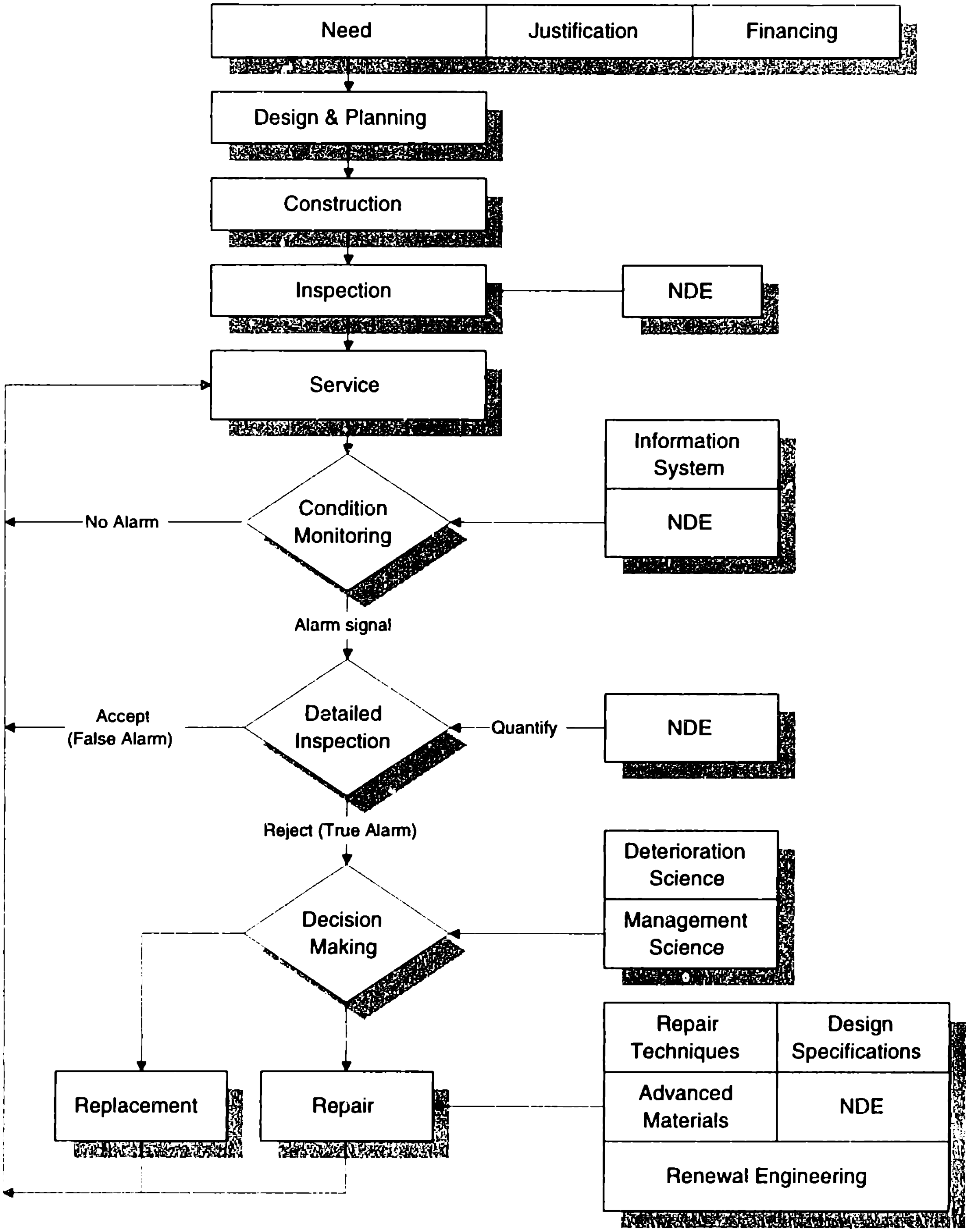

Figure 1.1: The role of NDE in the life-cycle of civil infrastructure (Wooh, 1995).

- Radiographic Testing (RT)
- Acoustic Emission (AE)
- Ultrasonic Testing (UT)

1.2.1 Visual and Optical Inspection

To some degree, all NDE methods require visual inspection as a first-cut assessment of the severity and type of damage in the structure. For this reason the unaided human eye is perhaps the most widely used of all techniques, discriminating a vast array of defects in various applications and often used to reinforce other methods, such as dye penetrant or magnetic particle. The experienced inspector will, for example, be able to detect the existence or absence of surface cracks, porosity, lack of penetration, undercutting, notches and misalignment in welds. The results are immediately obtainable, easy to interpret, and may by used to decide whether further NDE techniques are required.

The more sophisticated optical methods include holography and video enhancement. Holography is an image reconstruction technique based on the recording of a complete wavefront reflected from a surface so that all the information pertaining to the contact surface is retained and readily available for later retrieval. Rosenthal and Trolinger (1995) provide several application examples to NDT using holography, including defect detection, modal analysis, surface distortion and thermal expansion and distortion. Video enhancement enables remote monitoring of a structure thanks to the improved resolution of video cameras. Source detection systems enable imaging of heat, sonic, ultrasonic, and X-ray patterns. Computer interfacing allows for visual study and evaluation of information not previously detectable by traditional means.

1.2.2 Liquid Penetrant Testing

Liquid penetrant testing is used for detecting surface discontinuities such as cracks and porosity in solid materials and structures. The penetrant is drawn into very small openings by capillary action when it is applied to a surface. After sufficient dwell time, all of the remaining penetrant is removed, and a developer in dry powder or liquid form is applied to the surface. This developer absorbs residual penetrant drawn from discontinuities. Thus, a bright colored penetrant "bleeding" through the white background of the developer gives clear visual indications. Fluorescent penetrants offer a high contrast of bright yellow-green fluorescence against a dark background when viewed with black light in a darkened room.

Performed on most non-ferro-magnetic materials, penetrant inspection is most often used on materials clad in stainless steel, and stainless welded items. They are often used to detect cracks when other methods fail, but their application is limited to surface defects.

1.2.3 Magnetic Particle Inspection

One of the oldest and most widely used nondestructive testing methods, magnetic particle testing is useful for surface and subsurface flaw evaluation in ferromagnetic materials. The physical principle involves the distortion of a magnetic field due to a discontinuity in the material, resulting in a "leakage field" that extends beyond the surface of the material. Typically, a magnetic "yoke" is applied to the object being tested. The yoke is U-shaped, providing two contact points, and creating a magnetic field between the two thongs that are in contact with the object. With the yoke still attached to the object, a very fine dry ferromagnetic powder is applied to the area between the yoke's thongs, with some of them becoming magnetized and held in a high concentration at the discontinuity by the leakage field. To enhance the outline of the defect, fluorescent particles are often used. This is a relatively simple procedure. but does require experienced operators.

MPI is used to inspect items such as pressure vessels, weld-fabricated components, cast items, forged shafts, and barstocks. This method is particularly well suited for detecting cracks and defects open to the surface and within 0.25 in. (0.635 cm) of the surface. However, it cannot be used to detect interior damage.

1.2.4 Eddy Current

A general review of eddy current principles is given by Dufour *et al.* (1995). When an energized conducting coil is placed near the surface of a metallic material, eddy currents are induced in the material. These currents will be proportional to the electrical conductivity of the material. The current in the coil is AC, since relative motion between the field and the conductor is required to generate or induce electricity. The current induced in the metal flows in the opposite direction from the current in the coil. When current in the coil reverses direction, the induced current reverses. Material properties as well as discontinuities such as cracks or voids will affect the magnitude and phase of the induced current. Thus, with the aid of suitable instrumentation, eddy currents can be used to assess the material conditions.

A wide range of instrumentation is available for locating flaws in metallic materials. It is especially useful in rapid, automatic testing of tubing, wires, and large uniform surfaces. Manual testing is also practical for locating flaws and sorting materials according to electrical conductivity. McNab and Thomson (1995) describe a four by four multi-element eddy current array used for the local testing of ferritic specimens including welds. Thollon *et al.* (1995) discuss both the numerical and experimental results of an eddy current NDT system for the inspection of deep cracks under installed fasteners of aircraft structures. For the improvement of signal response, Dufour *et al.* (1995) use an active shielding technique for improved performance applied to the testing of graphite composite materials for aeronautics.

1.2.5 Radiographic Testing

X-radiography is essentially a two-dimensional shadow display or picture of the intensity distribution of X-rays that have passed through an object. The object attenuates radiation according to the mass, type and size of defects present. Thus, an intensity distribution of radiation that varies with flaw distribution is created. This radiation pattern can be made visible with photographic film, fluorescent screens, or digitized images displayed on television or computer screens. Because X-rays have very short wavelengths (0.1 nm to 0.1 μm), they can be used to assess the integrity of metallic and nonmetallic structures over a wide thickness range. X-rays are generated by high-velocity electrons striking a metallic target, which in flaw detection systems is usually tungsten embedded in copper. The target, along with the source of electrons and a means of accelerating them, is enclosed in a vacuum tube, which can be positioned as required to perform an inspection.

The advantage of radiography is that it is highly sensitive to changes in material properties. This is why X-rays are so common in medical imaging: the sharp contrast between tissue and bone due to their density variation will clearly indicate the location and extent of fracture.

In NDE, radiography is used to detect internal cracks, voids, porosity and inclusions in metallic materials as well as delamination and fracture in composites (in the latter case radio-opaque penetrants are required). X-Radiography, along with ultrasonics and magnetic particle inspection, is a mainstay in state of the art weld inspection. Ditchburn *et al.* (1996) summarize the general principles of radiography as well as its application to welded steel structures.

Although radiography interacts well with material properties and does not require contact with the test specimen, the bulkiness of the equipment limits its practical use in field inspections. The safety hazard of the high energy beams generated by the apparatus is another major problem since the testing area must be totally cleared out.

1.2.6 Acoustic Emission

The principles of this technology are based on transient mechanical vibration generated by the sudden and rapid release of energy from localized sources within materials. A stress or other stimulus is required to release or generate emissions. The detectable energy levels of these emissions can range from the motion of a few dislocations in metals to that required to cause impending failure due to cracking in structures.

The devices used in AE monitoring systems are typically passive. They can be designed to detect sounds produced by crack initiation or growth, chemical reactions such as corrosion, microdynamical events such as twinning, martensite phase transformations, vacancy coalescence, and dislocation breakaway from pinning points. Although AE sensors are unable to detect dormant cracks, they can be used, with adequate stimuli, to monitor material behavior, manufacturing processes and the structural integrity of pressure vessels and piping, as well as many other specialized applications.

A general review of acoustic emission is summarized by Sison *et al.* (1996). Their work relates to the application of AE sensors for monitoring of steel bridges. Berthelot *et al.* (1994) discuss a scheme for monitoring events in concrete based on the spectrum of the received signal. Their signal identification scheme takes into account the frequency response of the transducers as well as the wave attenuation in concrete as a function of frequency.

1.2.7 Ultrasonic Testing

Often associated with medical imaging and diagnostics, ultrasonic testing in the field of NDE is arguably the most robust and versatile method available. The majority of ultrasonic testing is based on the piezoelectric effect. Electrical pulses excite a piezoelectric material (transducer), generating stress waves which are emitted into an object at frequencies in the range of 30 kHz to 50 MHz, depending on the application. The interaction of these waves within the material will result in some portion of energy returned to a receiver and converted into electrical energy through an inverse piezoelectric effect.

When the return signals (known as A-scan waveforms) are monitored on an oscilloscope, the peaks will correspond to echos (reflections from a scatterer) and the space between the peaks provides the transit time. The literature shows that both the strength (amplitude) of the echo as well as the transit time (time-of-flight) are used extensively to characterize defects; Charlesworth and Temple (1989), Mak (1985), Doyle and Scala (1978), Ogura (1983), Achenbach *et al.* (1992).

One very attractive feature of ultrasound is its imaging capabilities. It is possible to display cross-sectional, planar and full volumetric images of virtually any conceivable material or component using immersion (underwater) testing. Intensity mapping of the received signals can qualitatively show defective regions. A large amount of literature covers various digital signal processing techniques and algorithms which use the information collected in the images to enhance the detail and resolution of defects; Schueler *et al.* (1984), Mak (1991), Hsu and Patton (1993), Wooh and Daniel (1994), Masnata and Sunseri (1996).

Widely used and relatively inexpensive, ultrasonic instrumentation is capable of detecting a wide range of surface, subsurface and internal defects of varying size and depth on many materials that have adequate inspection access and a sufficiently smooth testing surface. Ultrasonic techniques such as TOFD (Time-of-Flight Diffraction) have great accuracy, in many cases better than ±1 mm and have considerable capability for obtaining measurements in the wide range of material thicknesses encountered in engineering materials—up to 1 m in steel (Charlesworth and Temple, 1989).

Ultrasound is not limited to the detection of defects. Because stress waves interact naturally with material properties such as density (ρ) and elastic moduli (E and G), UT is also effective for material characterization, particularly composites; Wooh and Daniel (1991), Hsu *et al.* (1994).

Another awesome feature of UT is that it may be used either in direct contact or in a non-contact operational mode (i.e. through water or air) when testing solid materials. This is because all phases of matter support some form of elastic wave propagation. When ultrasound is coupled through air, it may be used to assess rough surfaces, or rapidly moving objects via the Doppler effect (Wooh and Clay, 1997). In an aqueous environment, ultrasound may scan enormous components having extremely complicated geometry by methods of contour following. Other non-contact methods include laser-based ultrasonics (LBU) and EMATs. They involve the localized thermoelastic (LBU) or electromagnetic (EMAT) generation of stress waves on the surface of an object and are therefore not piezoelectric in nature.

In light of these advantages, UT does have several drawbacks. A major consideration is the need of well-trained personnel who are skilled in calibrating the instrumentation and interpreting the return signals. Indeed, the inverse modeling techniques are not yet mature and operator experience is extremely critical in locating unknown defects. Also, the equipment can be somewhat bulky which may restrict access in the field.

Since ultrasonic NDE is the method applied in this work, the background theory of ultrasonic testing and imaging principles will be treated in greater detail in the following chapter.

1.3 Motivation and Rationale for Research in UT

Since this work is aimed for improved ultrasonic techniques and applications in civil infrastructure, the safety of the public may be considered to be the greatest motivational factor in this research. The rationale can be justified by one particular example of a documented structural failure which was followed by immediate and successful ultrasonic evaluation.

In June 1983, the collapse of a highway bridge on Interstate 95 in Greenwich, CT, resulted in three fatalities. Examination of the structure revealed cracking in a pin-hanger assembly, as shown in Fig. 1.2. The assembly comprises two pins and two hanger plates. The top pin is in a cantilever girder and the other is in a suspended girder connected by the two hanger plates.

After the catastrophe, the FHWA ruled that all fracture critical members[1] be tested ultrasonically. The method uses a straight beam transducer shown in Fig. 1.2 (bottom left) to transmit ultrasound and detect fractures that occur where the hanger plates bear against the pin. In addition, 5° angle beam transducers are used to enhance the reflection of outer diameter cracks and to avoid permissible cotter pin holes, as shown in Fig. 1.2 (bottom right). Angle beam tests also reveal small cracking or deterioration within the pin-hanger assembly.

---

[1] Fracture critical (FC) refers to those structures with primary members whose failure could result in collapse of the bridge. These members are subjected to tensile loads which cannot be transferred through alternate or redundant load paths.

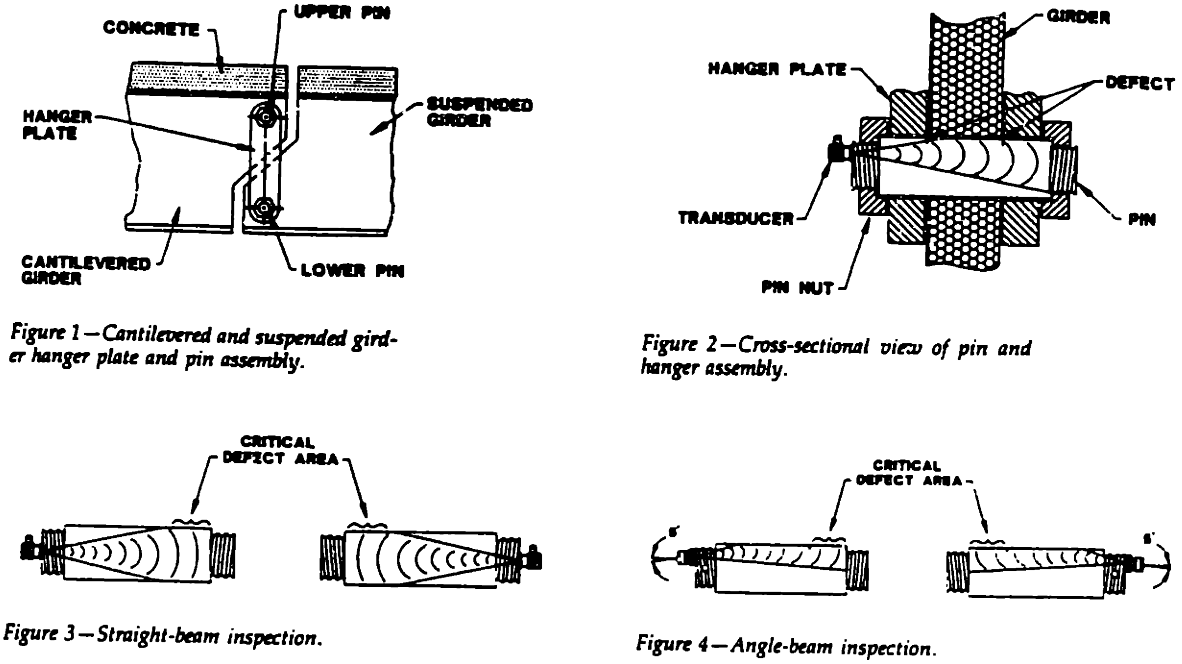

Figure 1—Cantilevered and suspended girder hanger plate and pin assembly.

Figure 2—Cross-sectional view of pin and hanger assembly.

Figure 3—Straight-beam inspection.

Figure 4—Angle-beam inspection.

Figure 1.2: The 1983 Interstate 95 highway bridge collapse: schematic of pin-hanger assembly (top) and current ultrasonic NDE method using straight and angle beam probes (bottom). (McCurdy, 1989)

This is but one of countless examples of quick, cost-effective and reliable ultrasonic inspection methods that have been adopted to safeguard from disaster. Many other ongoing applications are driven by the need to improve the quality of human lives through the assurance of structural integrity. Consequently, the pace of research and development in ultrasonic NDE is intense. This activity is further motivated by the need to establish higher performance standards, improve reliability, avoid human error through mechanization and automation, and even develop applications in hostile environments such as off-shore oil platforms and nuclear reactors.

1.4 Objectives and Approaches

Given the motivation for research in ultrasonic methods, there is a need to explore new areas for refinement and advancement. Indeed, ultrasonic testing at its current state does have some shortcomings in the area of infrastructure assessment.

Conventional ultrasonic probe inspection, as shown in Fig. 1.3(a) involves a single active element which can generate the ultrasound either at normal incidence or at oblique incidence into the material. The problem is that the operator is limited to a narrow field of view and should be extremely knowledgeable of the nature of the return signals. In addition, long structural members require back and forth manual scanning of the sensor or even step-by-step positioning which is cumbersome and time consuming. Since it is impossible to maintain uniform coupling conditions, the return echoes can be easily misinterpreted. Consequently, there is a huge demand for technological improvement in order to enhance the current status of infrastructure assessment.

One way to deal with these issues is to employ multielement sensors. Originally developed for radar and a staple in medical diagnostics and therapeutic treatment, phased arrays offer many advantages which can be used to overcome the difficulties encountered in conventional testing practices.

The chief feature of phased array sensors is their ability to steer and focus the ultrasonic beam in the material, as shown in Fig. 1.3(c). The advantages are clear

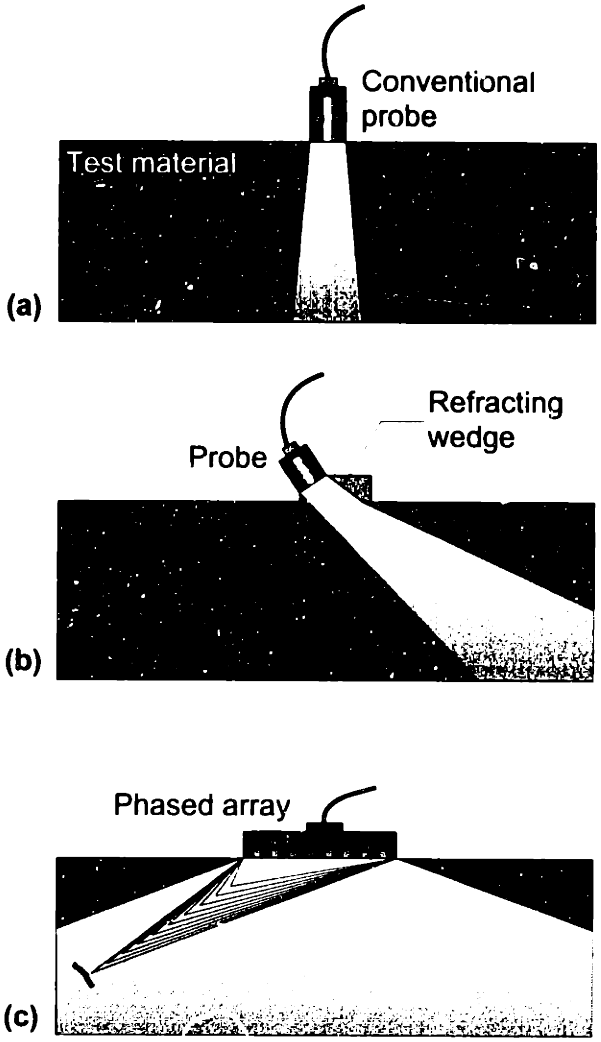

Figure 1.3: Conventional and proposed approaches in NDE: (a) single element straight beam probe, (b) angle wedge probe and (c) phased array (multielement probe).

and the potential applications are enormous. From a single fixed position, the beam can be swept like a searchlight from one end of the material to the other, pinpointing the location of cracks and flaws. This is a less labor intensive approach that may eventually lead to faster inspection times and more accurate assessment of the damage in the member.

The novelty and innovation of this research lies in the implementation of phased array sensors to be able to rapidly and accurately scan a vast spectrum of material defects. The application of phased arrays to solid materials (as opposed to tissue) is extremely challenging because of mode conversion, complex geometry, varying material properties and increased wave speed. Because little is known regarding the effect of certain key phased array parameters on the wave propagation behavior in solid media, the most important prerequisite for applying these sensors to infrastructure is to develop a system which can be used to calibrate and assess the beam steering performance of the sensor.

A solid platform for this research has been developed by the author with the following objectives in mind:

- to design and develop a prototype phased array system, including hardware, and transducer
- to develop a calibrating device whereby the behavior of the phased array may be characterized and assessed for performance
- to verify experimentally an optimum parameter configuration for phased array steering based on a theoretical model

The general approach used to carry out these objectives, showing the relationship between modeling and experimental work, is shown in Fig. 1.4. In this work, the objectives previously outlined provide a basis for understanding critical design parameters (discussed in Chapter 3) of the system. These parameters are explored in an analytical/numerical forward modeling investigation and, at the same time, they are used to develop a methodology for fabricating and integrating the system. The completed system must undergo extensive calibration in order to assess its performance and verify the validity of the results obtained from modeling. The feedback from this study will be used to refine and/or modify the design parameters as well as the fabrication technique.

A well calibrated system can immediately be extended to real applications. However, this is an area of study lying outside the scope of this thesis. It is an equally demanding task since inverse modeling techniques are required for quantitative characterization of material defects.

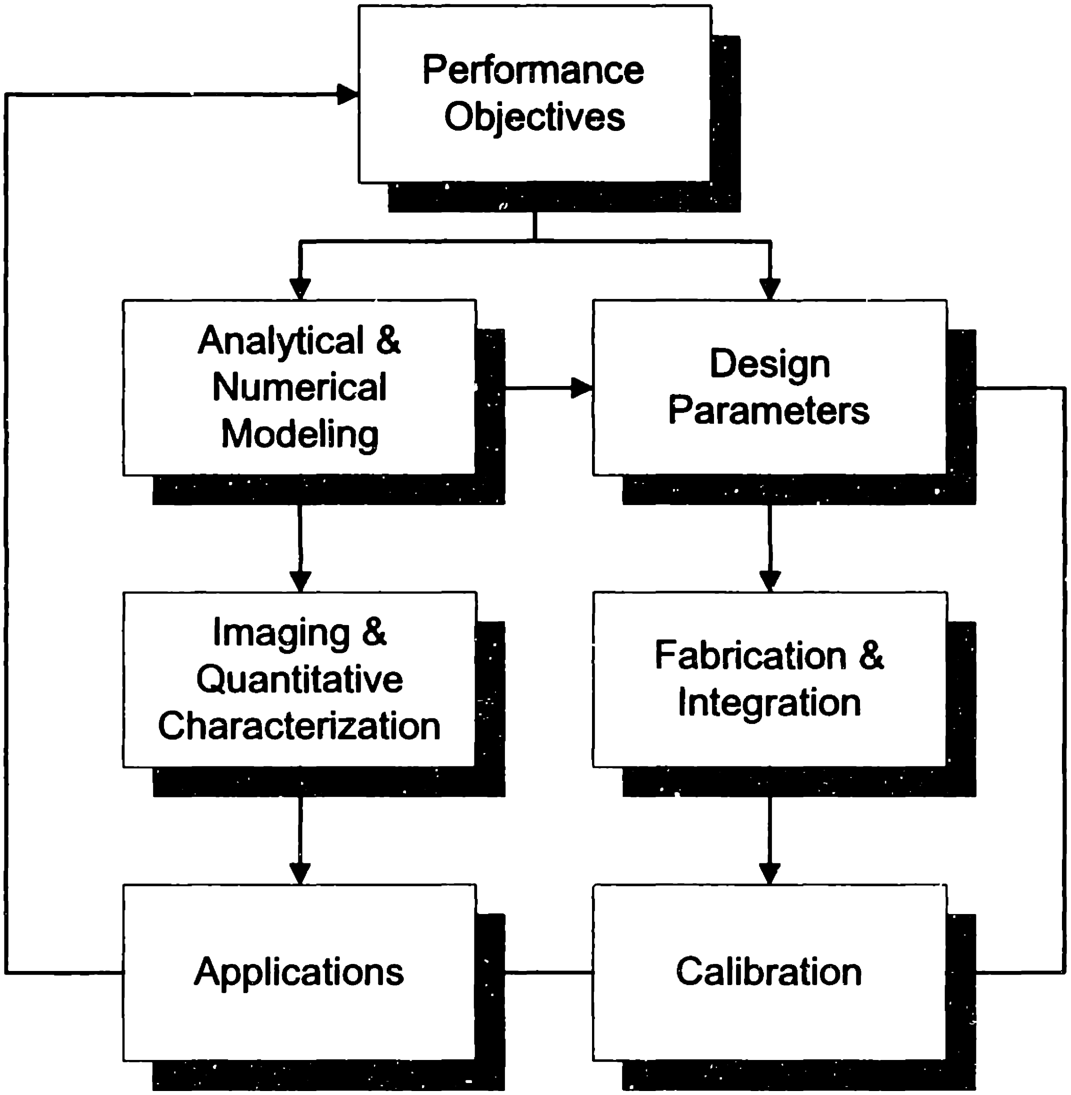

Figure 1.4: Approach to the phased array development, ultimately leading to various NDE applications in civil infrastructure.

1.5 Thesis Structure

This section provides a brief overview of the thesis structure and organization. The thesis itself is divided into six chapters:

- Chapter 1 introduces the thesis scope, along with the rationale and motivation for research in the nondestructive evaluation (NDE) of civil infrastructure systems (CIS).
- Chapter 2 provides the motivation, background, and basic principles of ultrasonic NDE as well as some general techniques used for detecting defects in structures.
- The first part of Chapter 3 focuses on the principles and applications of ultrasonic phased array transducers. The second part presents the background and results of the theoretical modeling of the pressure distribution, as well as the optimization of transducer parameters.
- Development of the prototype phased array system for NDE is presented in Chapter 4. This chapter will discuss the array design and fabrication, delay and pulser circuitry and computer interfacing.
- Chapter 5 presents the calibration platform used in this study. The experimental directivity patterns derived from the calibration will be compared with a numerical simulation based on the model discussed in Chapter 3.
- Chapter 6 will summarize the work performed. Important conclusions will be drawn and recommendations for future work and advancement in this study will be made.

Chapter 2

Ultrasonic NDE Principles and Methods

This chapter will discuss some fundamental background of ultrasonics as applied in the field of ultrasonic testing. These principles include basic wave propagation, sound field characteristics and behavior, and wave interaction at interfaces. Some of these concepts are germane to the theoretical development in Chapter 4 as well as the experimental work presented in Chapter 5. A technical overview of the components used in everyday UT is also included. The traditional techniques and methods for flaw characterization are addressed for completeness.

2.1 Principles

The origins of ultrasound may be traced back to the Curie brothers. In 1880, they demonstrated that a suitably cut plate of quartz, when mechanically stressed, develops electric charges on its surface. The generation of electrical energy, or voltage, by the application of a mechanical stress is known as the *piezoelectric effect.*

One year later, the converse of this effect was observed. That is, when a piezoelectric crystal was subjected to an alternating electric field, it rapidly changed shape, creating high-frequency vibrations in a characteristic fashion. These two phenomenon provide the absolute foundation of most uses of ultrasound known today, including ultrasonography, echocardiography and ultrasonic NDE.

2.1.1 Elastic Wave Propagation

Ultrasonic propagation is manifested as an elastic stress wave having a frequency exceeding the audible range (i.e., 20kHz). In practice, however, ultrasonic frequencies may be several orders of magnitude higher, from 100kHz to 30MHz. If the speed of sound in a material is known, then the wavelength is given by

$$\lambda = \frac{c}{f_0}, \tag{2.1}$$

where λ is the wavelength (mm), c is the wavespeed (m/sec), and f_0 (MHz) is the center frequency. This result is important in determining the sensitivity of detection in various applications since the minimum detectable flaw size is governed by the ultrasonic wavelength λ. At a frequency of 5MHz, the smallest observable defect in steel will be 1.2 mm, whereas in human tissue, it is four times smaller: 0.3 mm. In general, the smaller the damage the higher the frequency that is required.

The governing equation used to describe planar (one-dimensional) elastic wave motion is expressed as:

$$\frac{\partial^2 u}{\partial x^2} = \frac{1}{c^2}\frac{\partial^2 u}{\partial t^2} \tag{2.2}$$

where x is the particle position, t is time and $u = u(x,t)$ is the particle displacement.

The longitudinal speed of wave propagation in the medium is denoted by c_L and is dependent upon the material properties: the modulus of elasticity E, density ρ and Poisson ration ν of the material,

$$c_L = \sqrt{\frac{E(1-\nu)}{\rho(1+\nu)(1-2\nu)}} \tag{2.3}$$

Similarly, the planar transverse wave speed c_T would yield

$$c_T = \sqrt{\frac{G}{\rho}} \tag{2.4}$$

where G is the shear modulus of the medium. The ratio of c_L to c_T is often denoted by κ and may be expressed as

$$\kappa = \sqrt{\frac{2(1-\nu)}{1-2\nu}}. \tag{2.5}$$

For most solids, $\nu \approx 0.3$. Because ν is bounded between 0 and 0.5, it can be shown that $c_L > \sqrt{2}c_T$ for all solids.

The displacement u in Eq. 2.2 is satisfied by simple harmonic motion, which may be conveniently expressed mathematically as

$$u = Ae^{j(\omega t - kx)} \tag{2.6}$$

where A is the maximum particle displacement (amplitude), ω is the circular frequency, and k is the wave number (ω/c).

2.1.2 Ultrasonic Beam Characteristics

The acoustic pressure variation created by a circular resonator in the direction of the beam axis may be expressed by (Krautkrämer and Krautkrämer, 1990):

$$P(x) = \left| 2P_0 \sin\frac{\pi}{\lambda}\left[\left(\frac{D^2}{4} + x^2\right)^{1/2} - x\right]\right| \tag{2.7}$$

where x is the distance from the disc along the beam axis, λ is the wavelength, D is the diameter of the disc, and P_0 is the pressure at $x = 0$. The equation is valid only for circular piston oscillators. Pressure variation for other types of geometry, such as rectangular elements, is also provided in Krautkrämer and Krautkrämer (1990).

A plot of Eq. 2.7 is shown in Fig. 2.1, where $D = 10$ mm, and $\lambda = 0.3$ mm (wavelength in water at 5 MHz). The two distinct features of this response are the turbulent oscillations occurring before 0.04 m followed by a gradual decay after a maximum is reached at 0.08 m. The initially rapid and high amplitude fluctuations are due to the proximity of the waves to the face of the transducer. All activity that takes place up to the last maximum is said to occur in the *near field.* Afterwards, the response is in the *far field.* In most situations, UT inspectors are not interested in knowing the pressure within the near field, but are rather more concerned with the length of the near field so that inspection within this region can be avoided. The near field length is given as:

$$N_f = \frac{D^2}{4\lambda} \tag{2.8}$$

The same features of Fig. 2.1 can be shown pictorially in Fig. 2.2. Both the axial and off-axis (lateral) intensity patterns characteristic of ultrasonic transducers with circular elements are shown. The rapid fluctuations within the near field are made evident by the alternating shades of black and white. The rings showing the off-axis intensity indicate the pressure profile in the lateral direction, if one were looking along the axis of the transducer. It can be seen that the natural focus, which exists at the boundary between the near and far fields, provides the strongest amplitude along the acoustic axis. Further along the axis, this intensity will decay proportional to the distance from the transducer. The spread of the beam, or angle of divergence ψ, gives indication as to how fast the beam is losing energy:

$$\psi = \sin^{-1}\left(1.22\frac{\lambda}{D}\right) \tag{2.9}$$

where D is the aperture of the probe.

Values of ψ close to zero indicate a well directed and columnated beam which will have low lateral resolution. Larger values result in a greater beam spreading and thus have a greater chance of detecting off-axis defects. Thus, the angle of divergence is

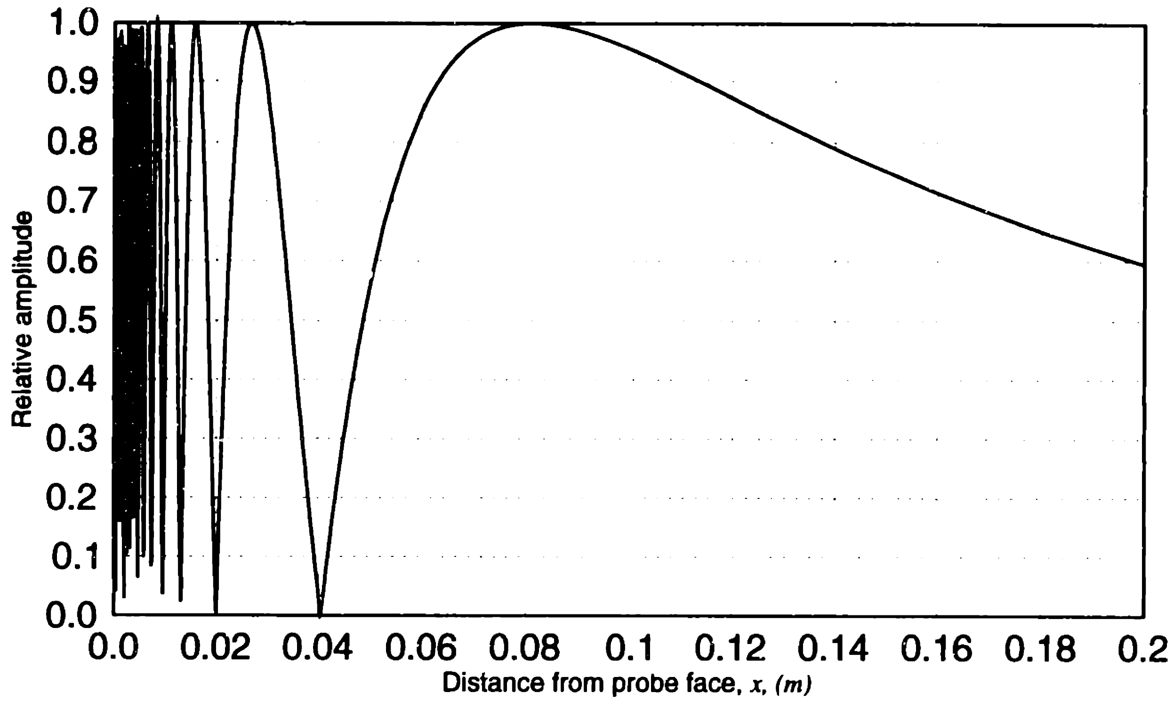

Figure 2.1: Acoustic pressure along the axis of the transducer in water.

useful for estimating what percentage of the maximum axial echo will still be received from a small reflector lying off the acoustic axis.

2.1.3 Ultrasonic Impingement at an Interface

Having discussed the general characteristics of the sound field, it is important to understand how ultrasonic waves interact and transfer energy at interfaces existing within the material or between two different materials.

Normal Incidence

In many UT inspection setups, the energy emitted from the transducer is directed downward into the material and normal to the test surface. In the presence of a transition in material properties, one is often interested in the amount transmitted or reflected, as illustrated in Fig. 2.3(a). Introducing the acoustic impedance, Z, defined as the product of material density ρ and wavespeed c, the magnitude of reflection and

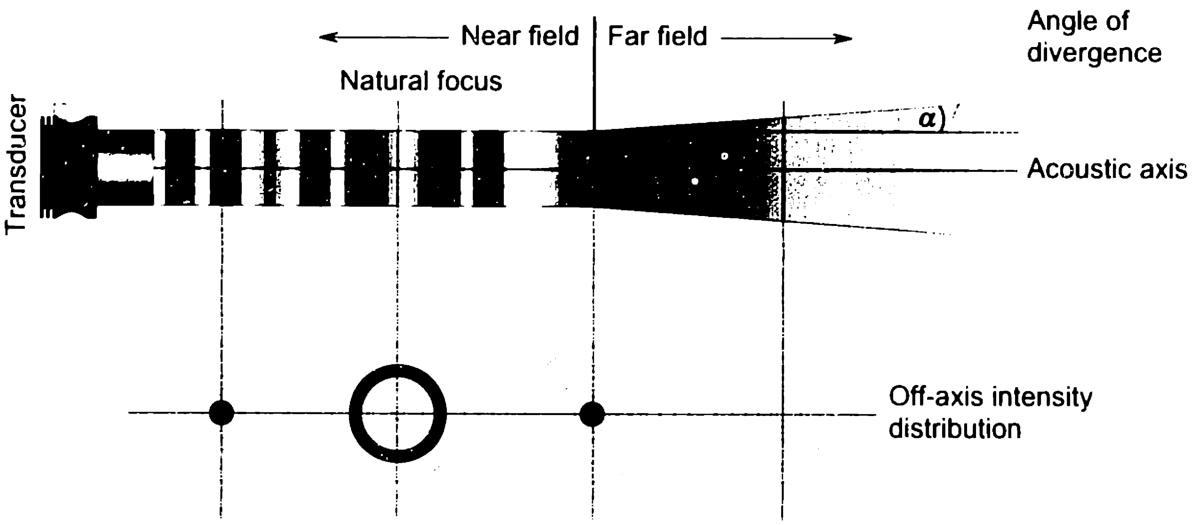

Figure 2.2: Axial beam profile and lateral intensity distribution of an ultrasonic transducer.

transmission at an interface for a normally incident beam can be computed solely in terms of the ratio of the two respective material impedances:

$$\beta = \frac{Z_1}{Z_2} = \frac{\rho_1 c_1}{\rho_2 c_2} \tag{2.10}$$

where the subscripts are used to distinguish between the two materials.

Usually the initial wave entering the system is assumed to have unit amplitude such that any interactions at the interfaces will be expressed in terms of a coefficient relative to the initial value. The reflection and transmission coefficients expressed in terms of displacement, stress and energy are given in Table 2.1.3. These coefficients are plotted in Fig. 2.4. It is important to observe that the sum of the transmissive and reflective energies is unity, which is in agreement with conservation of energy.

Oblique Incidence

Many situations arise in which oblique incidence is the preferred method of impinging ultrasound into the medium. In other cases, it is unavoidable, particularly when dealing with non-parallel surfaces. Oblique incidence is created using a refracting wedge, commonly made of perspex. Longitudinal waves emitted within the wedge are

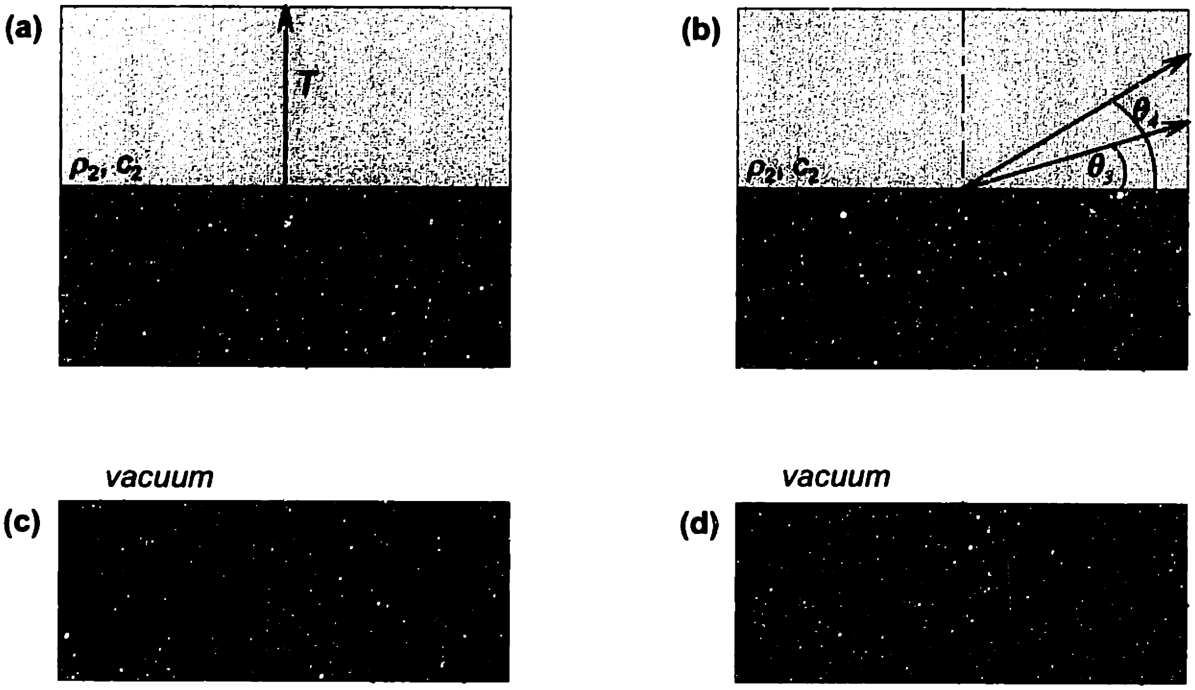

Figure 2.3: Wave reflection, transmission and refraction: (a) normal incidence, (b) oblique incidence between two media, (c) obliquely-incident longitudinal wave at a free surface, and (d) obliquely-incident transverse wave at a free surface.

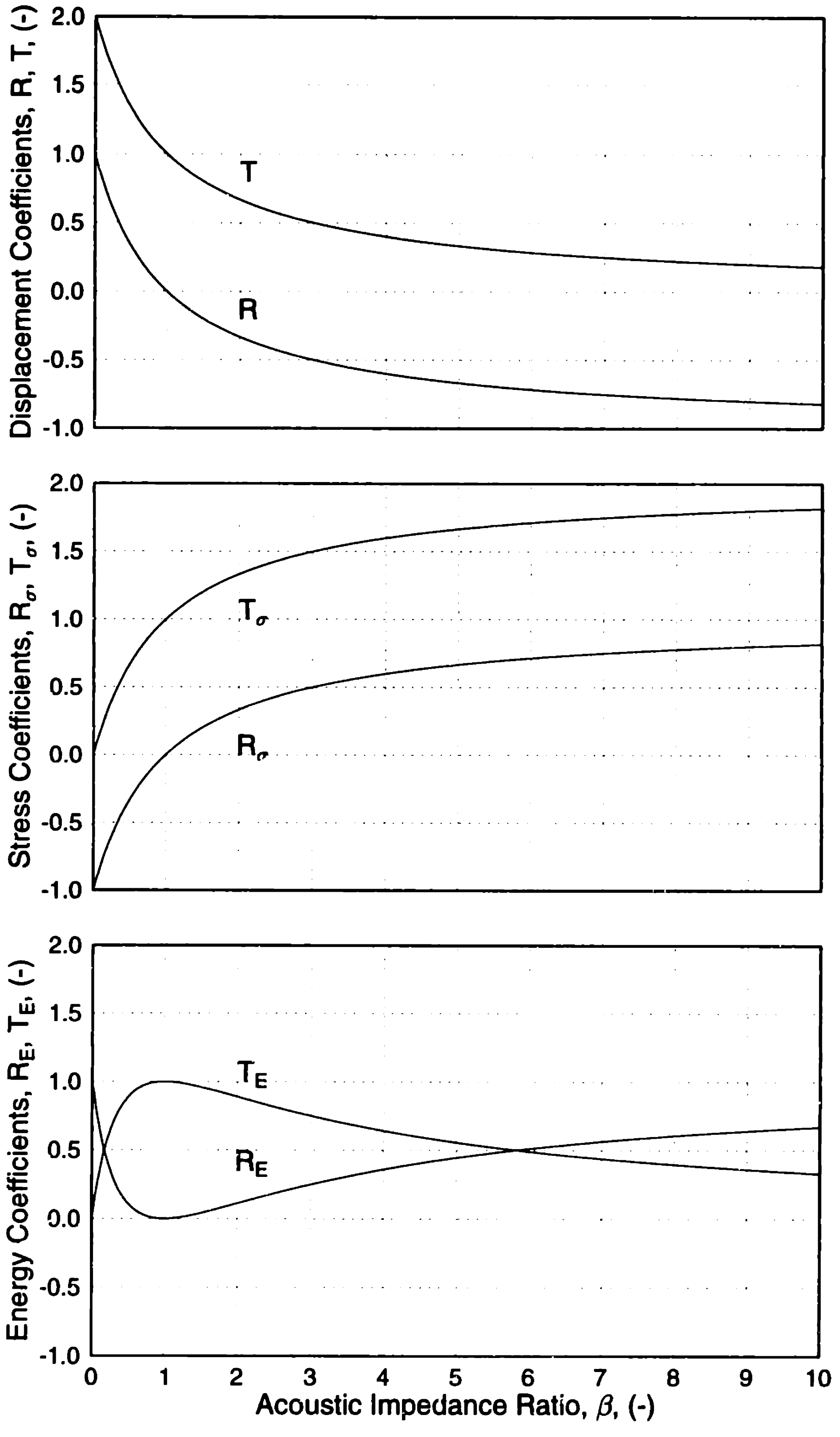

Figure 2.4: Reflection and transmission coefficients at normal incidence: (a) displacement, (b) stress (pressure) and (c) energy.

Displacement	***Stress***	***Energy***
$R = \frac{1-\beta}{1+\beta}$	$R_\sigma = -R = \frac{\beta-1}{\beta+1}$	$R_E = R^2 = \left(\frac{1-\beta}{1+\beta}\right)^2$
$T = \frac{2}{1+\beta}$	$T_\sigma = \beta T = \frac{2\beta}{1+\beta}$	$T_E = \beta T^2 = \frac{4\beta}{(1+\beta)^2}$

Table 2.1: Reflection and transmission coefficients at normal incidence.

immediately mode converted and refracted into transverse waves which will propagate at a steeper angle relative to the normal. This is often useful for weld inspections which cannot be investigated with a normally incident probe configuration.

The general situation discussed above is shown in Fig. 2.3(b). Given the refractive index c_1/c_2 between two media and the incident angle θ_i of the ray in medium 1, the refracted angle θ_r in the second medium can be obtained using Snell's Law:

$$\frac{\sin\theta_i}{c_1} = \frac{\sin\theta_r}{c_2} \tag{2.11}$$

Usually the angle of the refracted ray is required, so that

$$\theta_r = \sin^{-1}\left(\frac{c_2}{c_1}\sin\theta_i\right) \tag{2.12}$$

Since θ_r cannot exceed 90°, it follows that there is an upper limit on θ_i. That is, $\theta_i < \theta_{cr}$ where θ_{cr} is the so-called critical angle:

$$\theta_{cr} = \sin^{-1}\left(\frac{c_1}{c_2}\right) \tag{2.13}$$

For computing the reflection and transmission coefficients under oblique incidence situations, it is useful to classify interface problems according to the following boundary conditions:

- vacuum–solid

- fluid–solid
- solid–solid

Vacuum-solid interfaces are useful for approximating certain stress-free boundaries, such as air–steel. The boundary conditions require that the normal traction and shear stresses are zero at a free surface. Figure 2.3(c-d) shows the two cases in which either an incident L-wave or an incident T-wave may strike the interface. The displacement reflection coefficients for the case of an incident longitudinal and incident transverse wave in aluminum are shown graphically in Fig.2.5.

Reflection and transmission coefficients for solid–fluid and solid-solid interfaces are more complicated due to additional boundary conditions; their formulae can be found in Krautkämer and Krautkrämer (1990). The calculation of these coefficients is extremely important when performing ray tracing algorithms. Each time a ray strikes an interface, its amplitude will change such that new rays created from the incident ray have an amplitude history whose current amplitude will be the product of the coefficients of its predecessors.

2.1.4 UT Equipment and Instrumentation

Ultrasonic testing equipment is fairly light-weight and portable making it ideal for field inspections. The basic equipment required for ultrasonic NDE consists of three essential components: (1) transducer (probe), (2) pulser/receiver (P/R) unit, and (3) oscilloscope (display screen).

Most ultrasonic probes, as shown in Fig. 2.6 consist of an active piezoelectric element, usually a ceramic, which is connected to two lead wires from an external connector which supplies the necessary voltage to create a piezoelectric effect. Sometimes an internal electrical matching network may be included in the transducer to aid in matching the pulser circuitry with the mechanical response of the transducer. Normally, a backing is placed on top of the active element to help absorb reflections. A matching layer can also be placed in front of the element, functioning as an acoustic

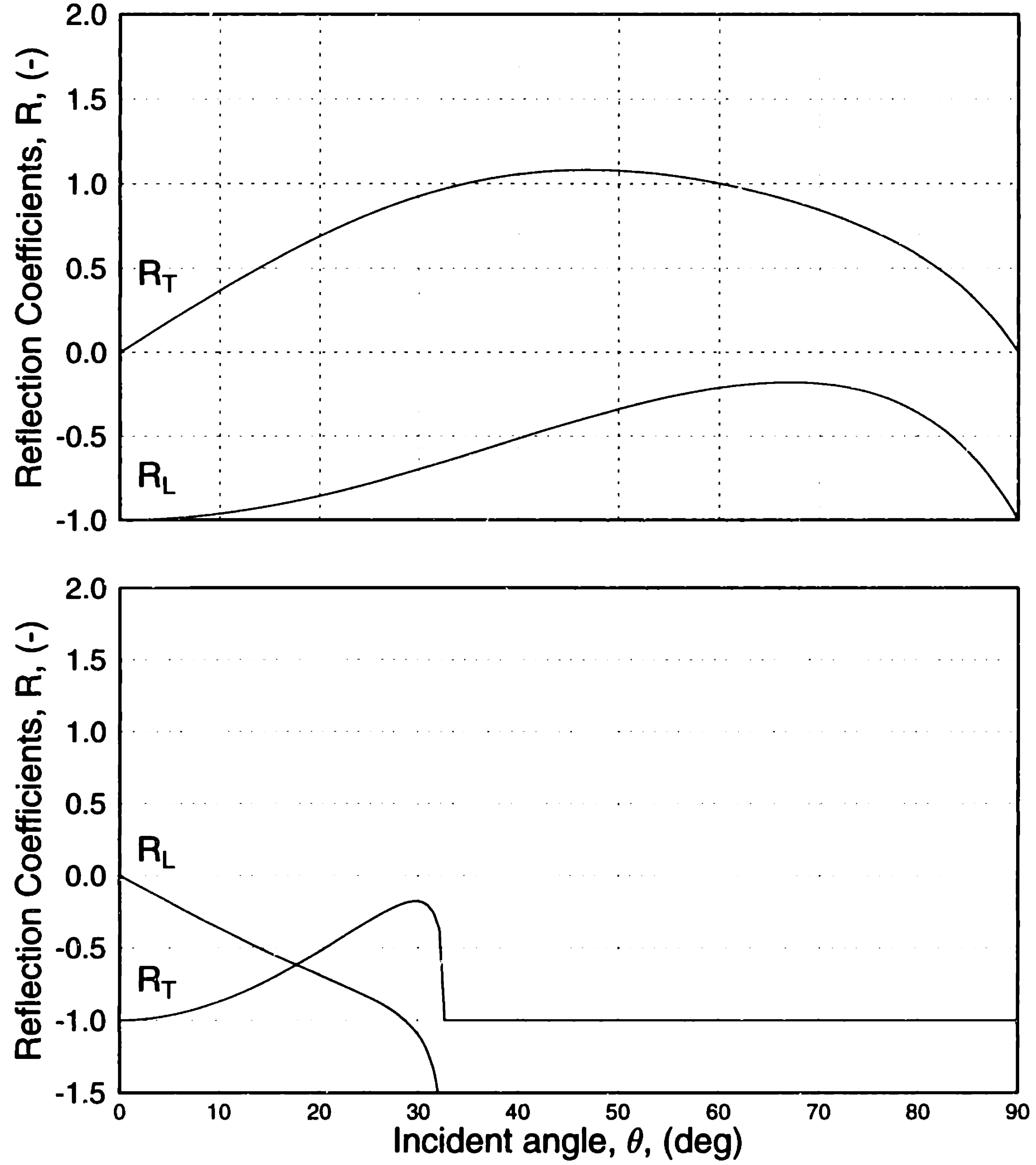

Figure 2.5: Reflection coefficient for incident longitudinal and transverse wave at an aluminum/air interface.

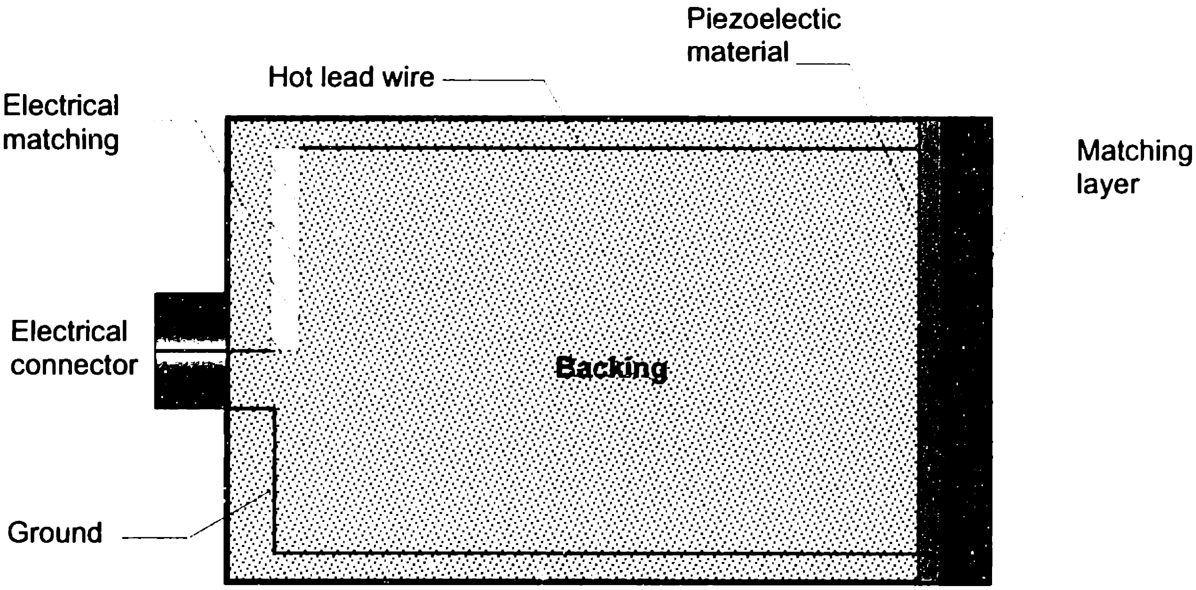

Figure 2.6: Schematic of typical probe construction.

transformer. The matching layer can boost the signal in transmission and reception. It also helps to protect the active element from damage.

The P/R unit sends an electrical pulse signal to the transducer which is converted into ultrasound via the piezoelectric effect. The ultrasonic wave will reflect off of defects inside the material and will be received by the P/R unit. The return signal amplitude of the echo will appear in the form of a peak on the oscilloscope (A-scan). The time for this pulse to travel through the material can be observed on the time axis. Nowadays, these components are integrated into compact and portable handheld units.

For the purpose of typical NDE inspections, ultrasonic probes may be divided into two groups: *straight* and *angle-beam* probes. Straigh-beam probes send longitudinal waves (L-waves) which are normally incident to the surface of the material being investigated. Internal cracks that are parallel to the material surface such as lamellar tears can be easily detected. Straight beam probes are sometimes implemented in pin-hanger connections to detect small cracks below the hanger plate. These probes are also useful in thickness gauging to determine the extent of dimensional loss in members due to corrosion. However, in order to test long members, the probe must be moved along the surface in a stepwise fashion. This process quickly wears down the face of the transducer and makes inspection procedures time consuming and cumbersome.

Figure 2.7 shows an example of L-wave testing using the straight beam probe. A flawless specimen will show a very strong return signal reflected from the backwall. If a defect is present, part of the ultrasonic energy will be reflected from the defect and the rest will be reflected from the backwall. The defect signal will appear smaller in amplitude and will occur before the backwall signal, as shown on the time axis. If the longitudinal wavespeed of the material is known, the depth h of the defect can be calculated as follows:

$$h = \frac{c_L t}{2} \tag{2.14}$$

An angle beam probe typically consists of a transducer mounted on a wedge made of perspex. The transducer sends an incident wave through the wedge to generate refracted longitudinal and transverse waves propagating in the test material. Most NDE applications use angle wedges that are set for the refracted angles of 45°, 60°, and 70° inside the material. They may also be used to create Rayleigh waves (surface waves). Variable angle-beam wedges allow the user to adjust the incident angle continuously.

The angle-beam probe is primarily used to test for cracks in welds. The angled sound path allows the sound beam to be reflected off the backwall to improve detectability of flaws in and around welded areas. Because the weldment surface is rough, direct contact with a straight-beam probe is unsuitable. Also, straight-beam probes are restricted to cracks which propagate parallel to the contact surface. Angle beams have also been used in pin-hanger connections to insonify areas prone to cracking which are undetectable using straight beam probes.

Figure 2.8 shows the common arrangement of welded inspection using the angle-beam probe. As with the straight-beam transducer, the angle beam must be repositioned until a distinguishable signal appears.

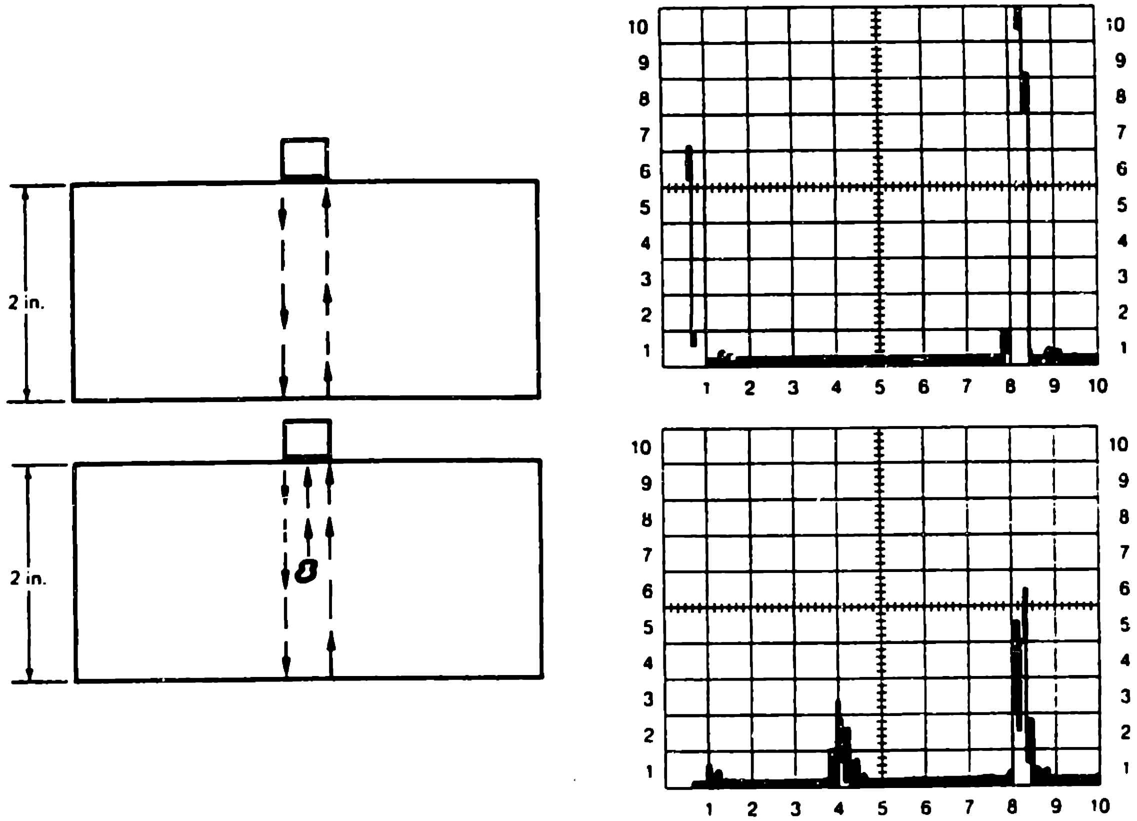

Figure 2.7: Straight-beam probe test and corresponding A-scan display. (AWS, 1985)

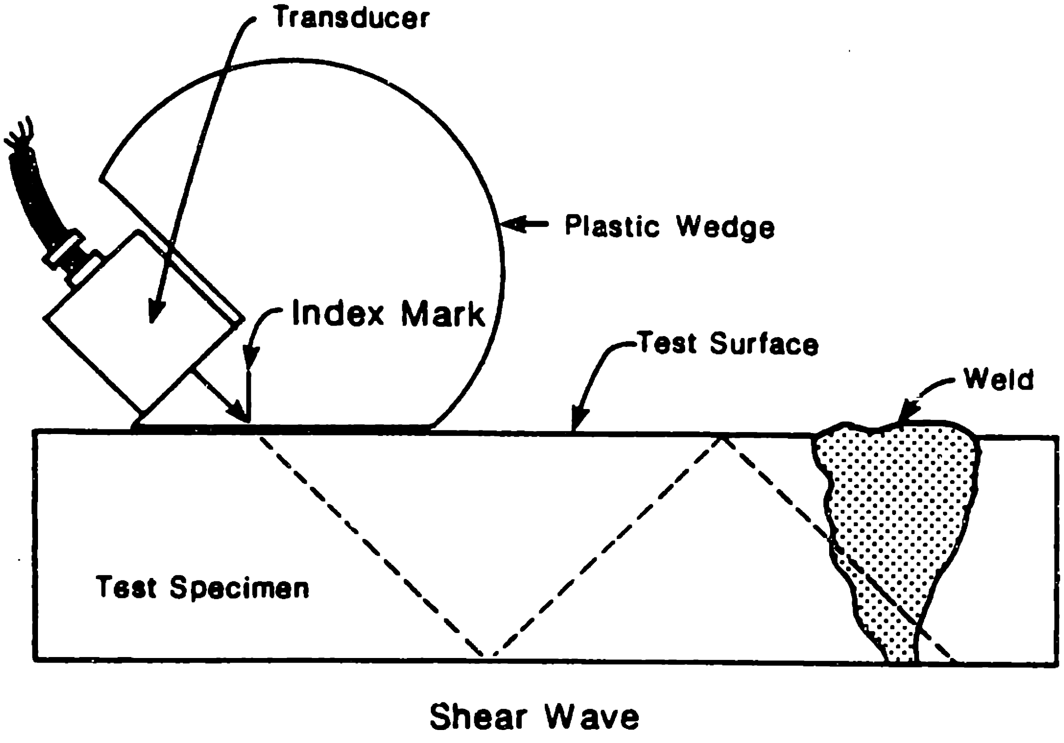

Figure 2.8: Welded inspection using an angle-beam probe. (FHWA, 1986)

2.2 Ultrasonic Methods

We will begin with an introduction to the basic transducer configurations commonly used in UT. These techniques are the backbone which lead to more sophisticated methods for obtaining information regarding the existence, location, and characteristics of defects. The principles of imaging as a qualitative aid in NDE will be addressed, followed by a summary of the methods and conclusions.

2.2.1 Transducer Configurations

Figure 2.9 illustrates the three main transducer arrangements. A single transducer operating as both transmitter and receiver as shown in Fig. 2.9(a) emits an ultrasonic signal which is reflected off the backwall of the material and received by the same transducer. This is called *pulse-echo*. This setup is often used when inspection is limited to a single side (i.e., single-sided access).

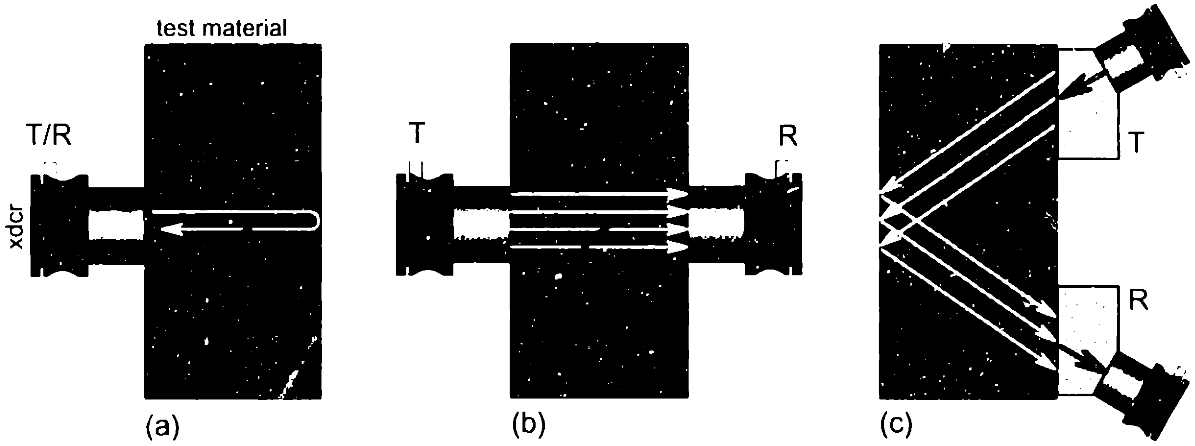

Figure 2.9: Transducer arrangements: (a) pulse-echo, (b) through-transmission, and (c) pitch-catch.

If a pair of transducers are placed on opposite sides of the medium (Fig. 2.9(b)), the pulse is said to be sent in *through-transmission*. This technique is only applicable to double-sided access. Through-transmission is very often employed for thickness gauging. In other cases, it may be used to effectively calibrate or characterize a transducer.

Two transducers situated on the same surface can be used in *pitch-catch* mode, as shown in Fig. 2.9(c). The transmitter sends an oblique beam into the specimen which will reflect off the opposite side and be collected by the receiver. Pitch-catch is ideal for time-of-flight diffraction methods. A defect may act to scatter the incoming oblique rays; some of this energy will be bent in the direction of the receiver. Although the transducers shown in Fig. 2.9 are in direct contact with the solid through the use of a couplant, all of these methods may easily be extended to non-contact applications involving a fluid surrounding medium.

2.2.2 Methods for Flaw Characterization

The *A*-scan is based on transmitting pulses on a periodic basis into a material, and synchronizing an oscilloscope to the transmitted burst. If the transmitting transducer is simultaneously used as a receiver (pulse-echo mode), then the echoes will appear

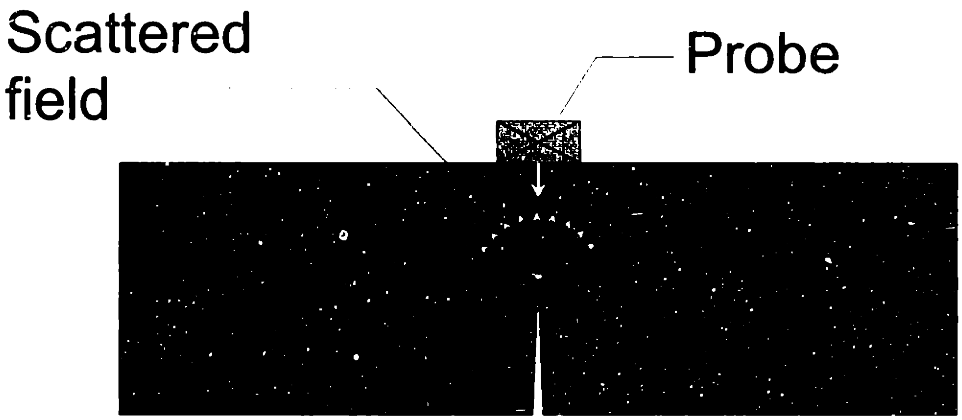

Figure 2.10: Scattered amplitude method used to measure the height of a crack.

on the screen, and the horizontal axis will give time information (this correlates to time-of-flight) while the vertical axis provides the echo amplitude. Careful analysis and interpretation of the echoes on the display screen can provide information about the extent of damage inside the material. The A-scan provides through-thickness information at a point. The A-scan (or the wavetrace) is the most fundamental form of representation that contains rich information about the material and flaws.

Interpretation of the A-scan can lead to methods which attempt to quantify certain characteristics of a crack, such as its location, size, depth, height, and orientation. This information is critical in assessing the condition of the structure and safeguarding it from potential failure. Some common methods currently employed are reviewed below.

(1) Surface-breaking Cracks: The *scattered amplitude method* is useful for evaluating the depth of a surface-breaking crack when testing from the side opposite to the crack, as shown in Fig. 2.10. A focused beam incident on the crack tip will produce edge-wave echoes resulting in wave scattering. Based on the transit time for the return signal from the crack tip, the depth of the crack may be calculated. The edge-wave echo is suitable for fatigue cracks since they have a well-defined tip edge and a smooth surface form the prolonged affect of repeated stress cycles (Krautkrämer, 1990).

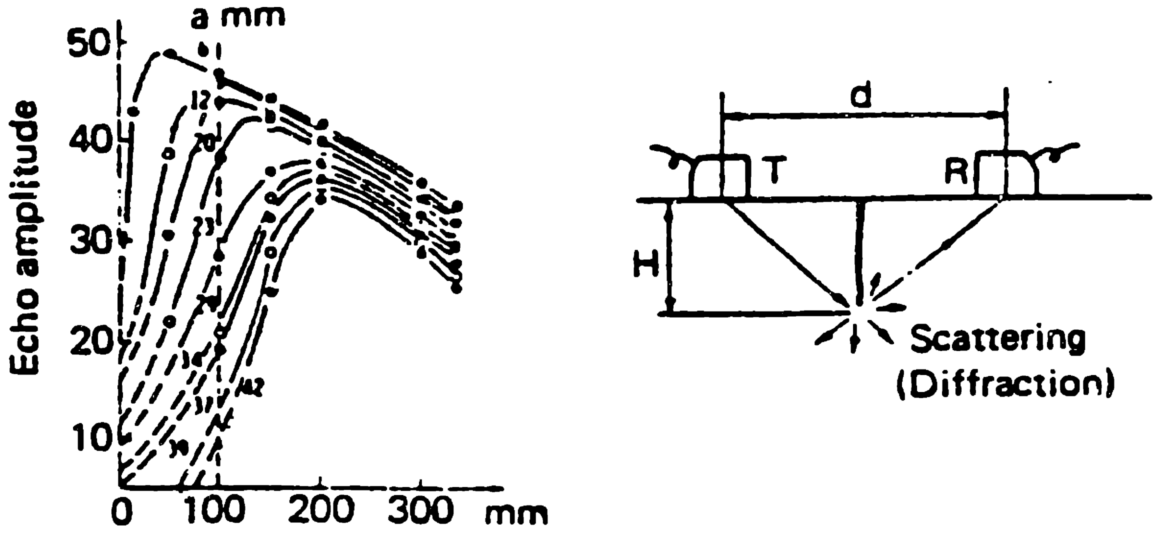

Figure 2.11: The principle of diffraction used to measure the height of a surface-breaking crack. (Ogura, 1983)

An alternate way of sizing surface-breaking cracks is by *diffraction methods* using a pair of transducers, one as a transmitter and the other as a receiver, as shown in Fig. 2.11. In this case, the transducers are placed on the cracked surface. The transmitted beam is diffracted at the tip of the crack and can be detected by the receiving probe. Knowing the distance between the probes and the echo amplitude, one can estimate the height of the crack by using a calibration curve similar to that provided in the figure. It should be noted that this method is limited by the minimum distance between the probes, making it only applicable to those defects having a height of 3 to 4 mm or more (Ogura, 1983).

Another timing method has been proposed by Mak (1985), whereby the location, height, and orientation of a surface-breaking crack can be determined using an obliquely incident shear wave transducer from two scan positions on either side of the crack. By assuming that the sound beam radiates from the wedge exit point of the transducer, Mak developed simple trigonometric expressions to characterize the crack. An advantage of this method is that it is independent of the incident probe angle. The methods described in his paper measure the time traversal between the probe exit point and the crack tip and root respectively. The probe can be positioned at various locations to detect signal responses from the tip and the root. Measurements at different positions can help to reduce the random error of the crack height and angle.

(2) Internal Cracks: In sizing internal cracks, the method employed depends on the crack size relative to the beam width of the probe used. For small cracks which are completely covered by the ultrasonic beam, standard *amplitude pulse-echo methods* may be used. Since the size of a crack is related to the return signal amplitude, it is possible to calculate the size of a crack based on known reference reflectors.

Larger cracks exceeding the beam width are usually sized using the *echo dynamic method*, as illustrated in Figure 2.12. This method assesses large defects from the variations of its echo when scanning the surface with the probe in a back-and-forth fashion. In this case the probe must be moved to trace the edges of the crack. The echo envelope between the edges accounts for the way the sound level rises and falls as a beam of ultrasound is traversed across a crack and can be used to estimate the cross-sectional height of the crack. For precise evaluation, mechanical scanning is often preferred over manual movement since better contact and guidance of the probe can be maintained. The accuracy of this method degrades as the sound beam deviates from normal incidence to the crack (Ogura, 1983).

There are a variety of measurement configurations which will facilitate the characterization of defects using the classical methods mentioned above. The *time-of-flight diffraction* (TOFD) method is useful for evaluating the height of internal cracks that are normally incident to the material surface. In this case, the transmitting and receiving probes are positioned so that the time of travel of the diffracted waves at the crack tip and root may be obtained. Knowing the time of travel and speed of sound in the material, the crack height can be estimated, as shown in Fig. 2.13.

2.2.3 Imaging Principles

By processing the A-scan, we can extract various information. However, A-scans only provide point-wise representation and require a high level of knowledge and experience

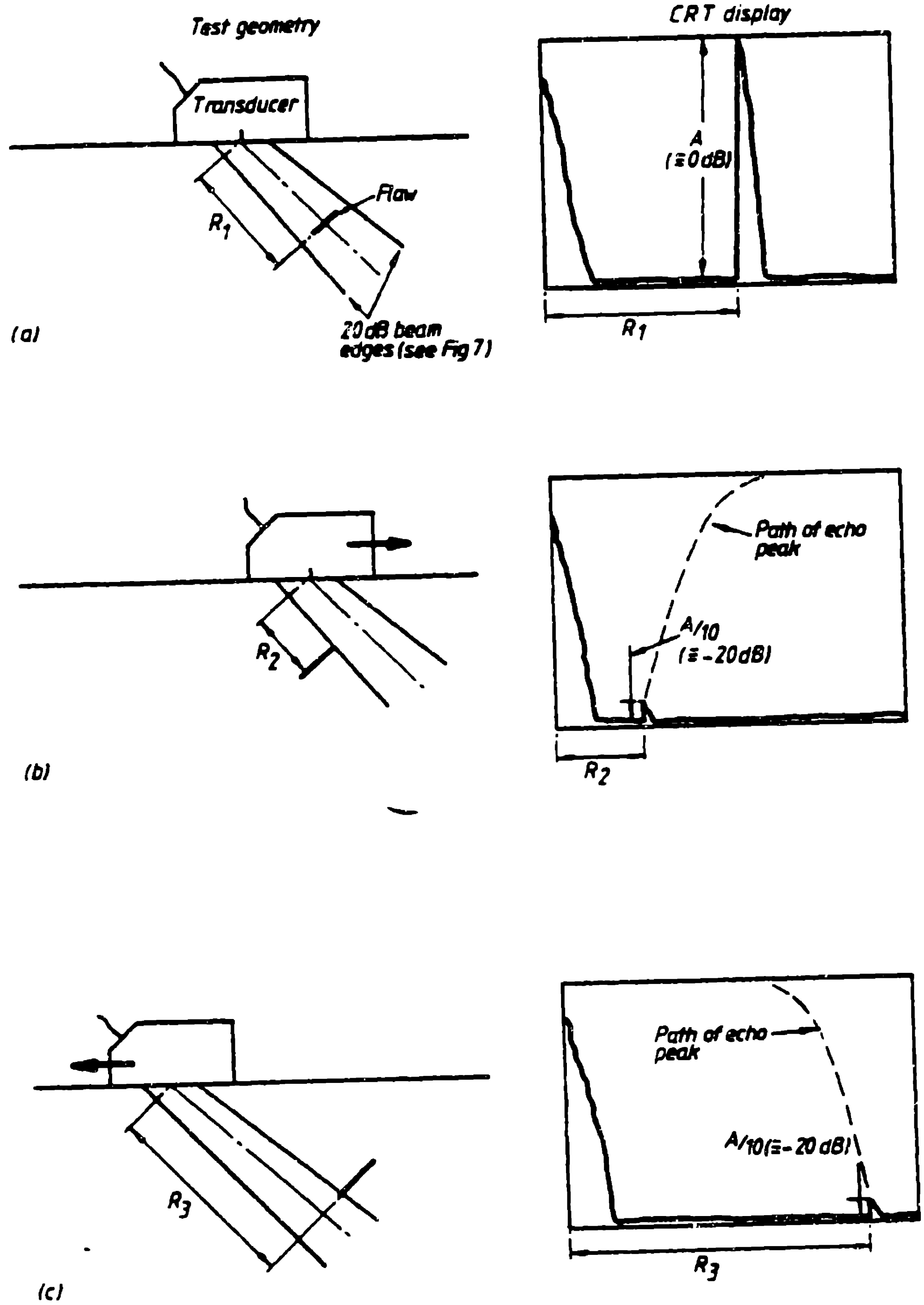

Figure 2.12: Sizing cracks using the echo dynamic principle. (Ogura, 1983)

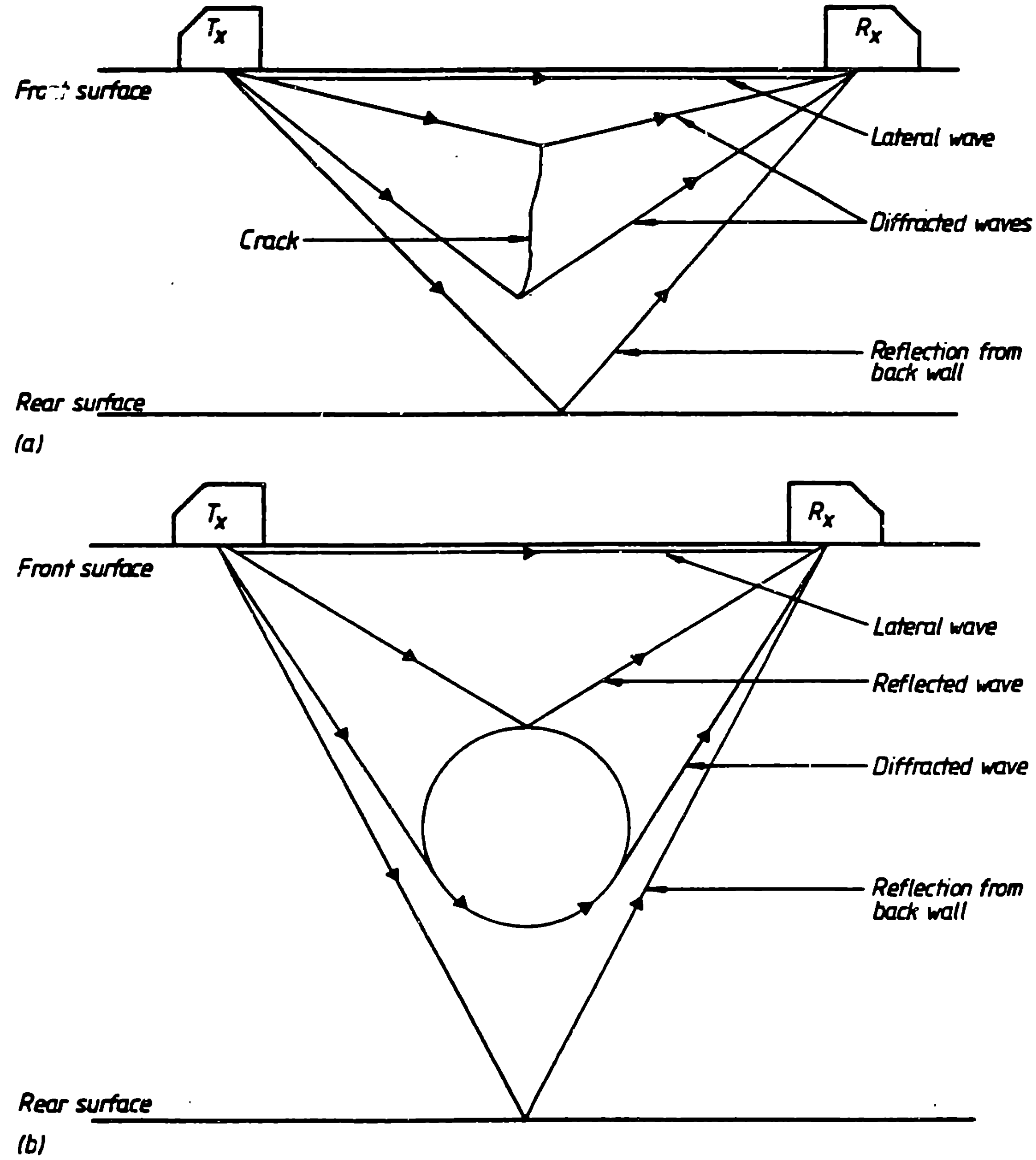

Figure 2.13: The principle of time-of-flight diffraction used to measure the height of a crack. (Jessop *et al.*, 1981)

of an operator. A-scans can be further extended to B-scans and C-scans by scanning and processing the A-scans at each point for ultrasonic imaging of flaws.

The B-scan represents a cross-sectional view. Since the time required for the wave to travel from one place to another (i.e., time difference between the points) is proportional to the distance between the points, we can extract information in the thickness direction at a point. Scanning by storing repeating A-scans along a line, an image of a cross-section can be obtained as shown in Fig. 2.14.

An image obtained by scanning over an area is called C-scan. C-scan represents a planar view of the material and flaws. In order to provide excellent resolution, a focused transducer is usually used for scanning. In general, intensity or echo amplitudes are mapped into brightness of the image while the transducer scans the area of interest on the specimen in raster fashion, as shown in Fig. 2.14. Since the backface reflection represents the signal loss due to material attenuation and reflection from flaws (if they exist) along the path of ultrasonic wave propagation at each point. Mapping the amplitude of backface reflection is often used to construct an image.

The A-, B- and C- scans are often done in an immersion tank. Immersion, rather than direct contact testing, offers several advantages. An aqueous environment will result in the minimum wear of the transducer, assuming it is watertight. Also, since fluids can only sustain longitudinal waves, the creation of transverse waves due to refraction at the transducer/fluid interface can be avoided. Finally, water forms a uniform and even coupling medium between test material and transducer.

2.2.4 Summary of Ultrasonic Methods

UT has many applications for inspecting welds, detecting porosity, voids, inclusions, corrosion, cracks, and other discontinuities. Virtually all industrial ultrasonic inspection schemes employ a single transducer operating in pulse-echo mode or two transducers operating in pitch-catch or through-transmission modes. The transducers are usually mounted on the surface with wedges to impinge sound waves into the material at a controlled incident angle and the signals are usually analyzed based on the amplitude and time-of-flight (TOF) measurements.

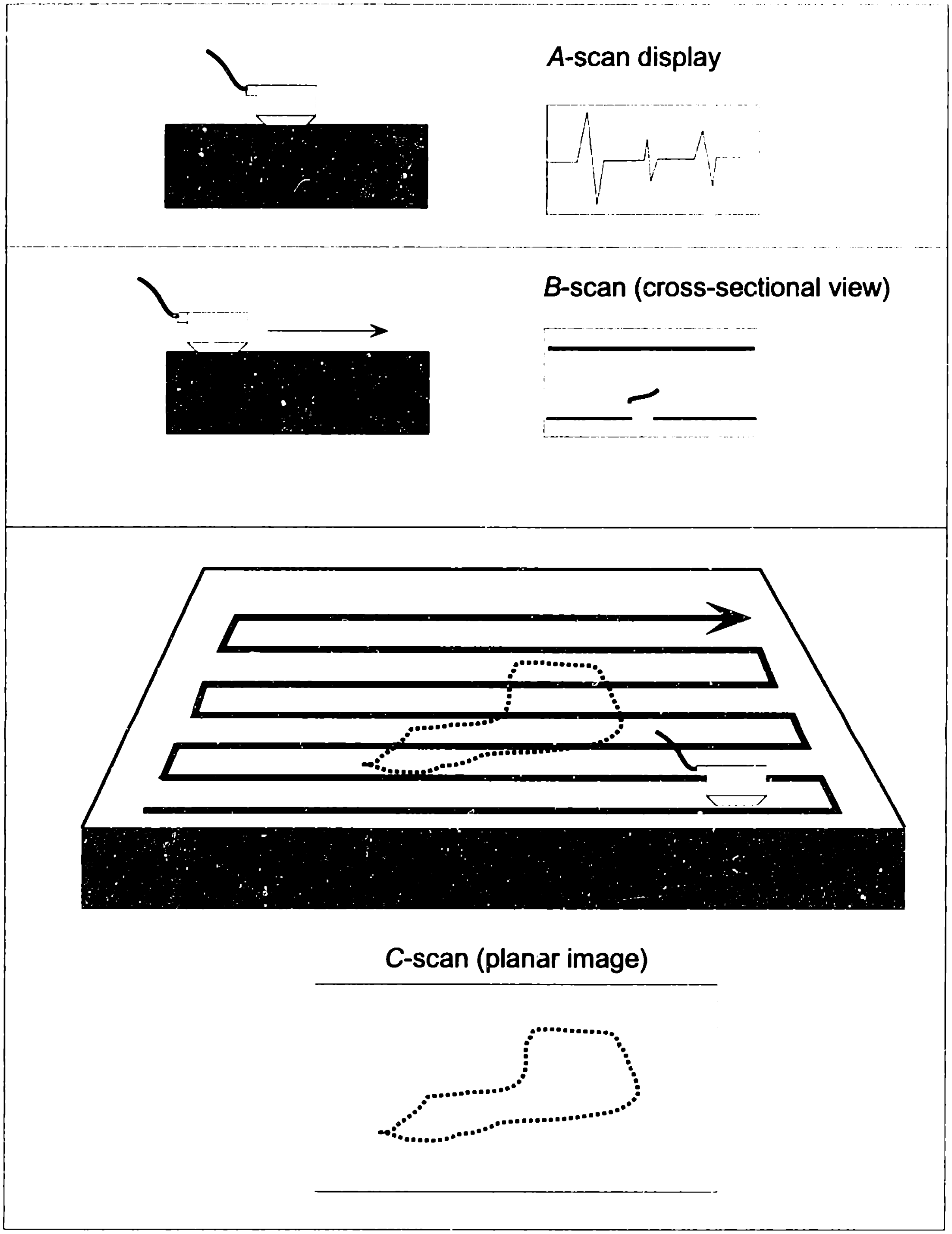

Figure 2.14: Imaging scan modes.

All the methods reviewed using the straight-beam and angle-beam suffer from some common drawbacks. The most important is the transducer movement required to locate the crack along the member. This requires a highly skilled inspector who must be able to accurately interpret the signal. Manual scanning using a transducer tends to reduce the probability of detection. In addition, the inspection can become time-consuming and cumbersome. Since there are a variety of angle paths required to investigate a flaw in a particular configuration, it is often necessary to employ several different probes for the same test. Many of these methods require calibration based on known defect sizes, and it must be kept in mind that the testing is restricted to specific crack shapes and rather limited configurations of the member or test material being inspected.

In summary, the classical ultrasonic methods sometimes are not adequate for large structures because of the following reasons: (1) Resolution is limited due to their inherently low aperture, (2) Interpretations of inspection data are very much subjective and rely on the operator's level of experience and skill, (3) These methods are sensitive to the orientation of flaws resulting in low probability of detection, and (4) Inspection time is often too long.

Nonetheless, ultrasonic NDE is a powerful tool for quantitative flaw characterization which can be used to determine location, size, and orientation of existing cracks. These methods, however, require a highly skilled operator for data interpretation and the test surface should be prepared prior to testing. At this stage, UT is only used for in-depth inspection and thus requires improvements to be used effectively in practice. In the next chapter, we will discuss the background and principles of phased array transducers as a means of enhancing the current UT technology.

Chapter 3

Background and Principles of Phased Array Transducers

This chapter will examine the underlying principles of phased array technology. The beam forming concepts will be introduced followed by a discussion of various array geometries and their capabilities and limitations. Current applications of phased arrays in NDE will be explored, as will the potential applications to civil infrastructure. A theoretical model, developed by Wooh and Shi (1995) will be presented as a means to understand the behavior of the sound field in terms of its pressure distribution. This work will provide the basis for the experimental study in Chapter 5.

3.1 Overview

Although actively used in medical applications such as echocardiography, hypothermia, diagnostic imaging, and OB ultrasound (Weyman, 1994), phased arrays have had limited applications in nondestructive testing. Several studies do, however, indicate considerable promise (Macovski, 1979; Sutton, 1979; Kino, 1979; McNab and Campbell, 1987; Schwartz, 1987; Hatfield *et al.*, 1994) for various NDE applications. Using a number of small elements, the phased arrays employ time delayed pulses which subsequently activate selected array elements. This sequence of delayed excitation of transducer elements gives the freedom of beam forming through steering and focusing of the ultrasonic waves. The phased array transducers can help to simplify the inspection problems especially for large structures having complicated geometries. Due to the flexibility of synthetic beam steering and focusing, the array sensor covers a broad area of the structure with small, light-weight sensors while preserving the sensitivity and resolution.

The configuration of a UT phased array system closely resembles that of a conventional system except for the noticeable increased complexity of hardware due to the required multiplexing of separate channels. Although the mechanism for generating delays varies from system to system depending on the application, the basic features of a phased array include a multiplexing system capable of generating and selecting delayed TTL pulses, and a number of pulser/receiver channels dedicated to a specific array element. The signal triggers a specific channel by the prescribed delay and then excites the corresponding element on the array. Received signals are delayed by the same amount to account for the varying propagation times and then summed. The signal can then be viewed on an A-scan display device. By rapidly changing these delays and using an A/D converter, one may obtain an image of the area investigated beneath the array.

3.2 Beam Forming Concepts

The fundamental operation of beam forming is shown in Fig. 3.1. Delayed pulses are sent to individual array elements so as to control the location of the beam in transmission. [1] The location can be described in terms of the steering angle that the beam makes with the normal, as well as the point at which the beam is focusing. Focusing is normally valid within the near field so that far field beam forming can only be achieved through steering. Upon reflection, individually received signals must be time-shifted according to the delay law and summed to acquire the response at the target.

---

[1] We will use the linear phased array as the basis of discussion in this section as it is the most common and easily understood geometry. Other geometries which have highly specialized beam forming capabilities will be presented in the following section.

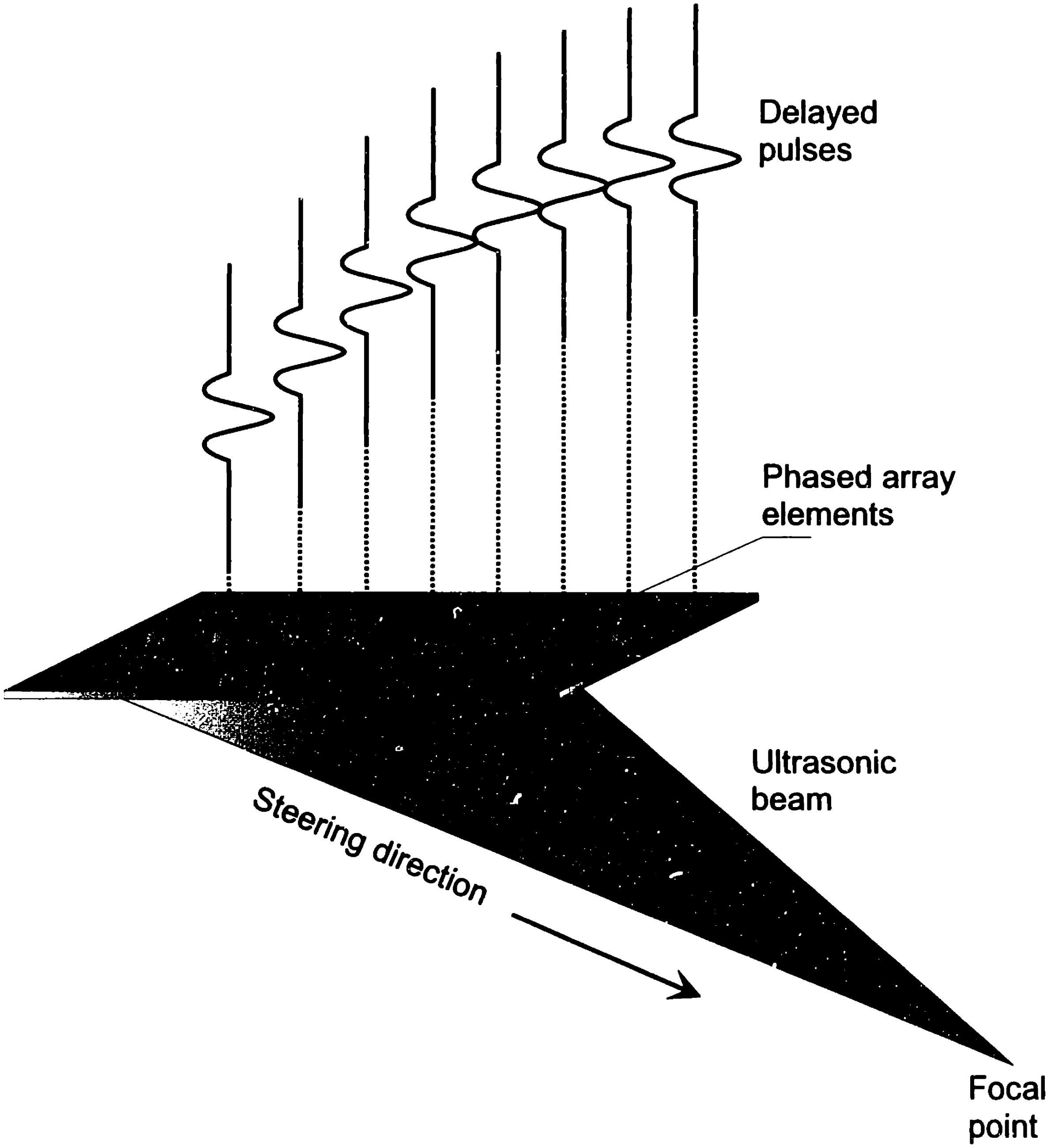

Figure 3.1: Principle of electronic beam control.

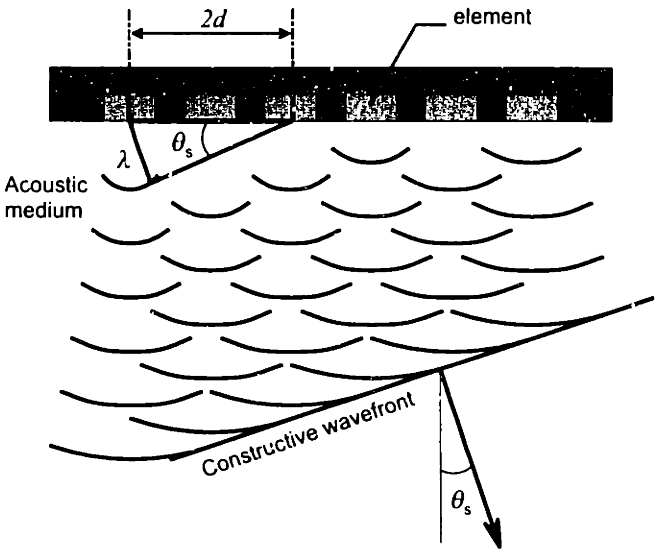

Figure 3.2: Huyghen's principle used to derive the steering formula.

Steering

Consider delaying each element by a fixed increment $\Delta\tau$. Individual array elements are fired at a time delayed by a multiple of $\Delta\tau$ so that the Huyghen construction may be used for the waves (Silk, 1983), as shown in Fig. 3.2. The net result is that the ultrasonic wavefront is propagating at an angle θ which may be expressed as:

$$\theta_s = \sin^{-1}\left(\frac{c\Delta\tau}{d}\right) \tag{3.1}$$

where c is the ultrasonic wavespeed in the medium and d is the center-to-center distance between the transducer elements in the array system. Electronic beam control in this fashion is called beam *steering* and is illustrated in Figure 3.3(a).

In theory, this formula implies no limit to the value of the steering angle and in principle becomes 90°, that is a tangential beam at a given value of $\tau = \pi d/2c$. By contrast, conventional ultrasonic insonification through an angle beam wedge is limited by the critical angle.

It should be noted that the steering formula (Eq. 3.1) does not predict the distribution of beam intensity as a function of angle. This presents two potential complications: (1) an insufficient amount of energy may be emitted at a particular steering angle due to beam spreading, and (2) anomalous signals of equivalent amplitude may appear at other angles (grating and side lobes). These issues will be resolved through modeling of the phased array sound field in the next chapter.

Another important limitation of Eq. 3.1 is that it accounts only for short pulse emission. In reality, most transducers emit cyclic pulses so that there is a separation of λ between successive positive cycles. As a result, other forms of constructive interference may occur, such as the first cycle of element 1 interfering with the second cycle of element 2, etc. One can then account for the additional beam deflections at higher modes such that

$$\theta_m = \pm \sin^{-1}\left(\frac{m\lambda}{d}\right) = \pm \sin^{-1}\left(\frac{mc}{fd}\right) \tag{3.2}$$

where m is an integral mode number, and θ_m is the angle (positive and negative by symmetry) at mode m.

The steering angle is limited by ±30° when going from the low velocity to high velocity medium, as is the case for most medical applications. However, when placed on steel, this would be increased to ±90° (DeSilets, 1978), making phased arrays attractive for NDE applications. This phenomenon is particularly useful for inspecting large structures because the ultrasonic beam can travel longer distances for increased steering angle.

Focusing

Focusing is obtained by variably delaying a group of elements with respect to the center element. For example, when a delay line takes a quadratic form, as shown in Fig. 3.3(b), the beam is converging at a focal point where the focal distance is a function of delay line, wavespeed, and element distance. This relationship may be written as (Von Ramm and Smith, 1983):

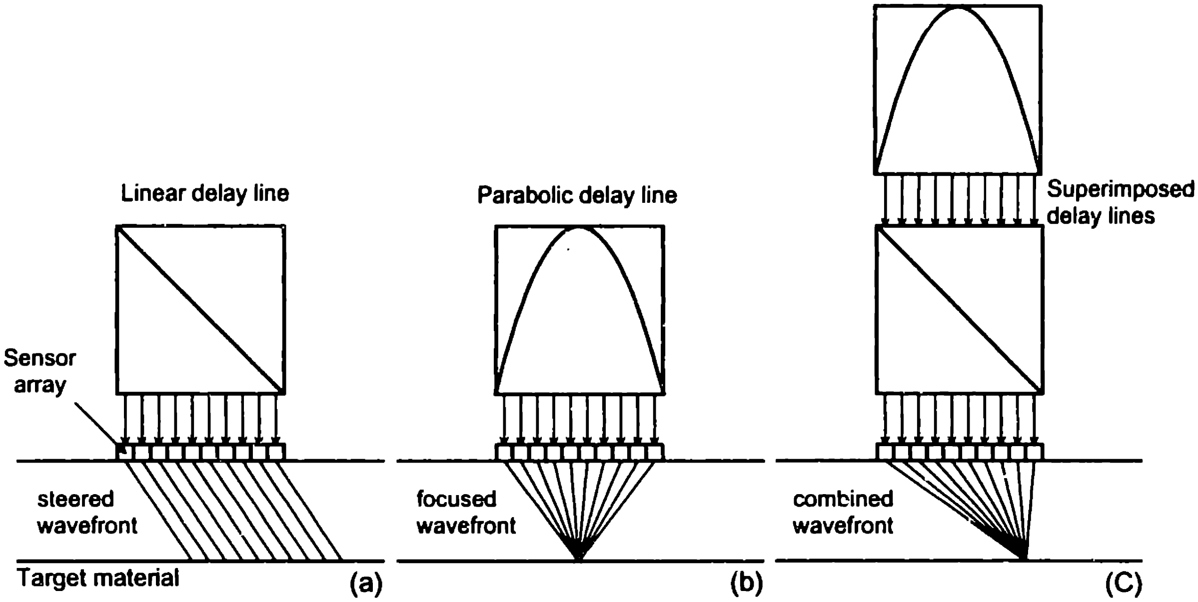

Figure 3.3: Principle of electronic beam forming: (a) A linear delay line creates a deflected beam, (b) a quadratic profile results in a focused beam and (c) superposition of the two profiles combines both steering and focusing.

$$\Delta t_n = \frac{F}{c}\left(1 - \left[1 + \left(\frac{nd}{F}\right)^2 - 2\frac{nd}{F}\sin\theta\right]^{1/2}\right) + t_o \tag{3.3}$$

where Δt_n is the required delay for the nth element, t_o is a constant of large enough magnitude to avoid negative delays, F is the focal distance, θ is the steering angle, c is the material wavespeed, and n is the element number, with respect to the center element.

It is possible to manipulate the delays and receiver patterns in such a way that multiple foci are created. This results in a *dynamic focusing* effect, extending the depth of field and maximizing the energy at a reflector and obtaining a controllable focal spot, both sharp and long. Conventional single element focused transducers do not have this feature since the acoustic lens is of a specific concavity and fitted in the probe to provide a fixed focal depth.

There are other indirect beam-forming operations such as auto-focusing, or self-focusing adaptive array (Beardsley *et al.*, 1995). This particular method exploits the offline processing capabilities of phased array hardware to achieve greater beam control and performance. The method does not require the use of the beam steering and focusing formulas given in Eq. 3.1 and Eq. 3.3. Rather, it uses a phased array to send a beam with no delay to a group of scatterers and is able to locate the maximum reflector from the group by iterating through a cross-correlation algorithm. The end result is a focused beam produced without knowing the position of the defect or material wavespeed beforehand.

3.3 Phased Array Geometries

In this section, we will discuss the principal features of the three basic array geometries: linear, planar and annular. The delay formula required for beam steering and focusing will be given as well as the chief benefits and drawbacks of each configuration.

Linear arrays have aperture divided into bars between one and one-half times the ultrasonic wavelength in width. The ultrasonic field pattern can be influenced in only one plane, the *azimuthal* plane. By appropriate phasing and amplitude shading, the sound beam can be steered and focused (cylindrical focus) and the side-lobe level can be reduced. Excitation of longitudinal, transverse, and surface (Rayleigh) waves is possible. Figure 3.4 shows the geometry and notation convention adopted for the linear arrays.

Planar arrays (also called matrix or two-dimensional arrays) have transducer elements distributed in a two-dimensional fashion, as shown in Fig. 3.5. With this array type it is possible to perform three-dimensional beam forming.

The governing equation used to determine the required delay t for a given element n_x, n_y is expressed as (ASNT, 1991):

$$t_{n_x,n_y} = \frac{d}{c}\left(n_x \cos\alpha + n_y \cos\beta\right) + \frac{d^2}{2cF}\left(n_x^2 \sin^2\alpha + n_y^2 \sin^2\beta\right) - \frac{d^2}{cF}\left(n_x n_y \cos\alpha \cos\beta\right) \tag{3.4}$$

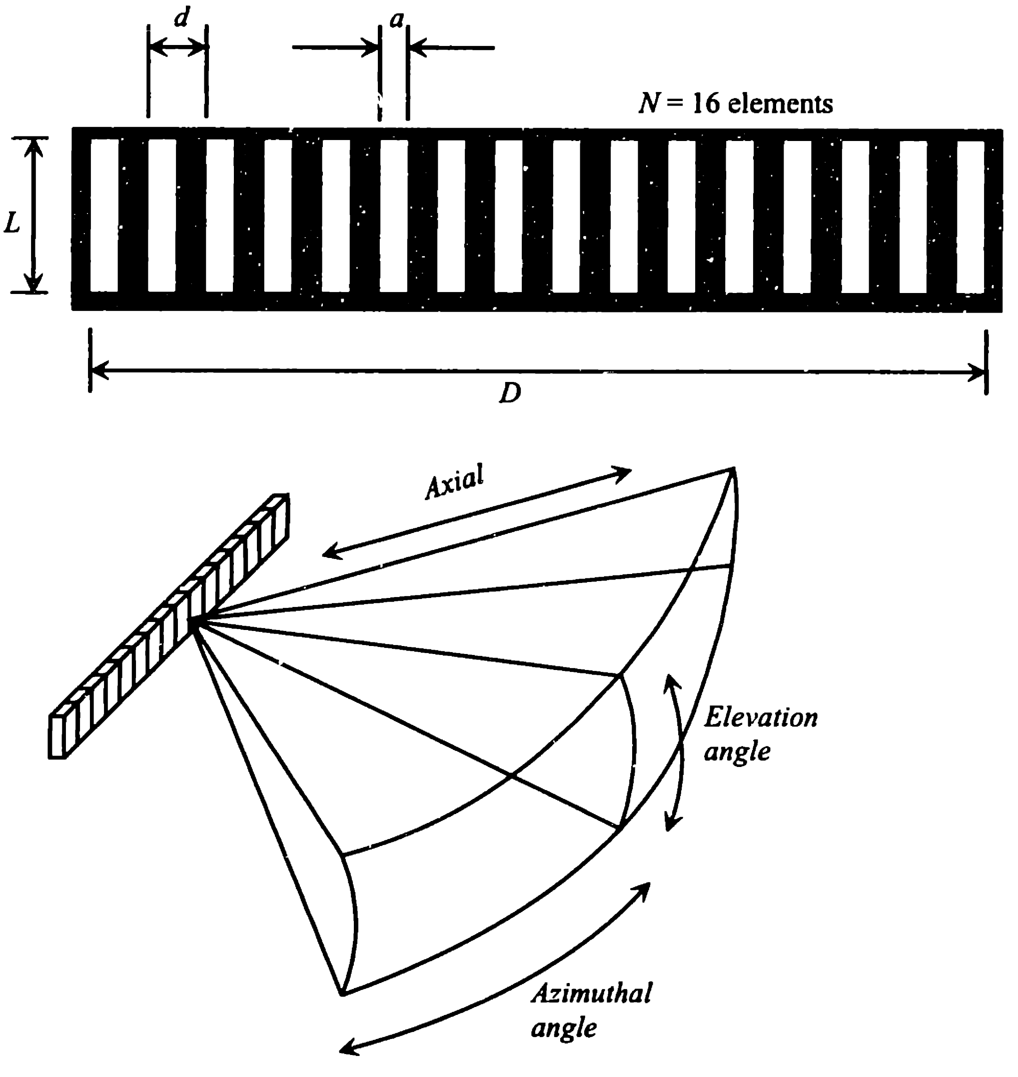

Figure 3.4: Linear array geometry and typical field of view.

where α and β are the X and Y direction angles to the point of interest, respectively, and the remaining variables are defined according to Eq. 3.3.

The sound field behavior of these arrays has been studied extensively (Turnball and Foster, 1991, Turnball and Foster, 1992, Smith *et al.*, 1991). Their use up to this point has been restricted primarily to medical applications. Although the benefits perceived from volumetric imaging of a structure are awesome, the huge increase in required channels to drive the array is a major factor deterring the use of 2-D probes in NDE.

Annular arrays consist of concentric rings, as shown in Fig. 3.6. The focus can be optimized to form a tube of minimized width over a relatively long range. This type has the advantage that the pressure distribution is symmetrical with respect to the beam axis; however, variation of the angle of incidence is not possible. It has been shown that superior focusing, lower side lobe levels and simplified electronics can be achieved by using concave annuli (ASNT, 1991).

A concave annular array with a radius of curvature R_c can be focused at a depth of d_f according to the following formula (ASNT, 1991):

$$t_j \approx a_j^2 \frac{\left(\frac{1}{R} - \frac{1}{d_f}\right)}{2c} \tag{3.5}$$

where t_j is the time delay between element j of radius a_j and the center element.

3.4 Applications

Phased arrays have been much less widely implemented in the NDE field, although there are some reports of successful applications in certain areas of material evaluation. The review of the literature shows that there is indeed extensive research well underway to advance phased array technology in NDE.

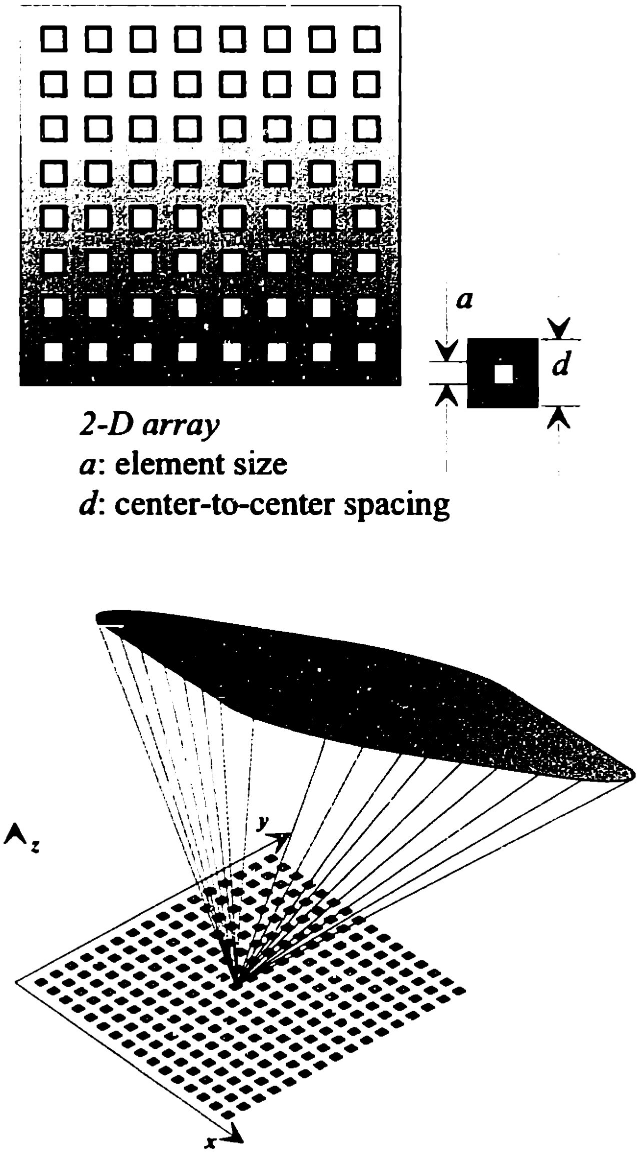

Figure 3.5: Linear array geometry and typical field of view.

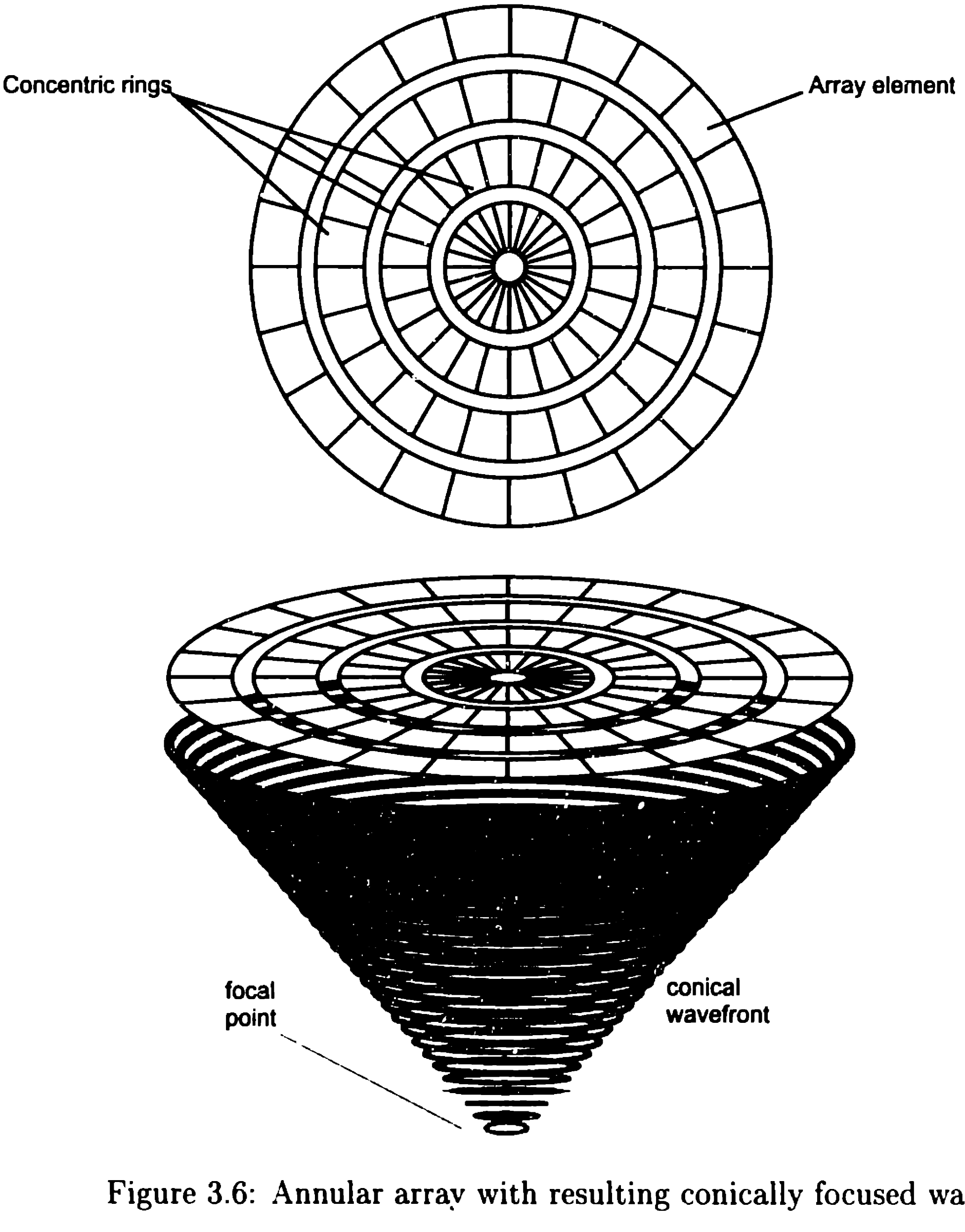

Figure 3.6: Annular array with resulting conically focused wavefront.

3.4.1 Current Applications

Literature findings indicate that phased arrays show promise in the following applications: (1) titanium and other billet inspections (Solomon *et al.*, 1994), (2) piping damaged by microbiologically influenced corrosion, (3) detecting and sizing pit corrosion in reactor fuel and target tubes, (4) detecting and sizing micro-shrinkage cracks in thin-wall iridium welds (Howard, 1994), (5) volumetric imaging of thermal fatigue cracking in feedwater pipe-to-nozzle welds (Bisbee and Burns, 1994), and (6) detection of composite defects.

Welds

Bisbee and Burns (1994) implemented a phased array system known as TestPro/FATS (Focused Array Transducer System) in the ultrasonic examination of thermal fatigue cracking in feedwater pipe-to-nozzle welds. Bisbee states that the TestPro/FATS integrated system offers several advantages over conventional ultrasonic examination techniques:

- Highly focused ultrasonic beam reduces effects of beam spreading.
- Ultrasonic beam remains focused through entire weld thickness.
- Smaller beam offers superior resolution and characterization.
- Advanced data acquisition and storage provide documentation of results, archival of data, and review of actual examination results.

A demonstration of TestPro/FATS system capabilities was recently completed. The area of interest was an actual fatigue crack contained in a 16-inch (406.4 mm) diameter, 0.75 inch (19 mm) wall thickness feedwater pipe-to-nozzle weld mockup. Based on *B*- and *C*-scan images of this defect, the length was determined to be 1.175 inches (29.85 mm), located at a depth of 0.287 inches (7.3 mm). The array used in this investigation was 5 MHz and 1.125" (28.6 mm) in diameter. It was composed of five circular elements producing a circular beam spot with each element in the array pulsed

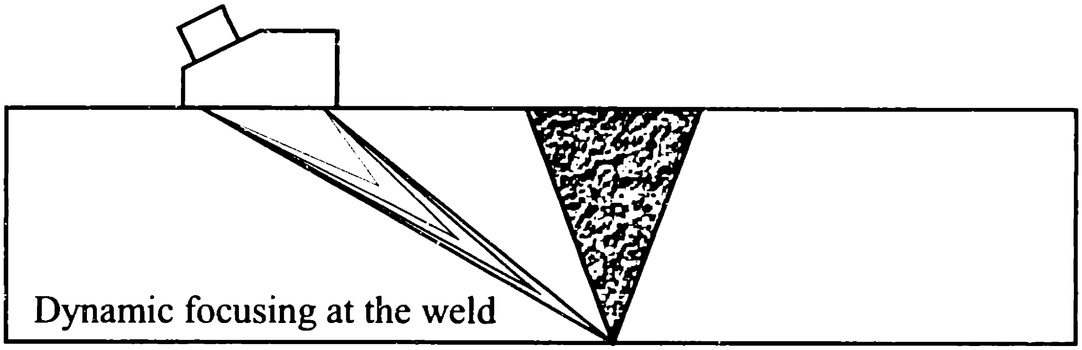

Figure 3.7: Detection of weld cracking using FATS dynamic focusing methods.

separately to generate a very high sound intensity within the area of interest. Variable phasing of all the elements allows focal point location control within the component over a wide range of depths. An illustration of the FATS method employed is shown in Fig. 3.7.

Titanium billets

FATS has also been used to improve the inspection of titanium aircraft components. Titanium billets, which are forged into jet engine disks, pose a unique challenge for ultrasonic inspections because of the varying diameters. Also, materials such as titanium, which characteristically have a high strength-to-weight ratio, often have large material grain structures. Conventional techniques use a fixed focused transducer which focuses at 1" (25.4mm) into the billet. However, for larger diameter billets, the resulting beam spread is very large and astigmatic. The beam spreading prevents a sharp focus at the center of the billet and is often barely detectable above the noise produced by the large grain structures.

To remedy this problem, Solomon *et al.* (1994) have employed a FATS technique, demonstrating electronic focusing through the billet diameter. This particular system provides five electronically controlled focal points which can be scanned throughout the billet depth. An interchangeable lens is chosen for the large aperture (1.75", 44.45 mm), seven element array transducer. Results show that the detectability is significantly improved.

Piping, Tubing, and Iridium Welds

Howard (1994) reports some other interesting applications of the FATS which were conducted at the Department of Energy's Savannah River Site, located in Aiken, South Carolina. There were three areas for which some successful results using focused array technology were obtained:

- Piping damaged by microbiologically influenced corrosion
- Detection and sizing pit corrosion in reactor fuel and target tubes
- Detecting and sizing microshrinkage cracks in thin-wall iridium welds

Howard observed that phased array transducer technology seemed to be a viable NDT method when very definitive quantitative/qualitative information is required. He also mentioned that phased array transducers are useful on both thin and thick work pieces, and that signal to noise ratios were greatly improved, usually on the order of 10 to 20 dB to 1.

Forgings

Another NDE application that uses phased arrays is inspection of large forgings like rotor shafts for turbines or components for nuclear reactors. Since the geometry of many forgings requires a multitude of angles for the in-service inspections and during manufacture, phased array probes designed for beam steering can be used. Wüstenberg *et al.* (1993) discusses the use of two specific phased array probes:

Direct-coupled linear phased array probes are used to generate longitudinal waves for turbine rotor shaft inspections. These arrays consist of 16 elements with 2.7 MHz center frequency. The probe can be adapted to the curved surfaces of turbine rotor shafts and is able to detect a 0.6 mm flat-bottom hole within a distance of 1 m. The angle of the beam may be varied ±30°. Furthermore, the angle may be incremented stepwise with a minimum step of 0.3°.

Linear phased arrays mounted on *Perspex wedges* produce different types of waves (particularly shear waves) with a variation of either the skewing angle, the angle of incidence, or both.

The use of the these probes is unique in this application because the phased steering techniques are combined with echotomography.

Composites

Lethiecq *et al.* (1994) used a 3.5 MHz, 72-element phased array for an imaging system used to detect defects in carbon fiber composites. The objectives of the system were as follows:

- to test composite plates of 2 cm maximum thickness in immersion;
- to perform 100% examination of the plates with resolutions on the order of 2 mm or better;
- to detect planar and volumetric defects as well as clouds of micro- defects in real time;
- to allow determination of the size and location of defects.

A focal distance of 40 mm in water was chosen, since the thickness of tested plates was not to exceed 20 mm. A scan width of 80 mm was established in order to examine relatively large plates. The transducer itself was composed of 9 groups of 8 elements. An individual group was given a particular firing sequence which created the focal depth. An adjacent group of elements was then activated and given another firing sequence, and so on, so that the focal spot was moved across the composite.

In order to detect, size, and locate the different types of defects, two types of images were employed:

- A transmission *C*-scan image (each pixel shows the amplitude of the signal transmitted once through the plate), for which two identical transducers are used. This mode was designed to be associated with mechanical scanning of the plate or the transducers.

- A reflection B-scan image, for which the same array operates as transmitter and receiver. This mode was designed for use with mechanical scanning or manual inspection.

Tests performed on carbon-epoxy composite plates of thickness 5 mm and plastic plates of thickness 17 mm showed that in transmission mode the size of large artificial defects or delaminations can be evaluated with an uncertainty of 1 mm to 3 mm. The depth of defects can be determined with an uncertainty of 0.5 mm in reflection mode.

3.4.2 Potential Applications

To this day, there is no documentation of the usage of phased arrays in NDE of civil structures and materials. However, these sensors offer some attractive features and improvements over conventional probes and may be perfectly suitable for certain applications frequently encountered in this area. In Fig. 3.8 some proposed applications to typical infrastructure components, assemblies and members are shown.

Fig. 3.8(a) shows various welding defects such as hidden cracks, incomplete fusion defects and porosity, all of which are suitable for phased array inspection. Combined steering and dynamic focusing can insonify the entire welded area to locate porosities. This same concept can be applied along the weld boundary to locate fusion defects. Steering along the bottom of the member near the weld will reveal any hidden cracks which normally are not detected by the conventional angle-beam transducer. Also, several different angle-beams of varying angle of incidence in steel are usually required in order to pick up each of these defects. It is evident that from one position, a single phased array can identify numerous types of defects in a short amount of time.

Pin-hanger assemblies are another potential candidate for phased array testing, as shown in Fig. 3.8(b). Cracks usually develop below the hanger plate, but straight-beam and angle-beam probes are not always able to detect them because of shadowing effects. In other words, the crack is out of the range of the transducer's ultrasonic beam. Placing a phased array on the pin nut will eliminate this problem since the beam can be steered and focused along the surface of the pin. Often the nut has a

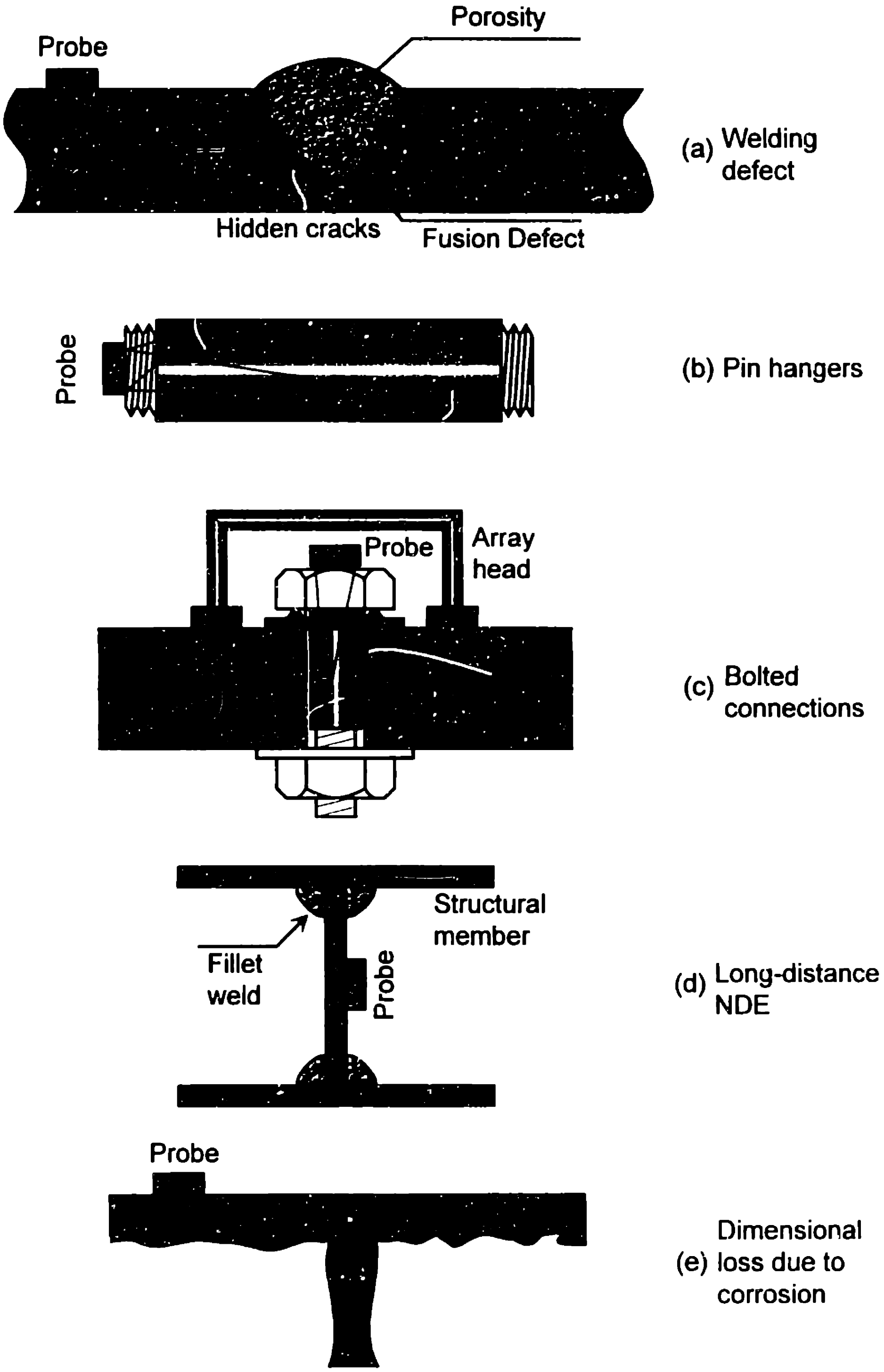

Figure 3.8: Potential phased array applications in civil infrastructure: (a) butt welds, (b) pin-hangers, (c) bolted connections, (d) long-distance NDE in beams and (e) dimensional loss due to corrosion.

smaller diameter than the pin, resulting in a shoulder which prevents direct inspection. However, by reflecting the beam off the opposite end of the pin, it is possible to locate the crack from the other side.

Bolted connections (Fig. 3.8(c)) may develop cracking in the bolt itself or in the bolted member. In the former case, the phased array may be positioned directly on the bolt nut and the beam may be dynamically focused and steered simultaneously along the length of the bolt. The latter may require a slightly more sophisticated array arrangement in order to effectively locate a crack. This is done by grouping the array elements in a ring. This allows rapid detection of cracking which may propagate from the circumference of the bolt into the member.

Another application is long-distance detection of defects in large members such as the built-up section shown in Fig. 3.8(d). In this arrangement, the sensor is positioned on the web and is used to scan the beam along the fillet weld in the axial direction. The phased array is especially advantageous when only single-sided access is available.

Members often suffer dimensional loss due to corrosion (Fig. 3.8(e)) and require accurate thickness measurements to determine the useful load-carrying capacity. Such testing is extremely tedious when conventional straight-beam probes are used. An improved method is to employ a phased array at one end of the member and scan along the corroded surface.

Several other interesting arrangements are possible. Phased arrays may be used for detailed inspection of transverse fissure defects in steel rail. These defects are often masked by longitudinal shelling, making normal beam probe detection virtually impossible. By banking the beam against the bottom surface of the rail, it may be possible to target the hidden defect and pick up the received signal in a pitch-catch configuration.

Piping and tube welds offer another possibility for phased array applications. In this case, the probe is situated a distance from the weldment and can send a guided wave through the relatively thin pipe thickness.

Finally, it may be worth investigating ways to steer the ultrasonic beam through the web of a girder by placing the transducer on the center of the top flange. This is particularly useful for single-sided access where cracks are growing in the bottom of the web, particularly in the vicinity of bolted and welded connections or lateral stiffeners.

3.5 Theoretical Modeling of the Phased Array Pressure Distribution

3.5.1 Background

In order to detect cracks at an appreciable distance, the array transducer should be capable of steering at large angles. At the same time, the accuracy, resolution and directivity will greatly influence the return signal. Accuracy and resolution are determined by the delay circuitry, while beam directivity is dictated by the geometry of the array. The quality of the sound field produced by linear phased arrays is mainly controlled by the inter-element spacing (d) and the element width (a).

Lemon and Posakony's (1980) study of element size on the sound field was limited to a single element. They also investigated the effect of element spacing on the steered wavefront of a linear array. McNab and Stumpf (1986) approached the array element model using a normal surface loading to predict the response of a single element. The superposition of these loadings resulted in a theoretical radiation field from phased sources, each of which is weighted by an amplitude and phase factor. The sound field of a 64-element linear array designed for treating intracavity hyperthermia was modeled by Buchanan and Hynynen (1994) using N cylindrical radiators of finite length, radius and separation as each of the transducers in the array. Lockwood *et. al.* (1996) introduced the effective aperture concept for reducing the required number of elements in the array while avoiding grating lobes.

A derivation of the far field pressure distribution and optimization for steering has been studied by Wooh and Shi (1997). Because this work characterizes beam steering behavior in structures according to various transducer parameters, it will set the theoretical benchmark for an experimental investigation to explore their results

Constants	
P_0	pressure at a distance r_0 from the acoustic source
r_0	a fixed radial distance from a simple source
f_0	center frequency of transducer
j	$\sqrt{-1}$
c	material wavespeed
θ_s	steering angle
$\Delta\tau$	interelement time delay
Parameters	
d	center-to-center element spacing
a	element width (azimuthal direction)
N	number of elements
Variables	
r	radial distance from acoustic source to arbitrary pressure point
θ	beam radiation angle
t	time
Functions	
$p(r,\theta,t)$	pressure at any arbitrary point in space and time
$p(r,\theta_s,t)$	pressure in the direction of a specific steering angle
$H(\theta)$	directivity function for phased arrays
$H_1(\theta)$	modulation function
$H_2(\theta)$	directivity function for discrete point sources
q	main lobe sharpness factor

Table 3.1: Notation used in phased array pressure modeling.

and confirm the validity of the optimization scheme. The notation used in this study is in accordance with Wooh and Shi and is given in Table 3.5.1.

3.5.2 Point Source Model

The point source provides the basis for all subsequent modeling development. Conceptually, a point source (or *simple source*), may be thought of as a pulsating sphere emitting ultrasonic vibrations into an acoustic medium. By definition, the radius of a point source is much smaller than the wavelength of its emissions, such that $a \ll \lambda$. The pressure at any point may be expressed as a function of time and radial distance

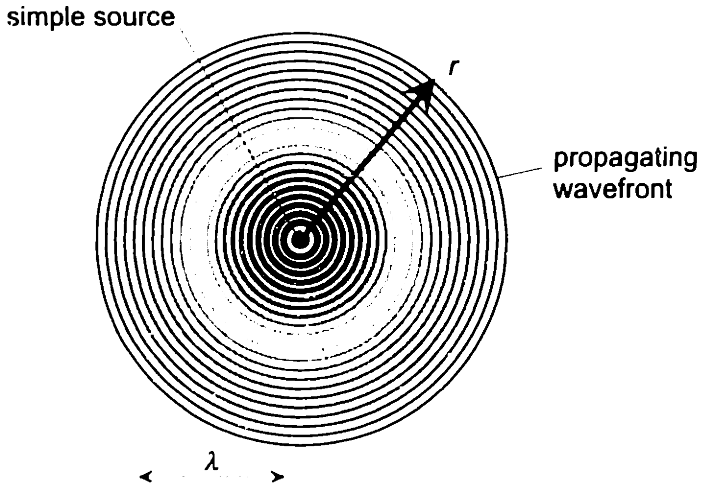

Figure 3.9: A snapshot of a wave emitted by a simple source.

from the acoustic source:

$$p(r, t) = \frac{P_0}{r_0} \exp[j(\omega t - kr)]. \tag{3.6}$$

Consequently, the pressure is uniform at a given radius but varies sinusoidally with time. The pressure itself drops off inversely with r. A snapshot of a disturbance created by a simple source is shown in Fig. 3.9. In this example, the concentric rings represent the propagating wave, similar to ripples in a pond. The harmonic variation is shown by the alternating ring color, whereas the amplitude of the pressure is marked by the diminishing width of the rings.

3.5.3 Modeling Approach

The approach to this theoretical development is shown in Fig. 3.10. As a first-cut approximation, the phased array may be modeled as an assembly of discrete point sources, with a point-to-point separation of d. If successive elements are delayed by an amount $\Delta\tau$, then the total pressure at any arbitrary point $P(r, \theta)$ may be computed as the sum of the contributions from each individual point source.

However, since the phased array is composed of discrete elements having finite width, it is logical to extend this analysis by considering each element to be composed

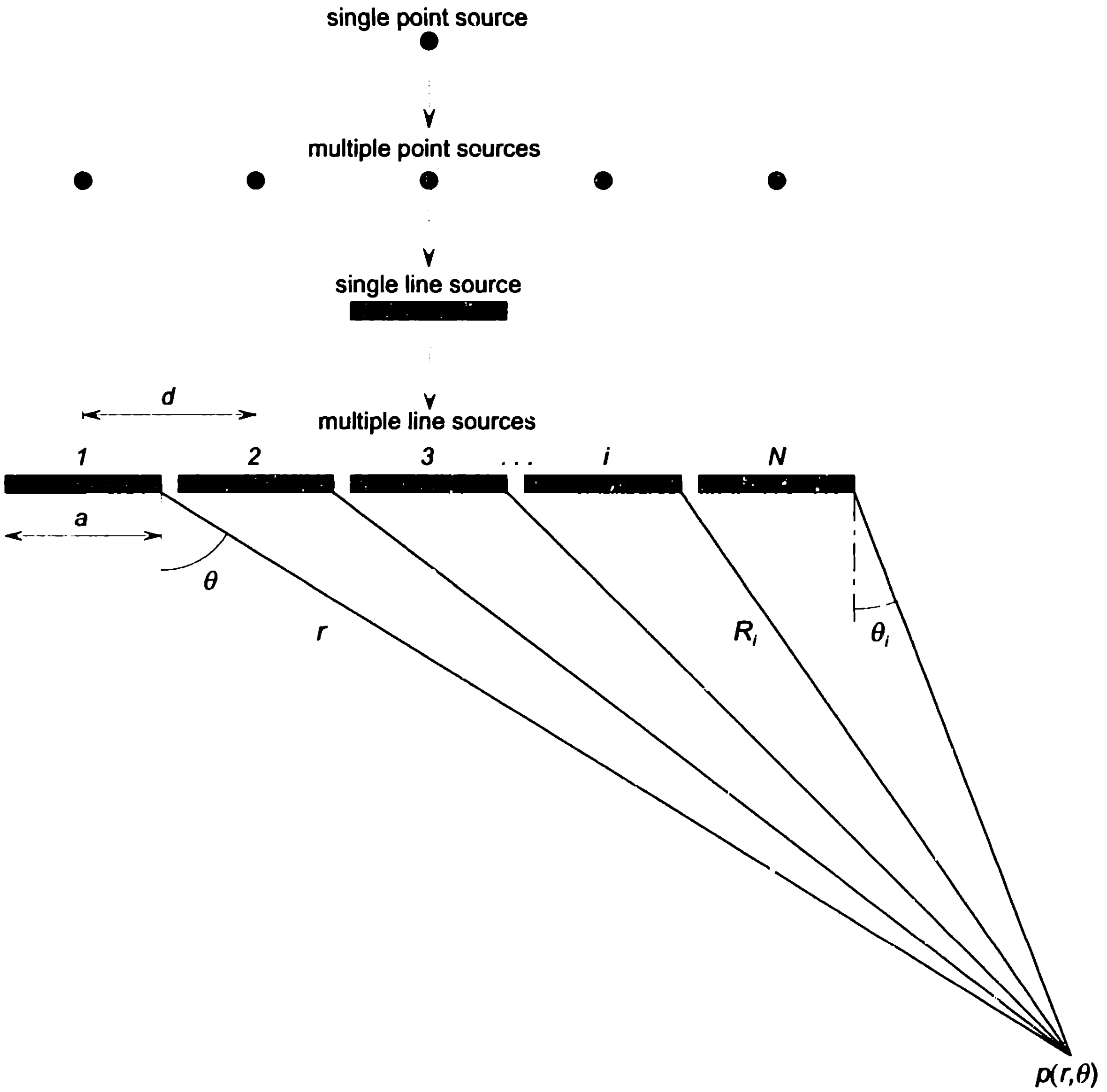

Figure 3.10: Approach to modeling the theoretical phased array pressure distribution: the array is an ensemble of multiple line sources, each of which is composed of an infinite number of point sources.

of an infinite number of point sources. The pressure field for this line source is obtained by integrating the contributions of all the point sources.

As shown in Fig. 3.10, the final step is to model the phased array as discrete line sources. The pressure distribution for the phased array is again obtained as the synthesis of the pressure contributions from each line source and may be expressed as

$$\begin{aligned} p(r,\theta,t) &= \sum_{i=1}^{N} p_i(r,\theta,t) \\ &= \frac{P_0}{r}\mathrm{sinc}\left(\frac{ka\sin\theta}{2}\right)\frac{\sin N\left(\frac{\omega\Delta\tau - kd\sin\theta}{2}\right)}{\sin\left(\frac{\omega\Delta\tau - kd\sin\theta}{2}\right)}\exp\left(-j\frac{ka\sin\theta}{2}\right) \\ &\quad \times \exp\left[-j\left(\frac{\omega\Delta\tau - kd\sin\theta}{2}\right)(N-1)\right]\exp[j(\omega t - kr)] \end{aligned} \tag{3.7}$$

A detailed derivation for multiple point source and line source formulae is given by Wooh and Shi (1997).

3.5.4 Phased Array Directivity

If the sound field pressure $p(r,\theta,t)$ is normalized with respect to the pressure $p(r,\theta_s,t)$ at a specific steering angle θ_s, then the so-called directivity function, $H(\theta)$ may be written as:

$$H(\theta) = \left|\frac{p(r,\theta,t)}{p(r,\theta_s,t)}\right|, 0 \le H(\theta) \le 1 \tag{3.8}$$

The directivity pattern for an ensemble of discrete point sources is given by

$$H(\theta) = \left|\frac{\sin\left[\frac{\pi d(\sin\theta_s - \sin\theta)}{\lambda}N\right]}{N\sin\left[\frac{\pi d(\sin\theta_s - \sin\theta)}{\lambda}\right]}\right| \tag{3.9}$$

For phased arrays, the directivity function is found to be the product of a modulation function $H_1(\theta)$ and the directivity function $H_2(\theta)$ for discrete point sources:

$$H(\theta) = H_1(\theta) \cdot H_2(\theta) = \left| \frac{\sin\left(\frac{\pi a \sin\theta}{\lambda}\right)}{\frac{\pi a \sin\theta}{\lambda}} \right| \times \left| \frac{\sin\left[\frac{\pi d(\sin\theta_s - \sin\theta)}{\lambda} N\right]}{N \sin\left[\frac{\pi d(\sin\theta_s - \sin\theta)}{\lambda}\right]} \right| \tag{3.10}$$

It can be shown from Fig. 3.11 that the modulation function $H_1(\theta)$ has little effect on the overall beam directivity provided θ is small or the ratio of a/λ is small. Thus, $H(\theta) \approx H_2(\theta)$ is a good approximation in most cases.

A typical directivity plot is shown in Fig. 3.12 in which the beam is steered at $\theta_s = 30°$. As an aid in studying the influence of d on the directivity behavior, the plots show the effect of three values of d/λ: 0.2, 2, and 0.5.

3.5.5 Discussion and Remarks

Several important observations can be made from Fig. 3.12. When $d/\lambda = 0.2$, grating lobes are suppressed but the directivity is rather poor, with $q \approx 0.2$. Now if $d = \lambda$, the directivity is superior ($q \approx 0$), but the existence of four additional grating lobes at -90°, -30°, 0°, and 90° makes steering extremely difficult. As expected, the optimum performance is obtained at $d = \lambda/2$. The main lobe sharpness factor is quite low ($q \approx 0.1$), and grating lobes have vanished.

By analyzing the locations of the main and side lobe peaks, it can be shown that there is an upper limit, d_{max} on the interelement spacing in order to suppress grating lobes[2]

$$d_{max} = \frac{\lambda}{1 + \sin\theta_s} \tag{3.11}$$

---

[2] It should be noted that Eq. 3.11 is a first order linear approximation to a Taylor's series expansion. A second order solution includes the contribution of a, element width.

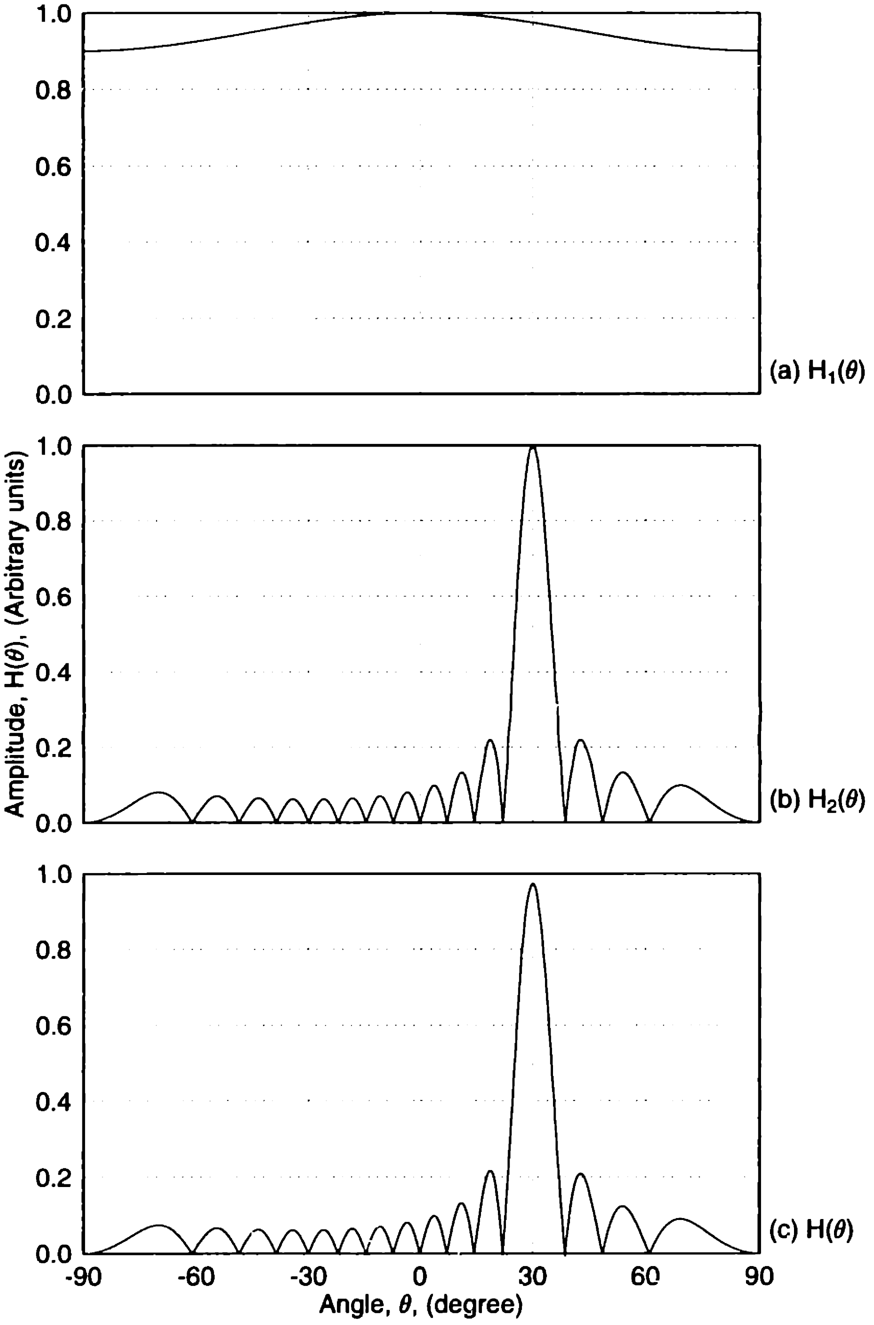

Figure 3.11: Effect of modulation function on phased array directivity: (a) the modulation function, $H_1(\theta)$, (b) the directivity of discrete point sources, $H_2(\theta)$, and (c) the directivity for a phased array, $H(\theta) = H_1(\theta) \times H_2(\theta)$.

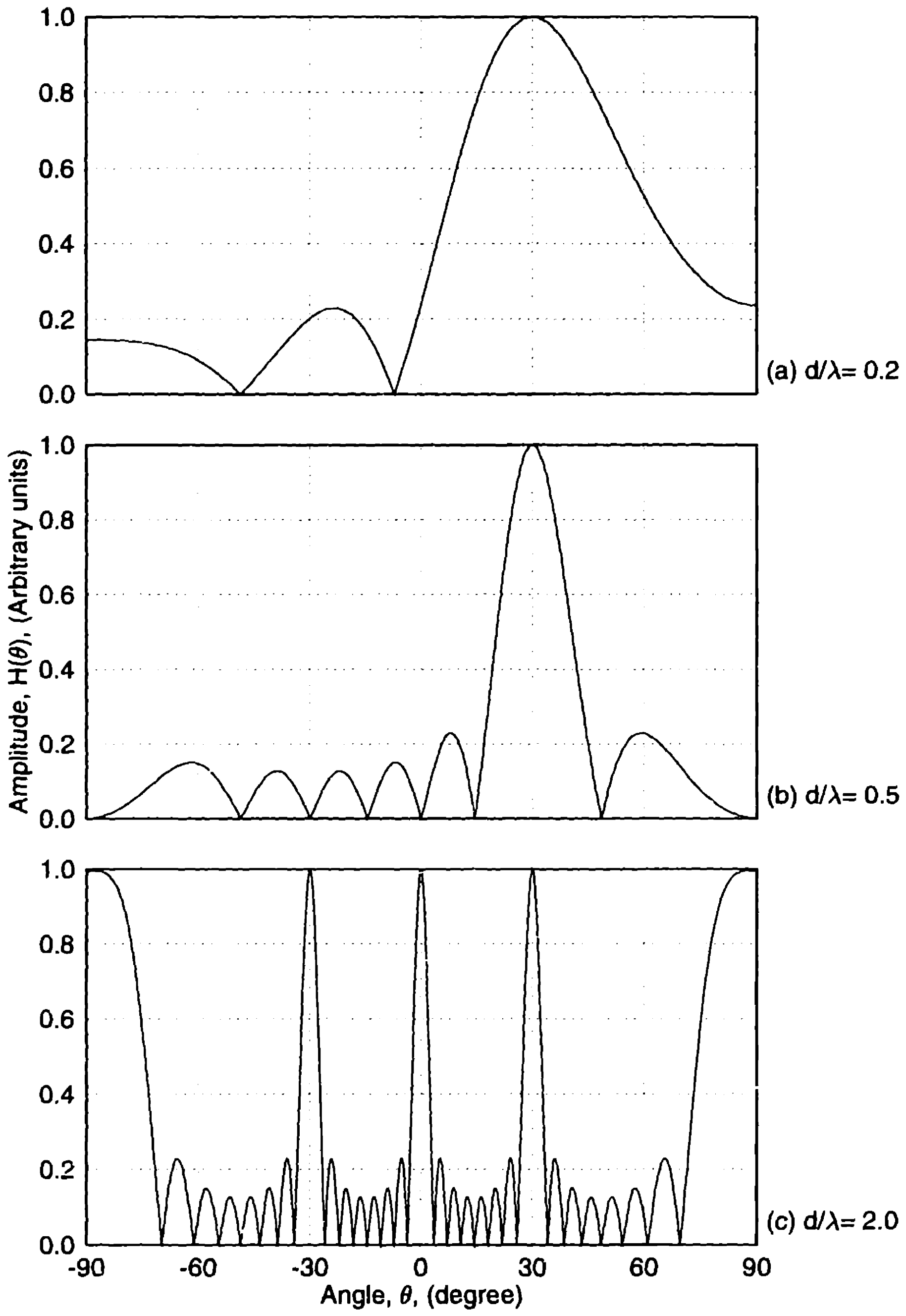

Figure 3.12: Theoretical directivity curves at $\theta_s = 30°$, showing the effect of the ratio of interelment spacing to wavelength for three distinct regimes: (a) d/λ=0.2, resulting in very broad directivity, (b) d/λ=0.5, the optimum directivity and (c) d/λ=2.0, very narrow main lobe coexisting with other grating lobes.

The literature usually reports that $d \leq \lambda/2$ to eliminate side lobes. This is true if $\theta_s = 90°$. However, if one is only interested in steering up to 30°, then d_{max} is actually $4/3d$. This observation implies that the usual requirement on interelement spacing does not need to be met if the steering angle is less than 90°. From a practical viewpoint, the array fabrication may be easier if the required steering angle is small.

Analysis the zero-crossing locations of the main and side lobes results in a useful expression for characterizing the width of the main lobe:

$$q = \frac{1}{\pi}\left[\sin^{-1}\left(\sin\theta_s + \frac{\lambda}{Nd}\right) - \sin^{-1}\left(\sin\theta_s - \frac{\lambda}{Nd}\right)\right] \tag{3.12}$$

where $0 \leq q \leq 1$ and is defined as the *main lobe sharpness factor*. Since q is normalized with respect to π (180°), then it follows that for a value of $q = 1/2$, the width of the lobe is 90°, which is inadequate for properly resolving nearby defects in steel structures. Thus, q should be kept as close to zero as possible for optimum directivity. This is achieved by increasing N and d and decreasing λ. Locking the values of these parameters shows that q increases with increasing θ_s.

They key findings from this theoretical development can be summarized as follows:

- There is an optimum spacing between elements for a given steering angle and frequency.
- Increasing the number of elements will improve the directivity and decrease the main lobe width.
- The size of the element has negligible effect on steering performance.

These results lead to the experimental investigation presented in Chapter 5. This program will not only be used to assess the performance of phased arrays according to their beam steering behavior, but also to confirm the results listed above. It is anticipated that the corroboration of these findings with the experimental results will provide a useful guideline for designing phased array probes and understanding their behavior when applied to real structures.

Chapter 4

System Development

A 16-channel phased array system developed for investigating the feasibility of long-distance NDE is discussed in this chapter. The main components, including electronic hardware, transducer array, control software and interfacing, will be discussed in detail. Each topic will address the design criteria, component selection and fabrication/assembly techniques used for developing the sensor.

4.1 Overview

Most phased array systems have several sub-assemblies, each of which may be developed as a separate unit. This modular feature is useful for isolating and addressing a particular problem or design aspect in detail without having direct influence on the other components. Naturally, the final integration of the system requires perfect marriage, which is usually a matter of providing the correct electro-acoustic matching and connectivity between components. In this particular system, there are essentially five main areas of development:

1. Delay circuitry
2. Pulser circuitry
3. Transducer array
4. Transducer calibration assembly

5. Computer interfacing

Many of the components used in the hardware are controllable, and therefore require computer interfacing through parallel i/o cabling, GPIB for data acquisition and RS-232 for serial port communication. The electronic hardware consists of a 16-channel delay generator and high-voltage pulser circuit. Each of the 16 channels is dedicated to pulsing a specific array element after a certain time delay has expired. The result is an electronically controllable ultrasonic beam whose performance is assessed using a calibration assembly, which will be discussed in Chapter 5.

A conceptual diagram of the system layout is schematicized in Fig. 4.1. TTL logic trigger signals, furnished through an HP Function Generator, are used as inputs to all 16 channels. Data from a 192-bit i/o board installed in a PC manipulates individual delay channels to generate a delayed trigger source for each of the 16 pulser units. The pulsers are accordingly delayed and excite the piezo-element with a high voltage spike pulse.

The following sections will provide a more detailed description of each component, along with certain design considerations and fabrication techniques. For completeness, a brief review of the relevant literature will accompany each section, showing the design approaches and methods adopted in this work.

4.2 Delay Circuitry

Many different design approaches are used to create a flexible and controllable multichannel delay system and are described extensively in the literature (Buchanan and Hynynen, 1994; Scales *et al.*, 1994; McNab and Campbell, 1987; Lovejoy *et al.*, 1995; Armitage *et al.*, 1995; Hatfield *et al.*, 1994; Beardsley *et al.*, 1995). The circuit used in this work most closely resembles Beardsley's cascading delay arrangement of tapped delay lines and multiplexers.

One of the major difficulties encountered in a discrete component assembly is the complexity of the circuit since the i/o control increases rapidly with increasing channels. Naturally, the more channels available, the greater the flexibility and control

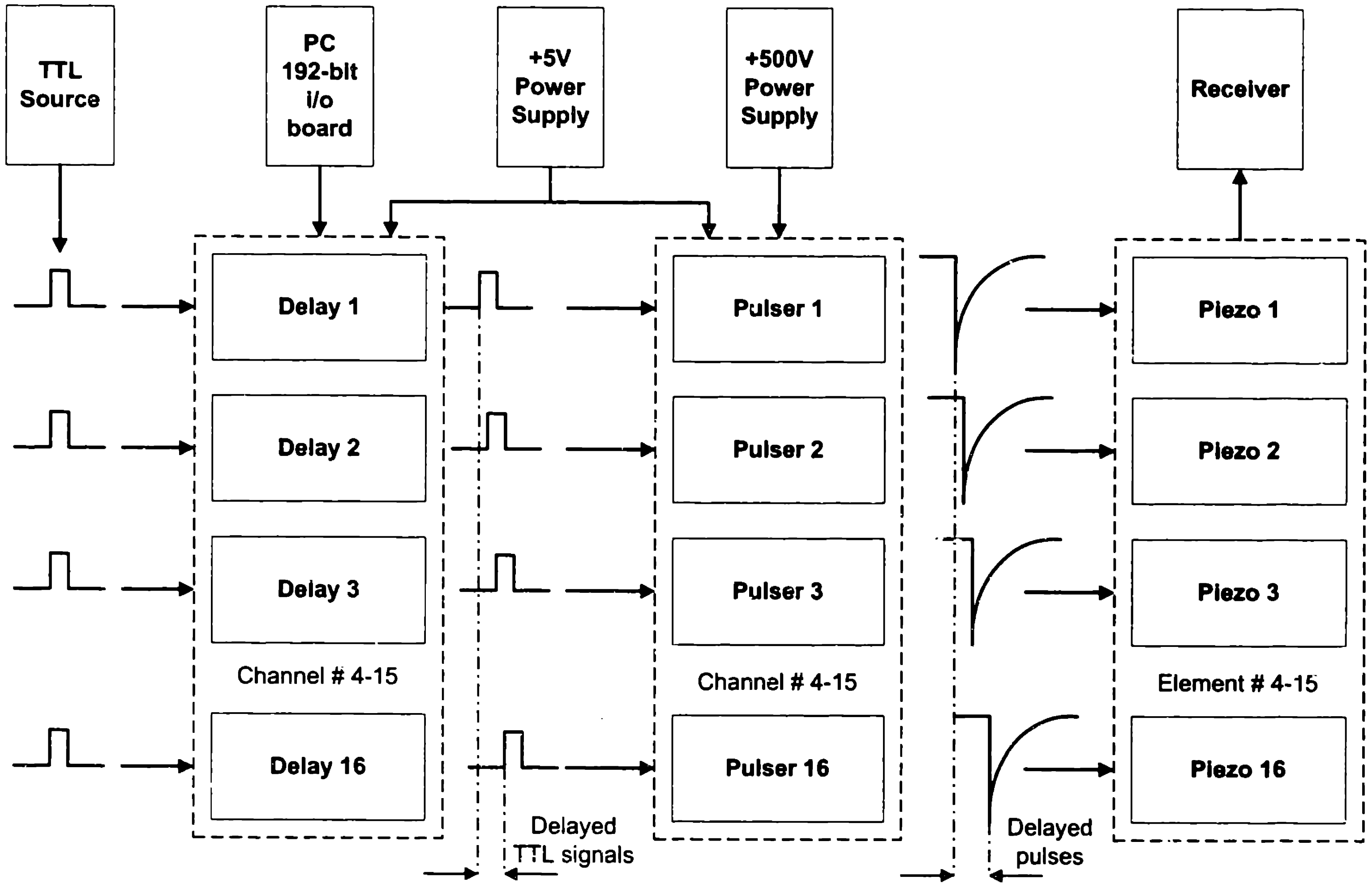

Figure 4.1: Schematic overview of the 16-channel phased array system.

Level	Delay (ns)
1 (coarsest)	0—500—1000—1500—2000
2	0—100—200—300—400
3	0—20—40—60—80
4 (finest)	0—5—10—15—20

Table 4.1: Cascade delay arrangement.

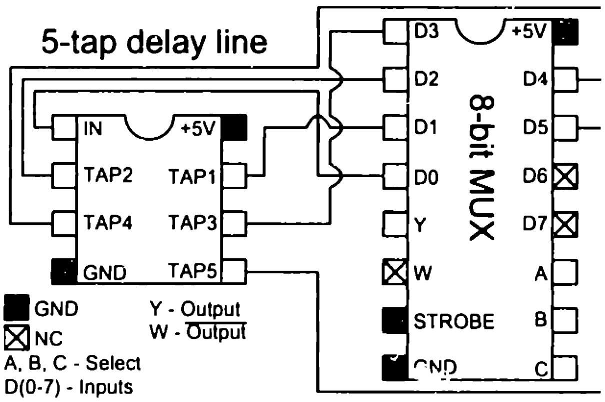

Figure 4.2: Delay line/multiplexer pin-outs and connection diagram.

of the ultrasonic beam. The important design considerations include the number of delay channels, the delay resolution (minimum delay) and the delay range (maximum delay). The actual delay circuit was prototyped on a breadboard.

4.2.1 Principle of Operation

The individual delays specified for each channel are created by using tapped delay lines and are controlled by 8-bit multiplexers. The delays are arranged in a cascade fashion with control shown in Table 4.1.

The first level in each channel is actually composed of a bank of four delay lines connected in series. The remaining levels only require one delay chip for the desired output. Accordingly, the total accumulated delay will equal the sum of delays for each level.

There are essentially two main components (integrated circuits) used in this circuit: 8-bit multiplexers (MUXs) and digital delay lines. A MUX is essentially a switching device which is given a number of inputs from which exactly *one* is selected (outputed) based on a prescribed bit combination. Hence, for an 8-bit multiplexer the Boolean equation is

$$\begin{aligned} Y \;=\; & D_0\overline{ABC} + D_1A\overline{BC} + D_2\bar{A}B\overline{C} + D_3\overline{AB}C + \\ & D_4AB\overline{C} + D_5A\overline{B}C + D_6\bar{A}BC + D_7ABC \end{aligned} \tag{4.1}$$

where Y is the output (i.e. the input that has been selected), A, B, and C are the i/o control bit values (0 or 1), and D_n is the nth input. For example, if the bits are set to $A = 0$, $B = 1$ and $C = 0$, then the corresponding output is $Y = D_2$.

A diagram of pin-outs and typical connection between a tapped delay line and multiplexer is shown in Fig. 4.2. The squares surrounding the two chips in Fig. 4.2 represent the actual pins; their function is labeled accordingly. Squares marked with an "×" do not require connection. The light squares get +5 V power while the dark ones are grounded. Data selection (i/o control) is provided by pins A, B, and C. Note that the input TTL signal, which is issued from an HP function generator, is connected to pin D0 of the MUX, resulting in no delay. The remaining delay line outputs are connected to the inputs of the MUX (D1–D5).

The digital delay lines used in this circuit all have five "taps", or five equal delay increments. The coarsest delays are provided by the 5-tap 500 ns delay lines, intermediate delays are available in a 5-tap 100 ns series, and the finest delays are created with 5-tap 25 ns delay lines. The chips are flexibly arranged so that the final output of each channel encompasses the required delay range with the minimum delay step. A schematic showing the operation of a single delay channel is illustrated in Fig. 4.3. As an example, the digram shows how a delay of 2495 ns is generated. An HP function generator provides a common TTL signal to all 16 channels. The TTL signal is a 5V peak-to-peak square wave set it burst mode having a minimum pulse width of 150 ns. This is the actual signal which gets delayed (according to the programmed delay for

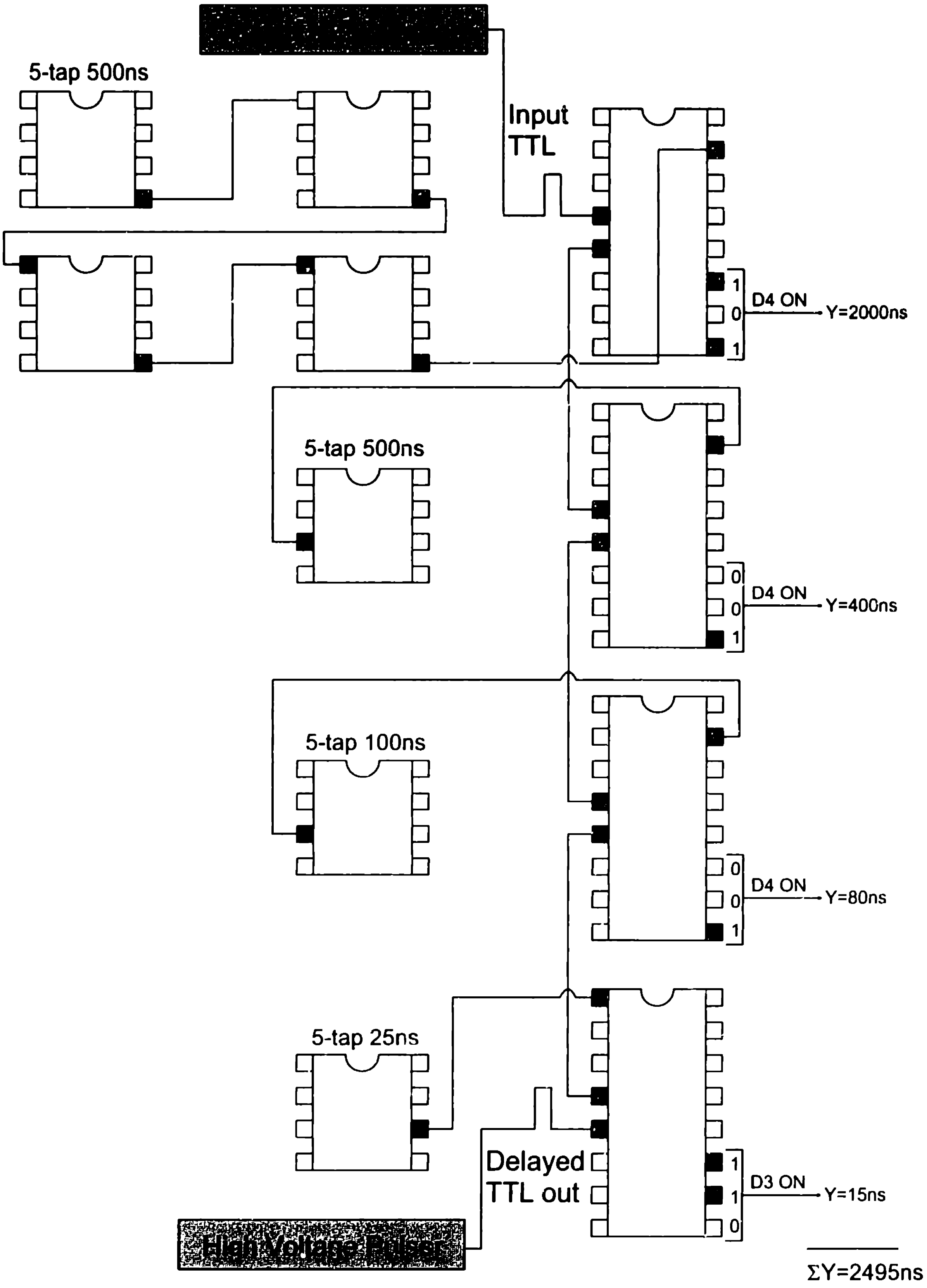

Figure 4.3: Schematic of typical delay channel.

each channel) and then fed to the pulser unit to create a high voltage negative spike pulse.

The top-level multiplexer receives a bit combination corresponding to a 2000 ns delay input, which is then cascaded to the second-level multiplexer. This one switches the 400 ns input based on its predetermined bit pattern, and the combined delayed TTL signal of 2400 ns is cascaded to the third-level multiplexer. At the third level, the signal is now delayed by an additional 80 ns, and finally sent to the bottom-level multiplexer which selects the 15 ns delay input thereby creating a total delay of 2495 ns which is then used as a trigger for the pulser.

4.2.2 Capabilities and Limitations

Unlike Beardsley's 8-channel partially *dependent* delay system, this circuit utilizes 16 *independently* programmable delay channels since the sharing of components across two channels was found to increase the electrical crosstalk significantly. The specifications for this circuit are provided in Table 4.2. This design also has a finer delay resolution of 5 ns and a maximum range of 2500 ns. Designed for ultrasonic transmission into either aluminum or steel, the circuit will allow for as many as 34 different steering angles, as shown in Table 4.3. The table displays the steering angle θ_s as a function of the interelement delay $\Delta\tau$ for three typical excitation frequencies (f_0=1, 2.25 and 5 MHz) according to:

$$\theta_s = \sin^{-1}\left(\frac{c_L \Delta\tau}{d}\right), \tag{4.2}$$

where c_L is the material's longitudinal wavespeed and d should be taken as $c_L/2f_0$, or $\lambda/2$, in order to minimize the effect of grating lobes. [1] With fewer than 16 channels in operation, the steering capability will increase. Note that there is a cutoff at 165 ns since this would result in a maximum total accumulated delay exceeding the range of the circuit.

---

[1] It should be noted that the steering angle is not physically dependent on frequency, but with the constraint that $d = \lambda/2$, one may indirectly explore the frequency behavior using $\theta_s = \sin^{-1}(2f_0\Delta\tau)$.

No. of channels:	16
I/0 per channel:	12
Total I/O:	192
Input signal:	TTL
Resolution:	5 ns
Range:	2500 ns

Table 4.2: Specifications for phased array delay generation circuit.

One can make several observations from Table 4.3 regarding the tradeoffs and limitations of the system. First, the delay range immediately confines the steering angles to a maximum of 71.8° in steel at a frequency of 5 MHz; lower frequencies will further restrict the steering angle. On the other hand, at 5 MHz, the large gaps between angles are somewhat disconcerting since the ultrasonic beam could easily pass over a defect which happened to lie within this blind zone. The lower frequencies create a smoother transition between angles, but it should be noted that the jumps enlarge as θ_s increases.

Despite these limitations, the system shows good balance and flexibility for various inspection schemes. For smooth steering within a narrow field of view, a 1 MHz piezoceramic may be used, whereas for coarse steering at large angles, 5 MHz will perform well in both steel and aluminum.

4.3 Pulser Circuitry

The function of the pulser circuitry is to create a high voltage waveform which can be used to excite the piezoelectric material. Since this is a multi-channel system, each pulser circuit must be replicated and dedicated to a specific piezoelement. The pulser unit has two sub-assemblies, a single high-voltage power source and sixteen pulse generators.

Delay	**θ_s in Steel**			**θ_s in Aluminum**		
$\Delta\tau$ (ns)	1 MHz	2.25 MHz	5 MHz	1 MHz	2.25 MHz	5 MHz
0	0.0	0.0	0.0	0.0	0.0	0.0
5	0.6	1.3	2.9	0.6	1.4	3.0
10	1.1	2.6	5.7	1.2	2.8	6.0
15	1.7	3.9	8.6	1.8	4.2	9.1
20	2.3	5.2	11.5	2.4	5.6	12.2
25	2.9	6.5	14.5	3.0	7.0	15.3
30	3.4	7.8	17.5	3.6	8.4	18.4
35	4.0	9.1	20.5	4.2	9.8	21.6
40	4.6	10.4	23.6	4.8	11.2	24.9
45	5.2	11.7	26.7	5.4	12.6	28.3
50	5.7	13.0	30.0	6.0	14.1	31.8
55	6.3	14.3	33.4	6.7	15.5	35.4
60	6.9	15.7	36.9	7.3	17.0	39.2
65	7.5	17.0	40.5	7.9	18.4	43.2
70	8.0	18.4	44.4	8.5	19.9	47.5
75	8.6	19.7	48.6	9.1	21.4	52.2
80	9.2	21.1	53.1	9.7	22.9	57.4
85	9.8	22.5	58.2	10.3	24.4	63.6
90	10.4	23.9	64.2	10.9	25.9	71.4
95	11.0	25.3	71.8	11.5	27.5	
100	11.5	26.7		12.2	29.1	
105	12.1	28.2		12.8	30.7	
110	12.7	29.7		13.4	32.3	
115	13.3	31.2		14.0	34.0	
120	13.9	32.7		14.6	35.7	
125	14.5	34.2		15.3	37.4	
130	15.1	35.8		15.9	39.2	
135	15.7	37.4		16.5	41.0	
140	16.3	39.1		17.2	42.9	
145	16.9	40.7		17.8	44.8	
150	17.5	42.5		18.4	46.8	
155	18.1	44.2		19.1	48.9	
160	18.7	46.1		19.7	51.1	
165	19.3	47.9		20.3	53.3	

Table 4.3: Available steering angles in steel and aluminum for the 16-channel system with 5 ns delay resolution.

4.3.1 High Voltage Power Source

A schematic of the high voltage power supply is shown in Fig. 4.4. [2] The system DC power supply is shown at the top level. The power supply requires standard 110/120 AC which is converted to 5V DC. This 5V DC source is used to power all electronic components, including the digital delay chips (MUXs and delay lines). The second high voltage component is a 20-pin analog to digital voltage selector. The output of this device is adjustable from 0 to 255 volts using the 8-bit data selectors (pins 7–14) and is fed to the control pin of the high voltage power supply unit. In order to meet system power requirements, two EMCO programmable high voltage power supplies are used; each EMCO unit supplies power to 8 channels. The input pin of the high voltage power supply requires 15V DC which is provided by a regulated DC to DC converter (5V to 15V). Each output pin furnishes the programmed DC voltage to 8 pulser channels allowing for a high voltage pulse waveform.

4.3.2 Pulse generator

Many applications require high voltage, high speed, and high current at low duty cycles such as ultrasonic cleaning equipment, flaw detection, medical imaging, and test instruments. This particular circuit is a variation of a high side open drain pulser provided in an electrical handbook (Supertex, 1996). This option was selected to satisfy the requirements of using a 500V maximum voltage. Complementary N- and P-channel DMOS transistors (TN2105, TP2105, TN2106, TP2106 and VN0550) are used for their low threshold voltages, low input capacitances and high output current capabilities, which are essential features for generating the high-voltage pulses used in this application. Additionally, the TO-92 is a cost-effective package option, saving board space.

The high-voltage pulser used in this phased array control circuit is drawn schematically in Fig. 4.5. The input signal is a standard TTL which is used to trigger the pulser circuit. The TP- and TN-channel transistors allow the negative and positive

---

[2] All ground pins of the components shown in the diagram are tied together.

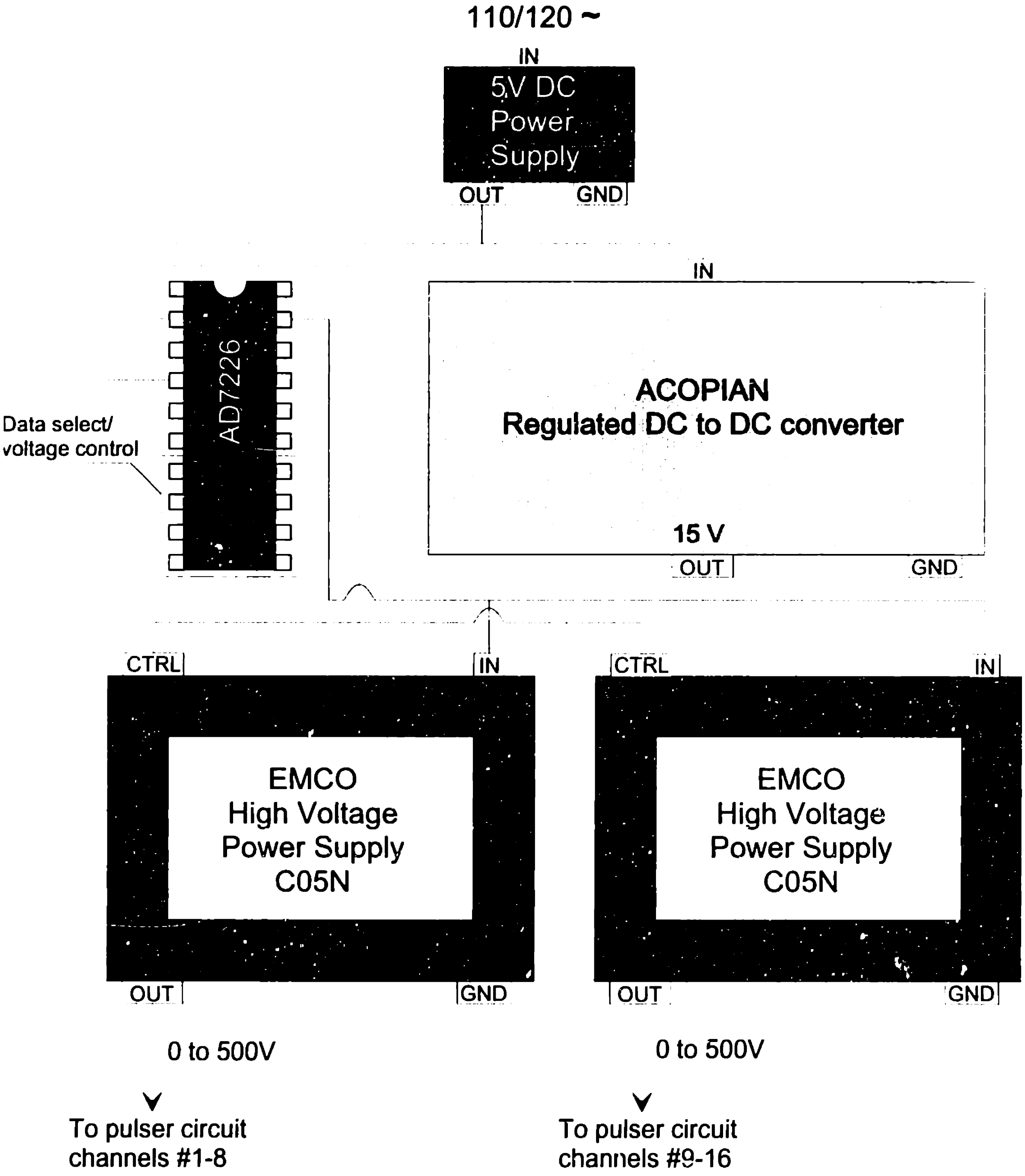

Figure 4.4: Schematic of high voltage power supply for pulser circuits.

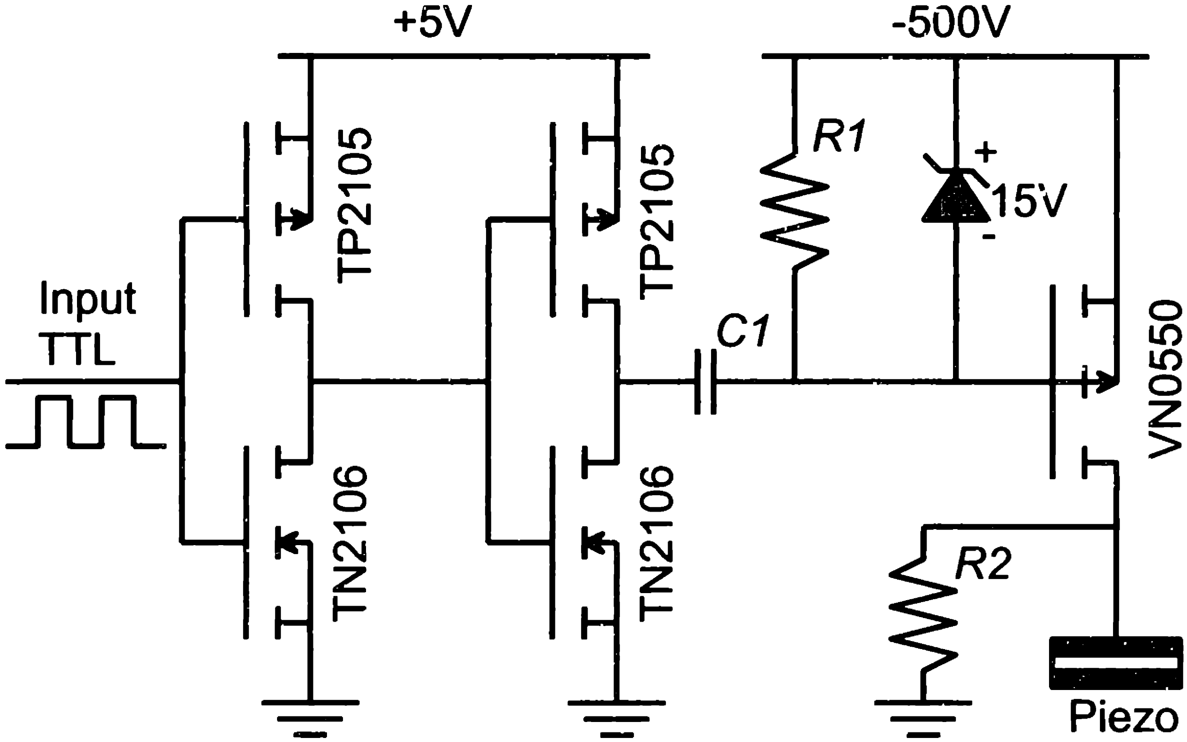

Figure 4.5: Schematic of a typical high-voltage pulser channel.

edges, respectively, of the input signal to pass through, which is then amplified to the desired voltage using the VN0550 transistor. The parallel combination of a $15V$ zener diode and resistor $R1$ ($\approx 100k\Omega$) are used to provide a high-voltage discharge mechanism as a safety precaution. The resistor $R2$ is used to match the impedance of the piezo-material and has a typical value of $\approx 1M\Omega$. Finally, the interfacing capacitor between the low and high voltage segments of the circuit has a value of approximately $0.01\mu F$. Several auxiliary capacitors, not shown, are used between the high voltage line and ground to stabilize the voltage.

A typical response under load showing the characteristic pulse shape is given in Fig. 4.6. Programmed at 225 V, the pulse is seen to have a width of approximately 10μsec, if measured from baseline to 80% recovery. The spike itself spends roughly 500 nsec at the maximum negative voltage. For this particular pulser design, the pulse width has been minimized but can be made even narrower using a revised layout and

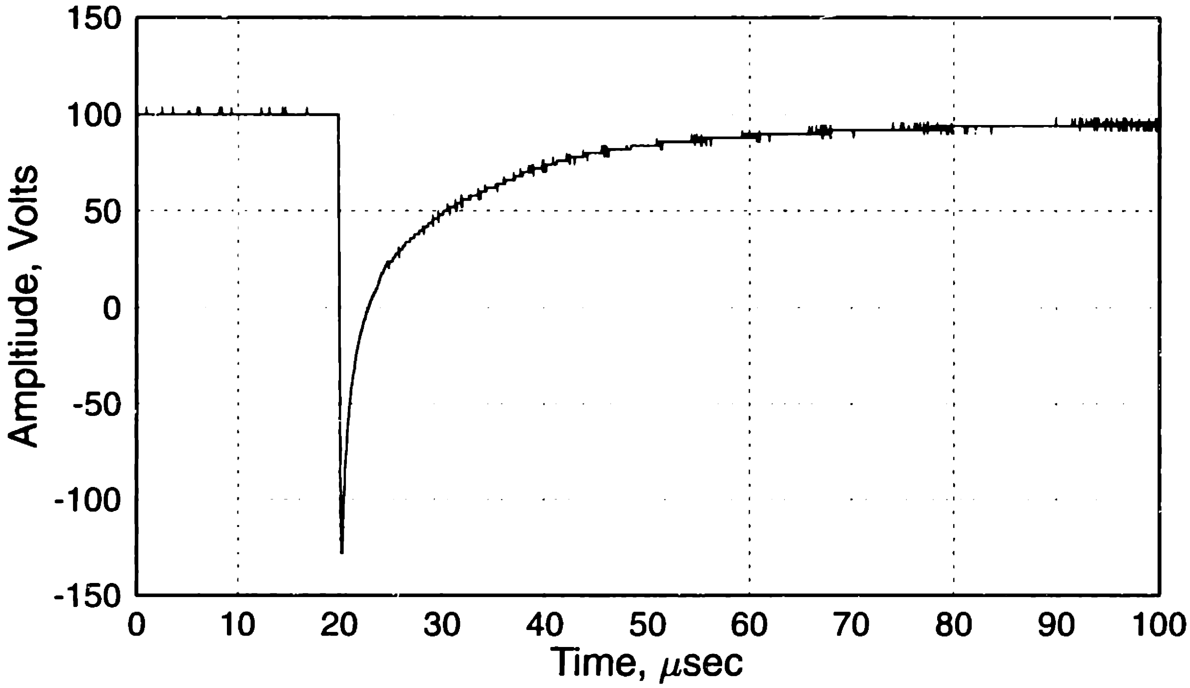

Figure 4.6: A typical response from a pulser channel under load: 225 V negative spike pulse.

more advanced circuit components. The specifications for the high voltage power supply and pulse generator are given in Table 4.4.

4.4 Transducer Design and Fabrication

Linear phased arrays are generally assembled in one of two ways: monolithically or slotted (reference). For the inspection of long members such as steel beams and

No. of channels:	16
Input:	TTL
Pulse amplitude:	0—500, 1V steps, programmable
Pulse width:	10 μsec
Repetition rate:	100 Hz—5 KHz, continuous
Polarity:	negative
Pulse type:	spike

Table 4.4: Specifications for pulser and high voltage circuitry.

plates, linear arrays are a good choice since the width of the member is normally not significantly longer than the width of the array itself. Monolithic arrays typically involve the removal (etching) or the electrode off the piezoelectric material to create gaps between the remaining electrode elements. This configuration often involves a significant amount of crosstalk. Slotted arrays are made with cuts through the active element which separate the elements individually and are attractive because the electro-mechanical crosstalk between neighboring elements is minimized.

4.4.1 Design Requirements

In addition to the design-related parameters (N, f, a and d), there are some important mechanical properties which can greatly enhance or severely compromise the performance of the transducer, depending on the care made in their selection. This includes a well damped acoustic backing and properly matched front layer(s).

The backing is generally a highly damped attenuative material that helps to trap the back-propagated energy and prevents it from interfering with the forward transmitted energy. Such a device will maximize the transmitted energy into the target material. However, upon return, the backing once again re-absorbs the energy so that received signals may be too weak to detect. Hence, for through-transmission systems, the transmitting probe should be heavily damped, while the pulse-echo transducer requires a medium damping.

Silk (1984) introduces the concept of "energy trapping" within the disc by

$$W = \left(\frac{Z_C - Z_L}{Z_C + Z_L}\right)\left(\frac{Z_C - Z_B}{Z_C + Z_B}\right) \tag{4.3}$$

where W represents the square root of the trapped energy after one oscillation , Z_B, Z_L and Z_C are the impedances of the backing, load and ceramic, respectively. In a simple case, W would provide the amplitude ratio of cycle n to cycle $n-1$.

A high value of $W(> 0.75)$ leads to excessive ringing, while low values (< 0.1) imply very short (broad bandwidth) transducer response. An acceptable value of W for general ultrasonic applications is 0.3. From this, one may obtain the required backing impedance Z_B:

$$Z_B = Z_C \left[1 - 0.3\left(\frac{Z_C + Z_L}{Z_C - Z_L}\right)\right]\left[1 + 0.3\left(\frac{Z_C + Z_L}{Z_C - Z_L}\right)\right]^{-1} \tag{4.4}$$

Persson and Hertz (1985) provide both the experimental and theoretical response of a 1 MHz, 10 mm diameter probe to various backing impedances. Their results lead to the following conclusions as the backing impedance is increased:

- There is a marked decrease in the number of ring-down cycles.
- The frequency spectrum is broadened.
- The return signal amplitude is decreased.

The second important ingredient in transducer fabrication is the selection of one or more properly matched front layers, or "shoe" materials. Front layers act as acoustic transformers and can have a pronounced effect on the performance of the transducer. The derivation of required impedance for one, two or more layers can be found in DeSilets (1978). An excellent experimental study showing the response of various multi-layer probes is given in Persson and Hertz (1985). Their results are corroborated with the use of a Mason model to predict the received signal in a pulse-echo ultrasonic immersion test.

In general, for a single layer design, the required matching impedance should be the harmonic mean of the impedance of the materials on either side (i.e. the piezoceramic and the load material):

$$Z_a = \sqrt{Z_L Z_C} \tag{4.5}$$

where Z_a is the matching layer impedance, and Z_L and Z_C are the impedances of the load and ceramic, respectively.

In a two-layer system, the required impedances may be written as

$$Z_a = Z_L^{3/7} Z_C^{4/7} \tag{4.6}$$

$$Z_b = Z_L^{6/7} Z_C^{1/7} \tag{4.7}$$

where Z_a and Z_b are the impedances of the first and second layers.

In order to maximize the energy transmitted into the load material, the thickness of the matching layer, t_a, should be taken as

$$t_a = \frac{\lambda}{4} = \frac{c_a}{4f_0} \quad . \tag{4.8}$$

where λ is the wavelength in the layer, c_a is the wavespeed in the layer, and f_0 is the center frequency of excitation. Persson and Hertz show that values of t_a outside the range of $\lambda/4$ will not only reduce the amplitude of the return signal, but also distort the center frequency.

4.4.2 Sensor Fabrication and Assembly

The assembly and fabrication techniques used for the prototype sensor are shown in Figs. 4.7–4.9. A revised technique showing improved performance is discussed at the end of this fabrication procedure.

The first step in fabricating the transducer is shown in Fig. 4.7. Essentially, a PZT plate is bonded to a tungsten-loaded backing material using a silver-filled epoxy. The tungsten used in this backing is in powder form, having a mean particle size of 0.5 micron to ensure adequate dispersion and suspension in the epoxy. A tungsten-to-epoxy mixing ratio of 3:1 is used to create a strong damping effect for the back-propagating acoustic vibrations. Once the respective amounts of tungsten and epoxy are weighed and measured, they are mixed together in a cup for about five minutes, until a uniform consistency is obtained.

Meanwhile, a small box-like aluminum mold is prepared by (1) tightening all the nuts which hold the panels together, (2) cleaning the interior surfaces, and (3) spraying the interior with a mold release agent. The mixture is poured into the mold and left to cure for 24 hours. After the backing is fully cured, the nuts are removed and the backing is extracted by carefully prying open the side panels of the mold.

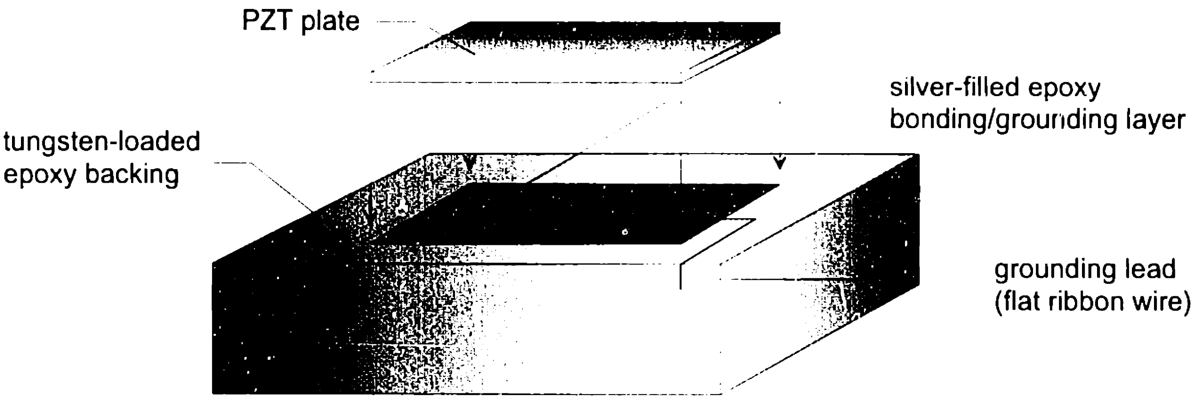

Figure 4.7: Bonding the PZT active element to its backing.

Figure 4.7 shows the actual placement of the PZT plate onto the center of the backing. The PZT is bonded to the backing using a thin layer of conductive silver-filled epoxy. Since one side of the plate requires electrical grounding, the conductive epoxy is also used to connect a ground wire to the PZT. In order to maintain contact between the PZT and backing, the ground lead used is a flat silver ribbon wire.

The next step in the array fabrication process, shown in Fig. 4.8, consists of cutting the PZT plate to form slotted elements and making lead-terminal connections to each individual element. Prior to cutting, the backing is secured in a vice-like assembly with bonded PZT facing up. In the thickness direction, the cuts are made 35 mm deep, with an extra 5 mm uncut. Ideally, the elements should be totally isolated by cutting all the way through the PZT. Unfortunately, the elements are extremely fragile and 35 mm is the maximum depth required to ensure that they all remain intact. Additionally, a full cut into the PZT may cause a partial grounding isolation which must be avoided. In the width-direction, the cuts are made all the way across the face of the plate.

The slots in the PZT are made with a precision diamond saw blade mounted to a rotary device on a horizontal milling machine. The position of the blade can be manually adjusted, with an accuracy of 0.01 mm. The thickness of the blade will actually determine the minimum gap between elements. Since it is has already been shown in Chapter 3 that the element width a has virtually no influence on

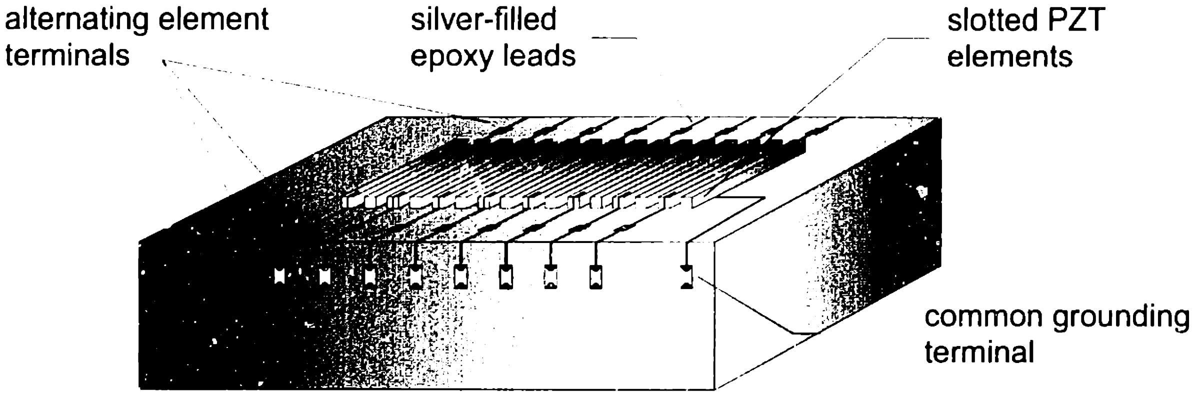

Figure 4.8: Lead and terminal arrangement on the mold.

the transducer directivity, there is some flexibility in selecting an adequate blade. Obviously, the thickness must be less than d.

After cutting, the array is now ready for electrical connections. This is done by "painting" conductive lines using the silver-filled epoxy from the very edge of each element to its respective terminal. The terminals are thin plastic strips with copper tab hourglass-shaped pads. Rather than using a 16-tab terminal, only one terminal strip with eight tabs is glued just in front of each side of the array. This facilitates in drawing the conductive lines without creating an accidental short-circuit. Another set of strips is glued to the adjacent face of the backing and the silver-filled epoxy lines are extended to these strips.

The final steps are shown in Fig. 4.9. This includes the placement of the backed PZT inside the large aluminum mold and connections from the terminals to a circular connector.

At this point, the next set of connections are made from the backing terminals to a plastic 28-pin circular connector using an extremely thin (36 AWG) enamel-coated wire. The enamel coating insulates the wire and is therefore useful for preventing any short-circuits within the final assembly. A solder iron is used to bond the wire to the copper tabs.

A second aluminum mold is used to cure an exterior epoxy cover onto the backing. A hole is cut out from one of the mold's panels so that a circular pin connector may

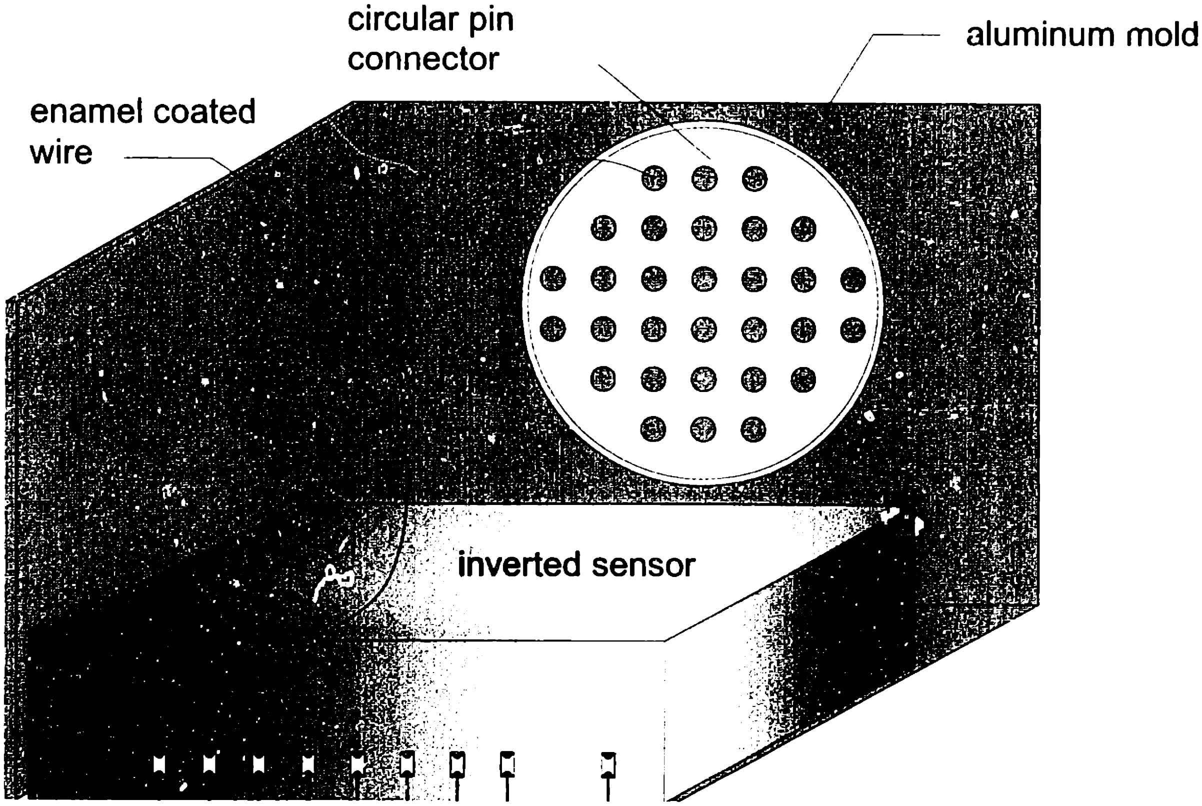

Figure 4.9: The sensor is inverted inside the exterior mold and connections are made from backing terminal to circular pin connector with enamel coated wire.

be attached and eventually bonded to the outside of the sensor. This outside epoxy actually has no function as far as the transducer is concerned, but it is necessary in order to protect the sensor along with its interior wiring and also to attach the connector for interfacing the phased array to the pulser circuit. Each one of the 16 enamel-coated wires is soldered onto a gold-plated pin which fits snugly into the hole of the circular connector. Once the connections are completed, all contact points are tested for continuity using a digital multimeter.

After the connections are checked and, if necessary, repaired, the backing is carefully inverted with PZT face down and placed inside the mold. A faint trace of tungsten is mixed with epoxy to keep the color of the sensor consistent and hide all the interior wiring. The mixture is poured and allowed to cure for 24 hours. The final product is removed from the mold and is now ready to be interfaced to the pulser circuit.

Revised transducer fabrication

Essentially the same methods from the process just described were used to make an improved sensor, but with the following differences:

- Connections from the element to the terminals are made with solder iron rather than silver filled epoxy.
- The piezoelement is embedded in the backing so that only the front (hot) face is exposed.
- The piezo is grounded on one side with a conductive foil that spans the length so that all elements are effectively grounded after full thickness cutting.

Soldering was found to provide a more reliable connection as the silver filled epoxy had a tendency to crack due to its brittle nature. Embedding the piezo provided a much stronger base for cutting the elements and also allowed for full penetration cuts, reducing the acoustic crosstalk. Apart from these modifications, all other aspects, including the backing properties and molds remain the same.

4.4.3 Software

The software used to provide a user interface to the hardware was developed in MS Visual C++ environment. Essentially, the program maps a specified channel and delay to the associated i/o pin of the corresponding multiplexer in the delay banks. A fragment of the source code showing the key functions is given below.

```
int  dly_table[12]={500, 1000, 2000, 100, 200, 400,
                    20,   40,   80,   5,  10, 20};
int  pin_table[SIZE]={16, 17, 18, 19, 20, 21,
                      22, 23,  8,  9, 10, 11};    /* CH 1*/

/*****************************************
 * FUNCTION exec_dly(int delay_settings[16]) *
 * ------------------------------------   *
```

```
* Executes delay settings for 16 channels.  *
*********************************************/
void exec_dly (int dly_settings[16])
{
  int i, j, k, elem;

  for (elem=0; elem<16; elem++) {
    k=12*elem;
    for (i=k, j=0; i<k+12, j<12; i++, j++) {
      if ((dly_settings[elem]/dly_table[j]==1) || ...
      (dly_settings[elem]/dly_table[j]==3)) {
      cbDBitOut(0, FIRSTPORTA, pin_table[i], 1);
      dly_settings[elem]-=dly_table[j];
      }
    }
  }
}
```

The function shown takes a one dimensional array with 16 elements which correspond to the delay requested by the user for each of the 16 channels. From this it is able to find the required pins from the pin-out lookup table array and activate them logically high through the use of the CbDBitOut( ), which is provided by the Cyber 192-bit i/o board library function. This i/o is transferred through parallel port to the circuit via color coded flat ribbon multiconductor cable. The i/o fans out to the corresponding pin on the circuit.

The algorithm for determining the required delays is very simple and efficient. While the outer loop runs through all 16 channels, each one will be swept along its possible delay values which are indexed according to the delay lookup table array. If the integer quotient resulting from the actual delay divided by the current index delay is 1 or 3, then it is a valid delay and the high-bit output is true. The delay settings for the particular channel will be decremented by the current index and the procedure continues until all 12 possible delays are scanned for each channel. Thus, the cascading operation is encapsulated in this code fragment by summing up the individual delays from each bank to achieve the desired delay.

Calibrating the delays is also done through the software. Essentially this is an iterative procedure whereby the programmed delays are measured against the actual delays which are obtained from a LeCroy digital oscilloscope. Two probes are used: one as a reference (channel 1), and the second to measure the actual delay for all other channels. These two signals are displayed on the oscilloscope and their separation in time can be obtained through an automatic delay function. If the difference between measured and expected delays is greater than an agreed tolerance (5 ns), then they are adjusted accordingly. Once convergence occurs for all 16 channels, these new delay settings are stored for future reference.

Chapter 5

Experimental Results

This chapter describes the experimental setup used for system-wide calibration and the resulting directivity curves obtained for various steering angles and parameter settings. The calibration assembly is used for observing changes in the transducer response due to several important phased array parameters, including interelement spacing d and number of elements N. Before conducting a full-fledged study, preliminary tests were made using a first-cut trial phased array. Analysis of both single and multiple element responses resulted in an improved transducer design. The experimental directivities are compared with a numerical simulation based on the theory discussed in chapter 3.

5.1 Experimental Program

5.1.1 Related Studies

Various experimental techniques for calibration of phased array sensors have been studied by several authors. One of the earliest experimental methods for measuring the sound field produced by phased arrays designed for NDT was developed by Lemon and Posakony (1980). They fabricated a 240-element phased array whose radiation pattern was created by positioning the sensor at the center of rotation of a rotating arm in a water tank. The transmitted energy was detected by a small hydrophone located at the end of the arm. The received signal was gated and peak detected, and the voltages corresponding to the peak received amplitudes were used to drive the x and y axes of a chart recorder to obtain the resulting directivity plot.

McNab and Stumf (1986) carried out an experimental assessment of the radiation field of an 8-element monolithic array. In their scheme, the transducer was positioned on the center of a cylindrical steel test block, measuring 40 mm in thickness and 92 mm in radius. A detector probe was secured to the curved surface of the block using radial elastic straps. An even flow of couplant was issued between the sensor and the block, facilitating uniform pressure at the desired angular location.

Mo *et al.* (1992) performed a quantitative assessment of crosstalk in various PVDF transducers. The angular response of the 9-element array is mounted on a test fixture immersed in a water tank. A 5 MHz source transducer was attached to a length-adjustable arm that was moved along an arc to obtain various angle positions. The far-field response of the array was recorded from -30° to +30° in 2.5° spacings.

5.1.2 General Design Objectives and Considerations

The realization of several key objectives has led to a reliable and useful calibrating system which shows significant improvement over the ones cited above. Accordingly, the following features were considered to be extremely important in order to accurately assess the performance of the phased array:

- A non-contact immersion transducer was to be used for reception of transmitted ultrasound.
- Complete automation of the calibration process.
- Directivity plots should be obtained in the far-field from $-90°$ to $90°$.
- Provision of secure and stable housing of the phased array during testing.

A machined disk having a smooth rim (i.e., a "wheel") was used for assessing accurate directivity of the transmitted ultrasound. Direct coupling to the material using contact transducers can often produce anomolous return signals. A more reliable approach is to partially submerge the rim of the wheel in water and use an immersion transducer which is focused on the rim. In this manner, the signal acquired is stable and provides a correct measurement of the ultrasonic energy along the circumference. Automation of signal acquisition for varying locations along the circumference is enabled through a step motor coupled to the center of the wheel.

Since steering is most effective in the far field, the near field length of the transducer will dictate the required radius, and consequently, the size of the calibration wheel. Ideally, the disk should be thick enough to avoid excessive sidewall reflections due to beam spreading. Wooh and Shi (1997) show that the near field is drawn closer to the face of the transducer as the steering angle is increased, so that the maximum near field length occurs at zero degrees. In this regard, the radius may be computed based on the well-known near field formula

$$N_f = \frac{D^2}{4\lambda} \tag{5.1}$$

where N_f is the near field length, D is the length of the array in the azimuthal direction and λ is the wavelength in the material.

Since the near field grows with the square of D, a compromise must be made between having an excessively large radius and being able to accommodate phased arrays having different D values,[1] A reasonable value of $D = 1.5$ in. (3.81 cm) was selected based on the transducer design discussed in the previous chapter. For a transducer operating at 5 MHz in aluminum (rationale for material selection provided below), the required radius is 11.3 in. (28.7 cm). The radius of the wheel in this design was rounded up to 12 in. (30.48 cm).

The selected acoustic medium is another vital consideration. For typical NDE applications, steel is the logical choice. However, its practical limitations such as cost, weight and machinability do not make it the ideal candidate. Aluminum, on the other hand, is comparatively cheaper and almost three times lighter than steel

---

[1] D is determined by the number of elements, N, interelement spacing, d and element width, a *viz.* $D = d(N - 1) + a$.

for the same volume of material. The savings in weight not only makes the assembly simpler to construct, but also reduces the required torque and cost of the step motor. Since compressional wavespeeds between the two materials are approximately equal ($c_{\text{steel}} = 5920$ m/s; $c_{\text{alum.}} = 6320$ m/s), the corresponding steering angles will be almost the same. Finally, aluminum enjoys similar properties as steel (e.g., isotropy and homogeneity), making it is an excellent alternative as the choice material used in obtaining the directivity of the phased array.

5.1.3 Calibration Concept

The concept behind the system calibration is illustrated in Fig. 5.1. The phased array is positioned so that the beam is transmitted from the center of the disk. The profile of the beam is traced using an immersible receiving transducer which is focused at the rim of the calibration disk. As the disk rotates via step motor, the receiving transducer picks up the energy of the transmitted beam at the rim. For a particular steering angle θ_s, one will observe a marked increase in maximum energy until θ_s is reached, followed by a decrease, tracing the profile of the main lobe. There may also be some side and grating lobes depending on the sensitivity of the setup and the interelement spacing chosen between the array elements. The result is a directivity plot which can be used to assess the performance of the sensor in a controlled environment in terms of its steerability (how close the peak energy is to θ_s) and its directivity (how narrow the main lobe is). The experimental data is also used to verify and confirm the theoretical model developed in Chapter 3.

As shown in Fig. 5.1, four distinct scenarios can be anticipated: (1) a well directed beam aimed at the intended steering angle, (2) a well directed beam not located at the correct steering angle, (3) correct steering angle but broad directivity and (4) poor directivity and poor steerability. Case 1 is the optimum performance that is to be strived for: it represents good delay control for correct steering, as well as a properly fabricated and designed sensor. The second scenario may indicate that the delay circuit is producing large errors which have a tendency to shift the steering angle. In the third case, the circuitry is probably calibrated well but the sensor requires some better design. Finally, the fourth case requires both improved sensor design as well as a calibration scheme to handle the inevitable delay errors caused by the delay chips and multiplexers.

5.1.4 Experimental Setup

The actual setup, shown in fig. 5.2 includes the following components:

- Aluminum calibration wheel
- Spherical focus immersion transducer
- Step motor (including controller and driver) and gearbox
- Plexiglas water tank

The setup consists of a 2 ft (61 cm) diameter, 1.5 in. (3.81 cm) thick aluminum disk which is free to rotate about its center. The aluminum required special machining in order to ensure perfectly smooth, flat and round surfaces. Irregular or rough surfaces would defeat the purpose of the experiment since the ultrasound detected at the receiver would give a totally false indication of directivity due to scattering and diffraction at the interface.

A 2 in.^{2} (12.9 cm^2), 1 in. (2.54 cm) deep pocket cut out above the horizontal centerline of the disk is used to house the phased array unit. A spring-loaded plate is inserted in the pocket to stabilize the sensor and to maintain good coupling contact with the aluminum surface. The bottom half of the disk is placed inside a plexiglas water tank, with the water level set slightly above the rim. A 2.25 MHz focused receiving transducer is situated 2 in. (5.08 cm) directly beneath the vertical centerline of the disk, as indicated in Fig. 5.2. Rotation of the disk is controlled by a step motor having a static torque of 100 oz-in. and maximum angular resolution of 0.014°. A 100:1 gearbox was placed between the motor output shaft and coupling shaft to the wheel in order to increase the torque and reduce the inertial mismatch between the motor and the wheel. The motor parameters were set in its native programming language to turn the wheel every 0.5°.

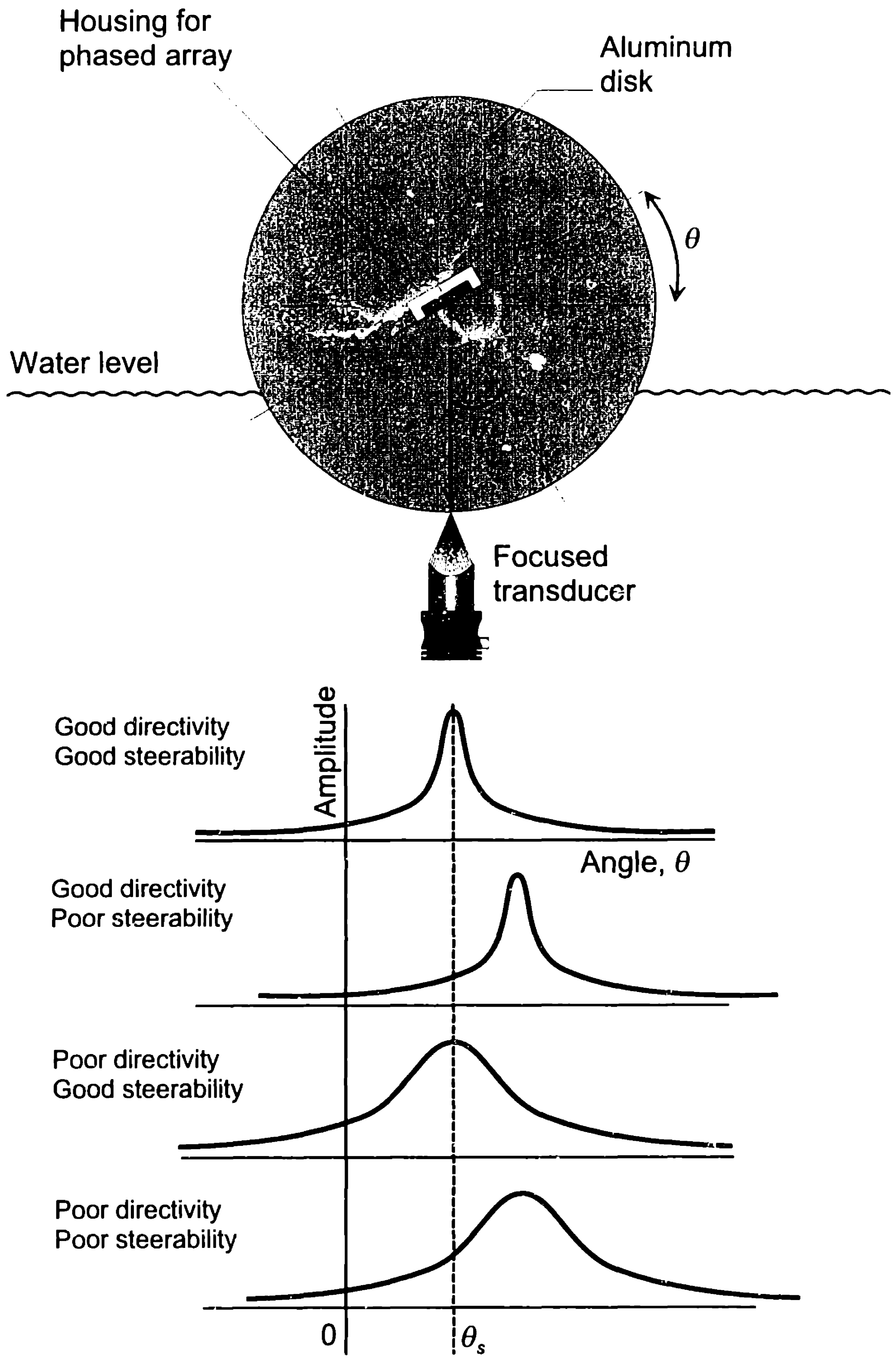

Figure 5.1: Concept of sensor calibration in assessing transducer performance and validity of the theoretical model.

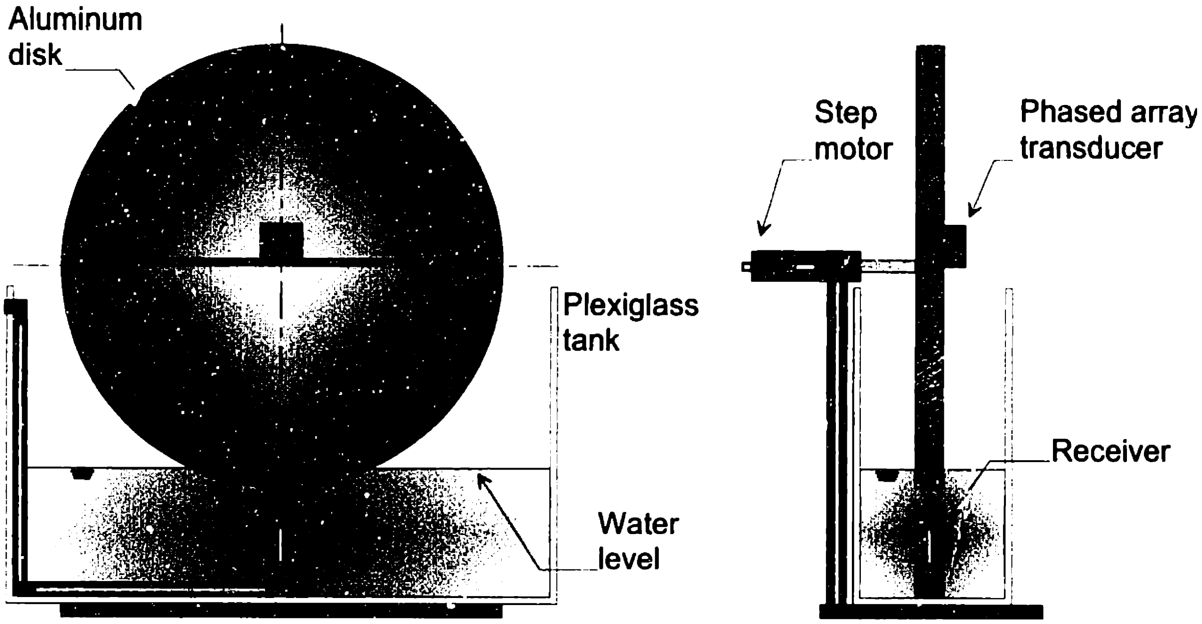

Figure 5.2: Experimental setup for calibrating the phased array sensor.

The overall system connectivity is shown in Fig. 5.3. This figure shows the integration of the system developed (as described in the previous chapter) and the calibration assembly. A PC is continuously controlling three devices: step motor controller through RS-232 serial port, a Tektronix TDS-210 1 GHz digital oscilloscope through GPIB, and the delay circuit through a 192-bit Cyber Research model 192-DIOi/o board.

5.1.5 Principle of Operation

Figure 5.4 shows the actual operation of the calibration experiment. First, the phased array is initially set at 0° steering angle in order to locate the first received signal on the oscilloscope.[2] The sensor is programmed for a particular steering angle, θ_s, through the 16-channel delay-generation software. The disk is then rotated to its start position at -90°. After each rotational step increment from the motor, the oscilloscope is triggered to acquire the received waveform which can be later processed. Hence, for

---

[2] The time-of-flight for the ultrasonic beam to travel the 12 in. radius of the aluminum wheel plus two inches in water is 86 μs.

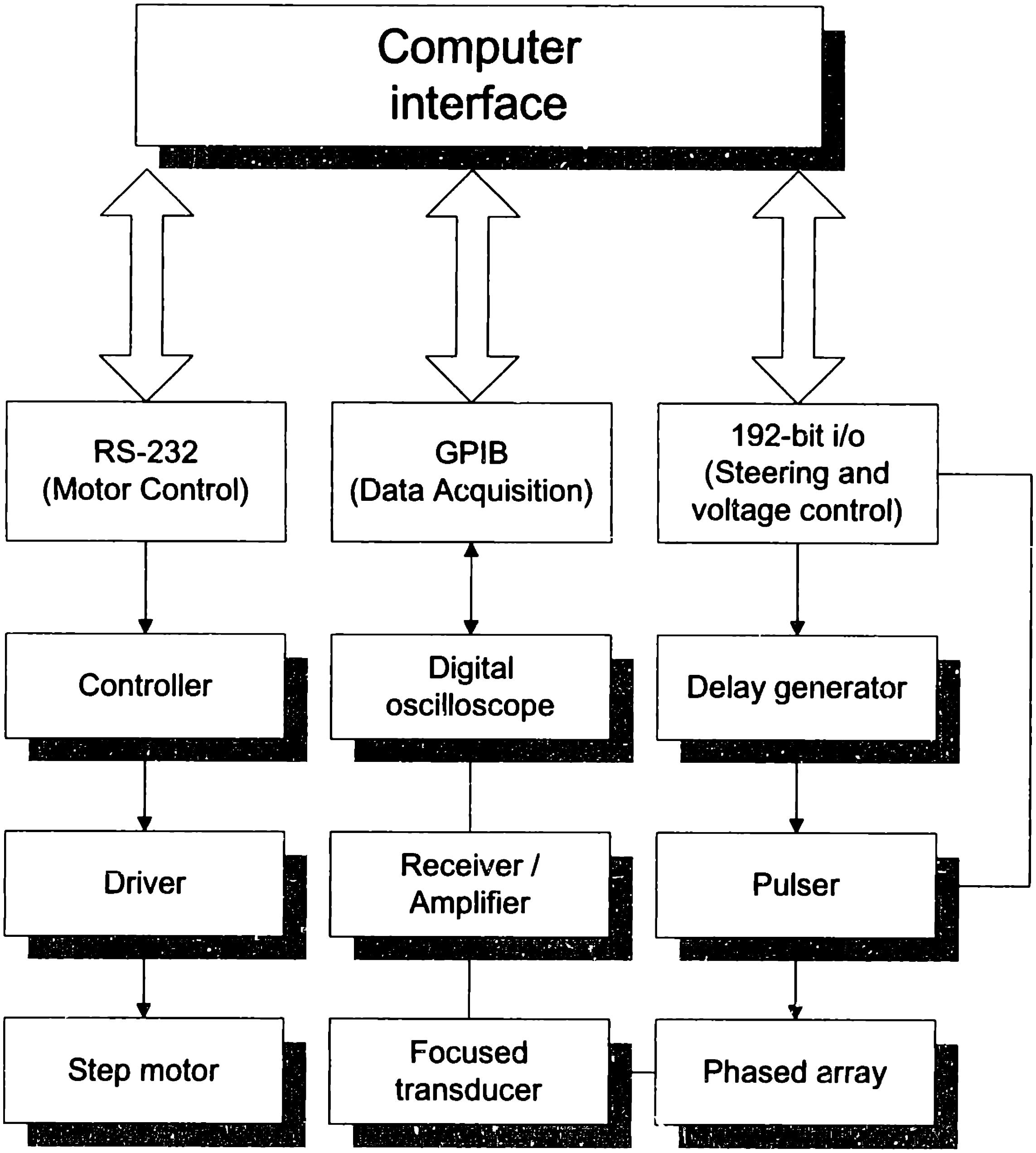

Figure 5.3: Schematic diagram of control flow of the calibration setup.

a particular angle increment $\Delta\theta$, and waveform $A(t)$, an array of waveforms is stored in memory as a single binary file which can later be decompressed into $180/\Delta\theta+1$ ASCII files. Each ASCII file is stored in a two-column format; the left column provides time (based on the sampling rate) and the right column gives the corresponding voltage. These ASCII files represent the A-scans which are used for actual data processing and can be later deleted; the single binary file encapsulates all the necessary information for future use.

There are several methods for determining the maximum pressure at a particular angle. The method adopted in this work is to gate the received waveform and acquire the maximum peak-to-peak voltage:

$$\bar{A} = (A_i)_{\mathtt{max}} - (A_i)_{\mathtt{min}}, \tag{5.2}$$

where $(A_i)_{\mathtt{max}}$ and $(A_i)_{\mathtt{min}}$ are the maximum and minimum acquired voltages within the specified gate, respectively. The peak-to-peak amplitude is a convenient way to measure pressure but care should be taken when excessive noise enters the system. Other methods, such as an average intensity, may be more representative in this case.

5.2 Preliminary Results

5.2.1 Sensor Description

The first cut phased array was assembled according to the method described in Chapter 4. The active element used was 0.04 in (1.02 cm) thick resulting in an expected center frequency of 2.25 MHz. The grooves between elements were filled with a silicone rubber adhesive sealant (GE Translucent RTV 118) for support and protection. A layer of the same material was spread over the array to electrically isolate and shield the conductive lines painted on each element. One final piece of Kapton tape was firmly secured to the bottom face of the entire sensor. Connections from the transducer to the pulser circuit were made using a 4 ft (122 cm) multiconductor cable with overall shielding.

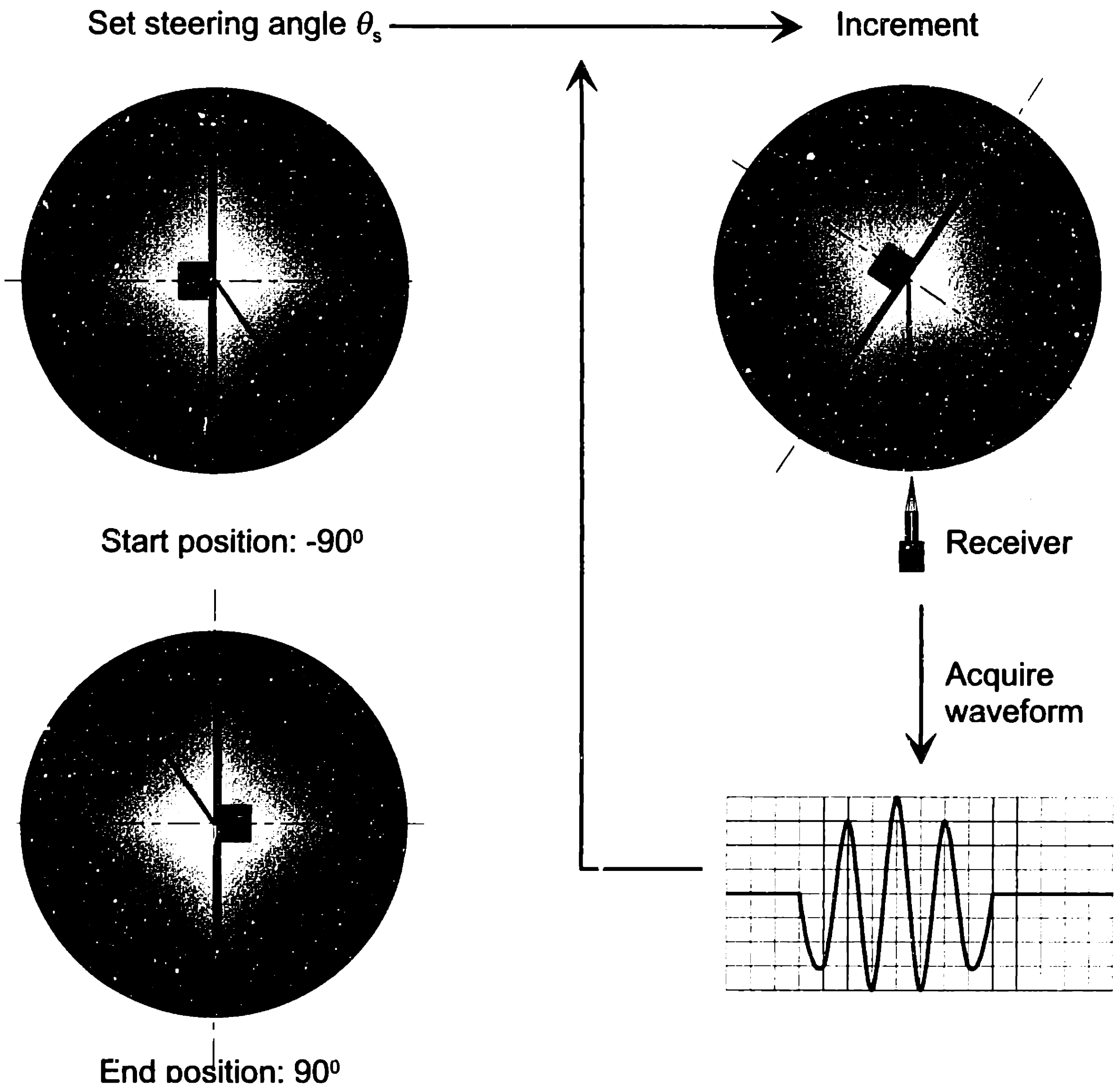

Figure 5.4: Motor control and data acquisition routine.

5.2.2 Single-element Response

Figure 5.5(a) shows the single element directivity taken from the eighth element of the array with both the RTV and Kapton tape on the front face. Ideally, the individual elements of the phased array should exhibit virtually no directionality, similar to a point source. The ideal situation, shown in Fig. 5.6(a), models a single element. It is clear that the experimental results show a strong directivity at approximately 10°.

One explanation for this is that the elements are experiencing crosstalk. When the eight element is fired, the acoustic energy is transferred to neighboring elements. To prevent this, the elements should be in perfect isolation. This concept was proven both experimentally and numerically as shown in Fig. 5.5(a) and fig. 5.6(b). Figure 5.5(b) shows the directivity of a single element mounted on a backing. Since it is in isolation, its directivity is much broader compared to that of Fig. 5.5(a).

However, the directivity of this single isolated element still does not match the ideal point-source model given in Fig. 5.6(a). The model was adjusted by implementing the concept of "effective element width". That is, the element acts as though its width is equivalent to a larger width which predicts the behavior nicely as shown in Fig. 5.6(b). It should also be noted that only Kapton tape (and no RTV) was used in this case. Because the response is much more symmetric it appears that the RTV may have had other deleterious effects on the response of the elements.

5.2.3 Multi-element Response

Figure 5.7 shows the directivity plots obtained for the following steering angles: 0°, 13° and 43°. Figure 5.7 (a) does not show any clear steering or directivity when the beam is steered at zero degrees. Not only is the peak amplitude shifted to $\approx -15°$, but there are also two spurious side lobes which exceed 0.6 normalized amplitude. The directivity at 13°, as shown in Fig. 5.7 (b) is improved. For larger steering angles, such as $\theta_s = 27°$, shown in Fig. 5.8 (b) and $\theta_s = 43°$, shown in Fig. 5.7 (c), two side lobes located to the left of the main lobe start to appear. Not only do they become

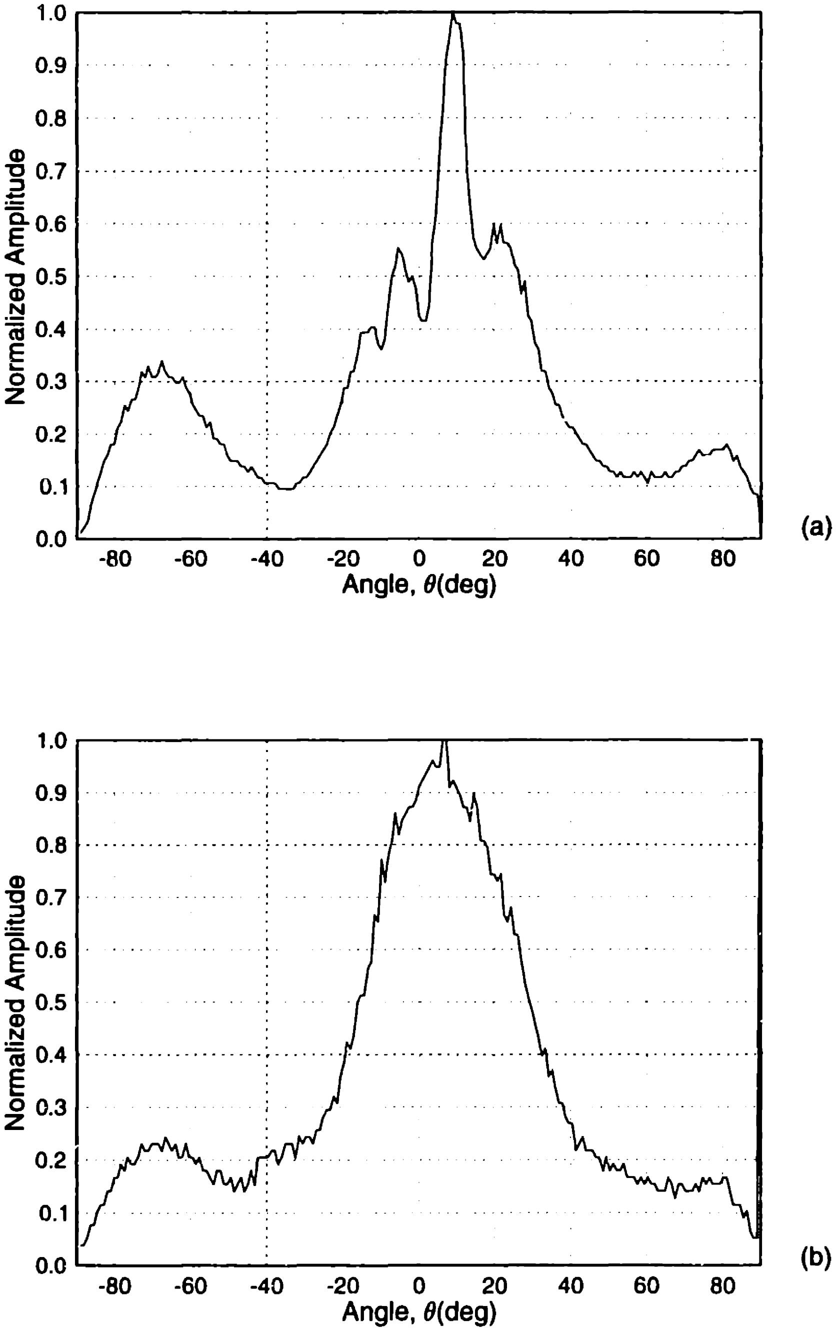

Figure 5.5: Actual response of single element: (a) RTV and Kapton front layers and (b) Front layer with Kapton tape and RTV removed.

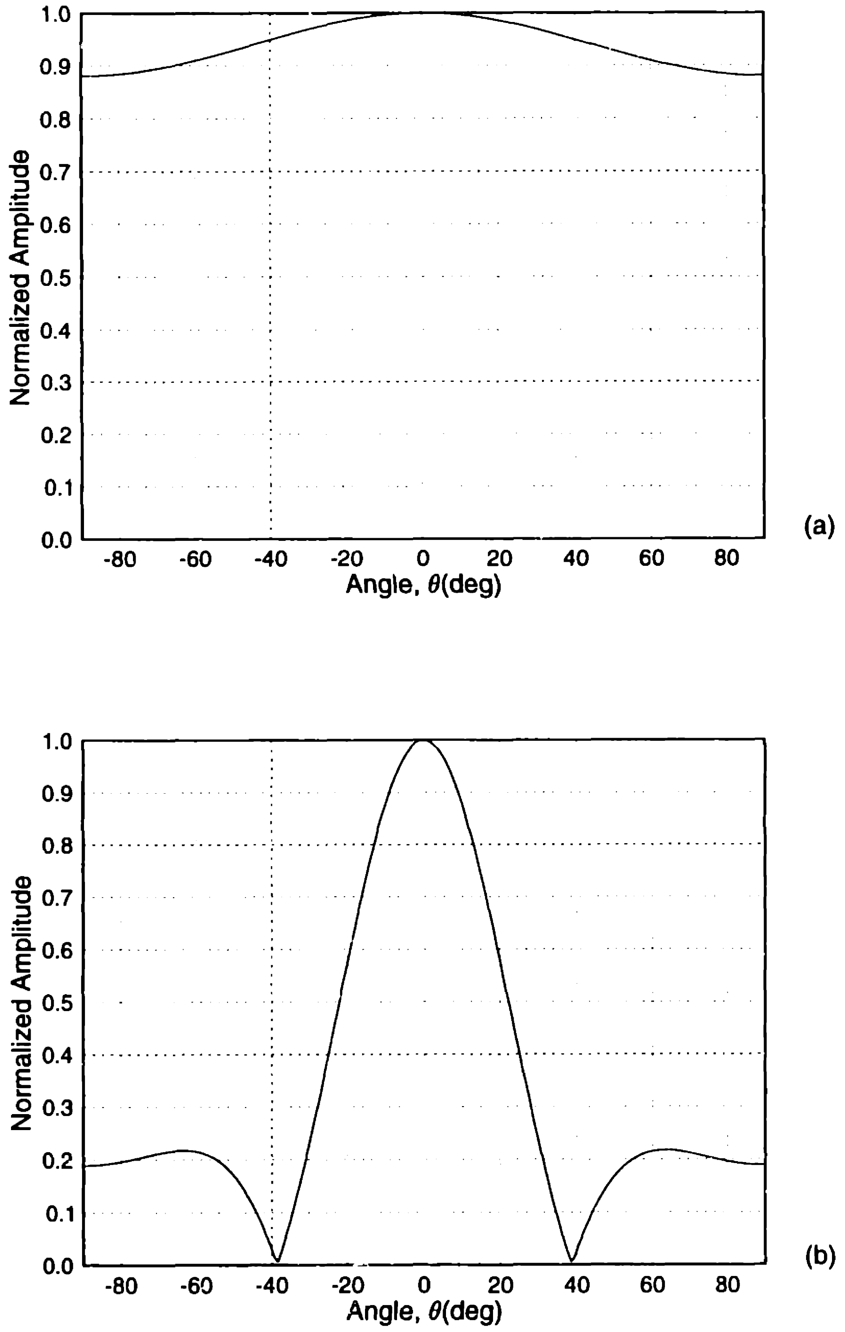

Figure 5.6: Predicted single element directivity assuming: (a) ideal point source and (b) effective element width concept to take crosstalk effects into account.

more pronounced for the 43° curve, but the beam can no longer be steered beyond $\approx 35^\circ$ with this particular setup.

Crosstalk effects and delay errors were assumed to be the primary contributors to both the large side lobes and the deviation from the intended steering angle. Figure 5.8 (a) shows the theoretical directivity at 27°, followed by the actual results, and then corrected for acoustical crosstalk and delay errors. The crosstalk was modeled using the concept of the effective element width as discussed earlier. Delay errors were measured from the oscilloscope and directly inputed into the model as the actual time delays between elements. Figs 5.8(b) and 5.8(c) confirms that the combination of delay errors and crosstalk are possible causes of distortion in the beam directivity and steerability.

5.2.4 Discussion

The results of the first cut array clearly show the need for an improved design and fabrication methodology. However, the utility of the calibration wheel is fully demonstrated. It clearly shows that both delay errors and sensor design are key issues which should be explored in greater detail. The adjustment of delay errors through an iterative program is described in Chapter 4 since it is an actual component of the system development. The crosstalk effects can be resolved by using the second sensor fabrication methodology which completely embeds and isolates the elements in the backing. It was also found that electrical shielding was another serious problem in the initial design. The multiconductor cable requires individual shielding of the wires so that elements may not transfer signals through EMI.

In summary, the findings from the first cut study lead to the following suggested improvements:

- Reduce delay errors through a calibration scheme.
- Isolate individual elements completely through an embedded technique.
- Prevent accidental shorting of elements with improved grounding technique.

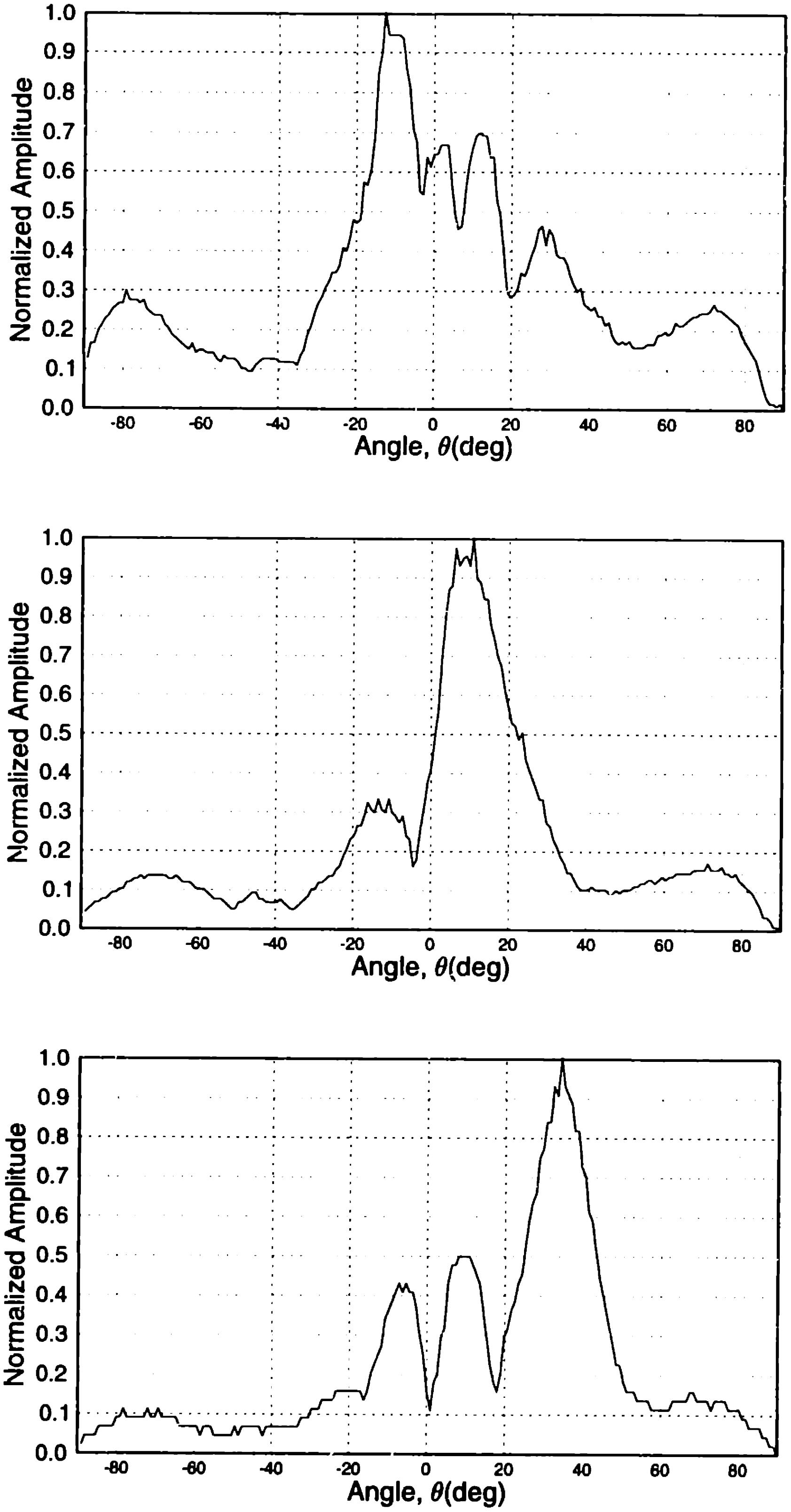

Figure 5.7: Experimental directivity plots: (a) $\theta_s = 0°$, (b) $\theta_s = 13°$ and (c) $\theta_s = 43°$.

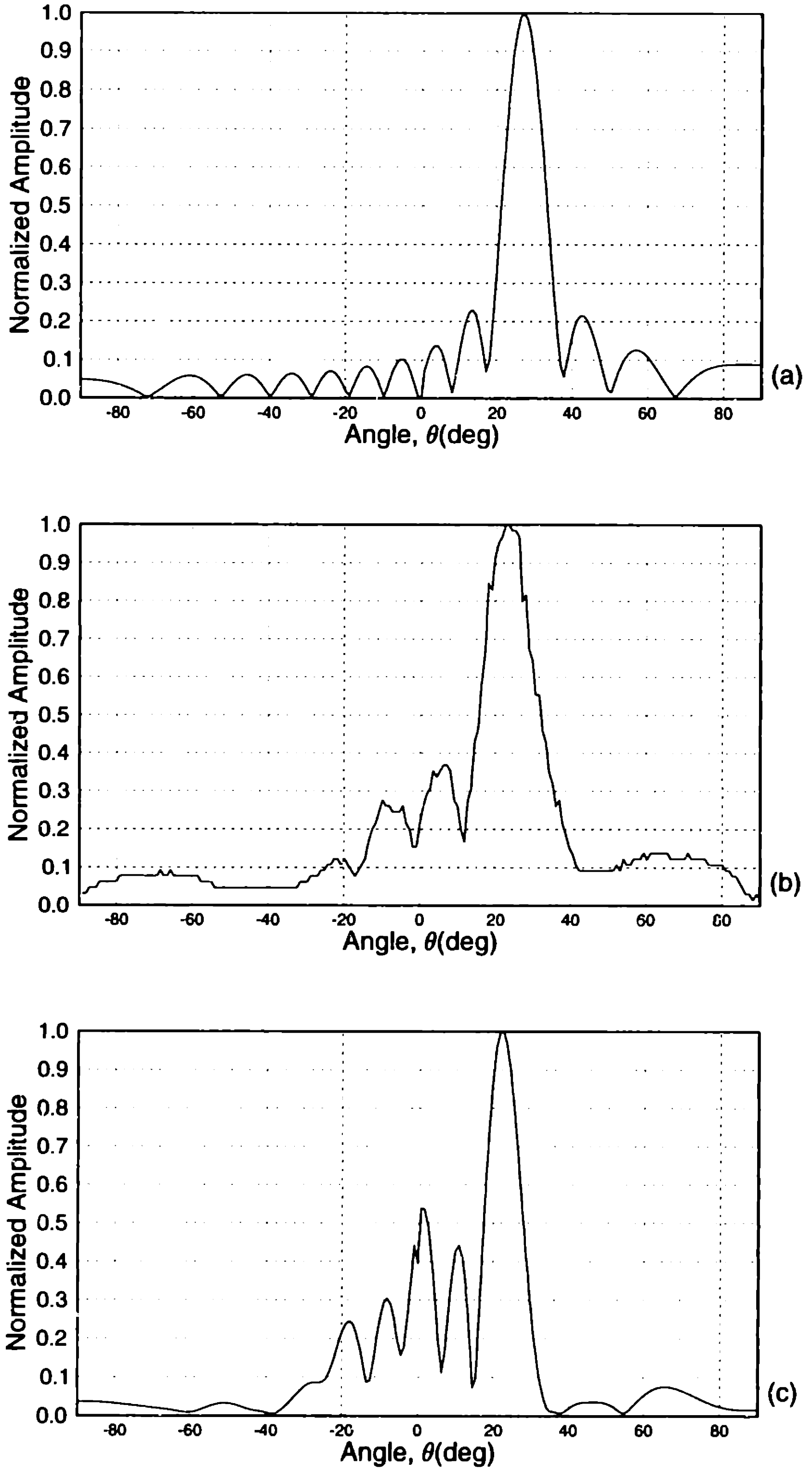

Figure 5.8: Modeling the crosstalk and delay errors for $\theta_s = 27°$: (a) simulated directivity without effects, (b) actual directivity and (c) simulated directivity accounting for the effects.

- Minimize electrical crosstalk by using individually shielded cable for each channel.
- Avoid the use of any front matching layer (such as RTV) whose thickness cannot be precisely controlled.

5.3 Improved Results

The results from the previous section led to an improved transducer design along with some other important modifications. A description of the revised transducer design can be found in Chapter 4. We will begin this section by discussing how the parameters for this study were selected, followed by a single element directivity. The simulation used to predict the phased array steering profile will be briefly summarized and a sample input parameter file will be included. The method of processing the raw data to create a directivity is also described. Finally, the resulting simulated and obtained directivities will be presented, along with a summary and discussion of these results.

5.3.1 Single-element Characterization

Prior to testing the steering behavior of this transducer, several single element experiments were performed. First, the A-scan from a single element was acquired and the frequency from its Fourier transformation was determined. This result is critical in order to have an accurate estimate of the wavelength λ in the material. Secondly, the directivity from the same element was obtained and several important observations were made.

The as-obtained time-domain waveform for a single element is plotted below in Fig. 5.9(a). along with its magnitude spectrum in Fig. 5.9(b). Analysis of the time domain signal $x(t)$ in the frequency domain $X(\omega)$ is achieved through the use of the magnitude Fourier Transform:

$$X(\omega) = \left| \int_{-\infty}^{\infty} x(t)e^{-j\omega t}dt \right|. \tag{5.3}$$

The frequency spectrum is computed for the waveform from 0 to $\approx$ 3.5 μsec since the trailing signal of lower frequency would result in an interfered spectrum. From Fig. 5.9(b), it can be seen that the signal has a center frequency of 1.8 MHz, resulting in a wavelength λ of 3.5 mm in aluminum. Note that the spectrum is somewhat narrowband. This is probably due to the relatively low backing impedance and wide pulse width.

The piezoceramic (PZT-5A) used as the active element in these transducers is designed to resonate at a frequency of 2.25 MHz. However, because of the backing, pulse, protective Kapton tape layer, and medium, the frequency will inevitably shift. This shift can be predicted with some degree of accuracy in advance with a Mason or KLM model (Silk, 1984). However, such models are not employed in this work; the frequency was determined through several trial transducers experimentally.

A single element directivity representative of the sensors with embedded design is given in Fig. 5.10. The optimum directivity with the cosine effect (to be discussed shortly) taken into account, is shown in Fig. 5.10(a). The actual directivity is shown in Fig. 5.10(b). A more realistic approach may be to re-introduce the effective element width, as shown in Fig. 5.10(c). This directivity was modeled assuming an effective width of $a = 3d$. It appears that individual elements are still somewhat directed due to the contribution of acoustic crosstalk from neighboring elements. However, since the true effective width cannot be justified without further study, the actual element width will be used from here onward, which assumes there is no adjacent crosstalk.

5.3.2 Data Collection and Processing

Each experimental directivity plot is essentially composed of 361 points. Each point is obtained from the maximum peak-to-peak amplitude of the gated waveform acquired at every 0.5°, from -90° to 90°. Several representative waveforms are shown in

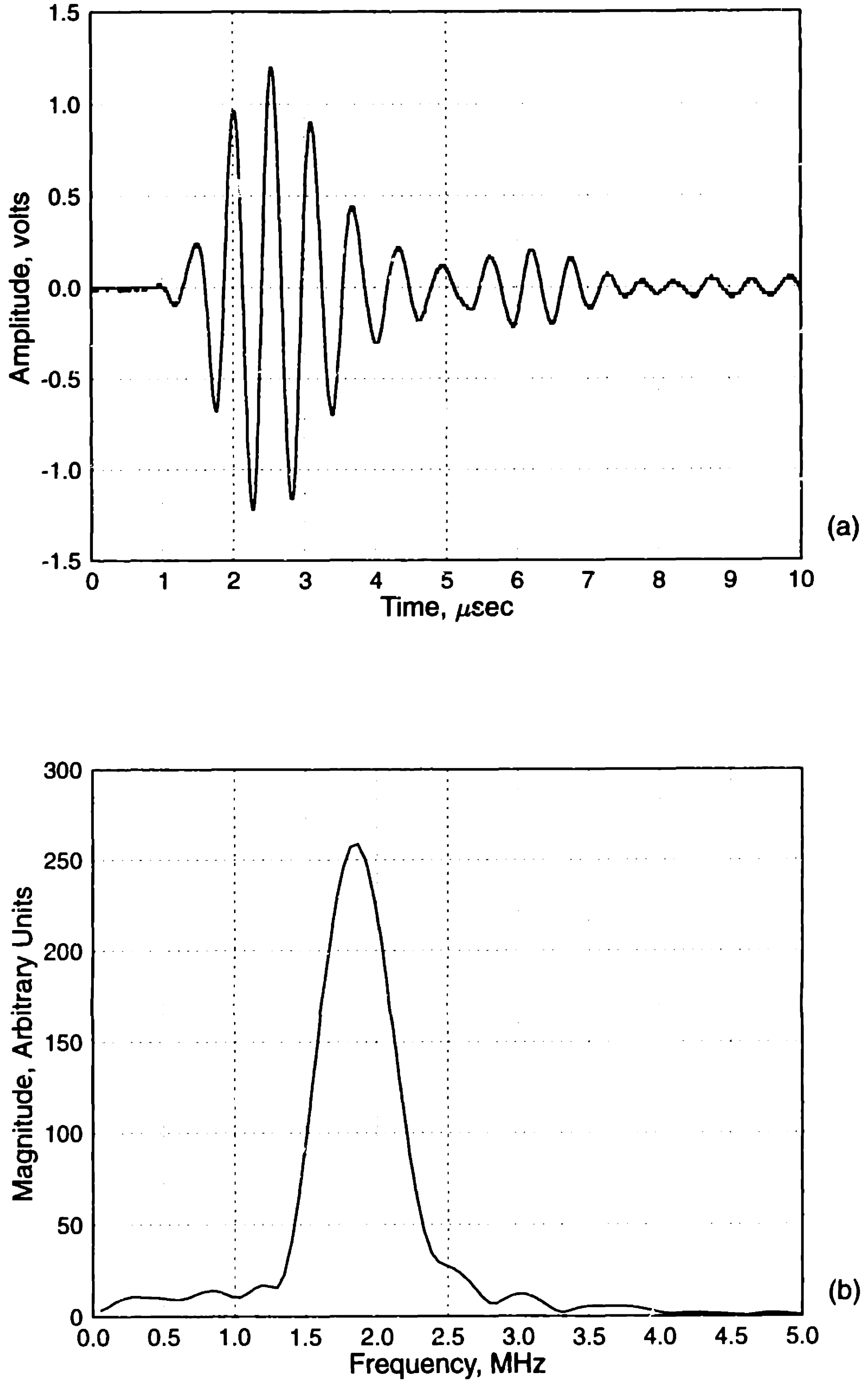

Figure 5.9: Single element response: (a) time domain and (b) frequency domain.

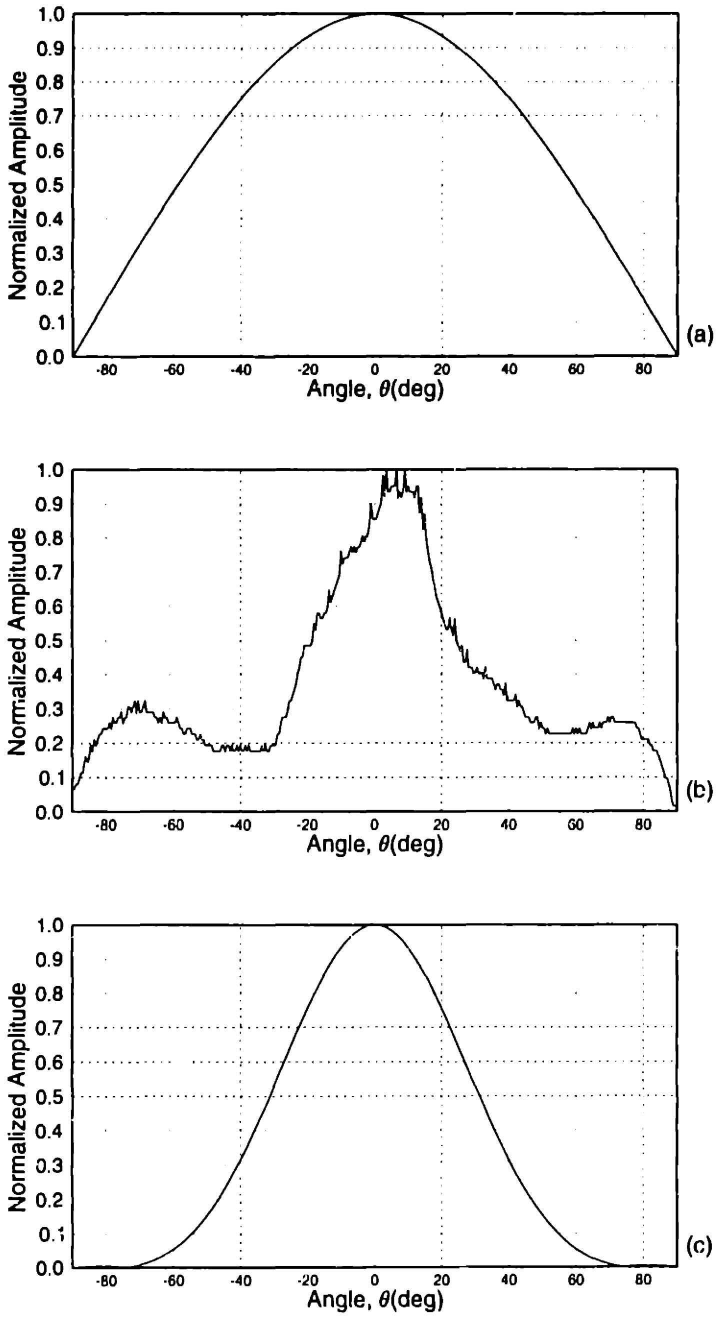

Figure 5.10: Single element directivity pattern: (a) simulated optimum directivity with cosine envelope, (b) actual directivity for single element and (c) modified using an effective element width ($a = 3d$).

Fig. 5.11. In this example the steering angle is set to 27°. The A-scans correspond to the positions $\theta = -11°$, $\theta = 18.5°$ and $\theta = 27.5°$ along the wheel were acquired for the directivity shown in Fig. 5.25(b). The receiver gain on the pulser/receiver unit was set so as not to saturate the signal, otherwise the shape of the directivities would be distorted and the result would be meaningless. Note that the waveforms are clipped at the right since this is where the right gate was set. The waveforms are clearly increasing in amplitude until the maximum is reached at $\theta = 27.5°$, which is in agreement with the steering angle. These waveforms also show some drift in the time axis which sometimes results in extra information entering the gate. This can easily explain some of the larger lobes present in several directivity plots, as will be discussed later.

5.3.3 Numerical Simulation

The computer model used in this thesis was developed by Lawrence Azar [3] and can be used to obtain directivities and images of the ultrasonic field for focusing and steering in both the near and far fields. The mechanics behind this simulation are based on the theory developed in Chapter 3. Each element is represented as a point source and the contribution of the propagating fields from each element is synthesized via Huyghen's principle to produce the total wavefront. However, there is one important difference taken into account in the simulation: the element directivity is modified by a cosine envelope. This effect was first observed by Selfridge *et al.* (1980) and provides a more realistic directivity.

A sample input parameter file showing the settings programmed for the simulated directivity shown in Fig. 5.14 is given below. Only the relevant parameters will be discussed in this example (lines 2–6). For this simulation, 8 elements will be activated, so `Number_Elements` (line 2) is set to 8. For aluminum, we will set `WaveSpeed_m/s` equal to 6320 m/s. The center frequency, as obtained from the Fourier spectrum of Fig 5.9, is inputed into line 4 in Hz. The steering angle, line 5, is in degrees

---

[3] For additional information regarding the software, contact `azar1@ix.netcom.com`

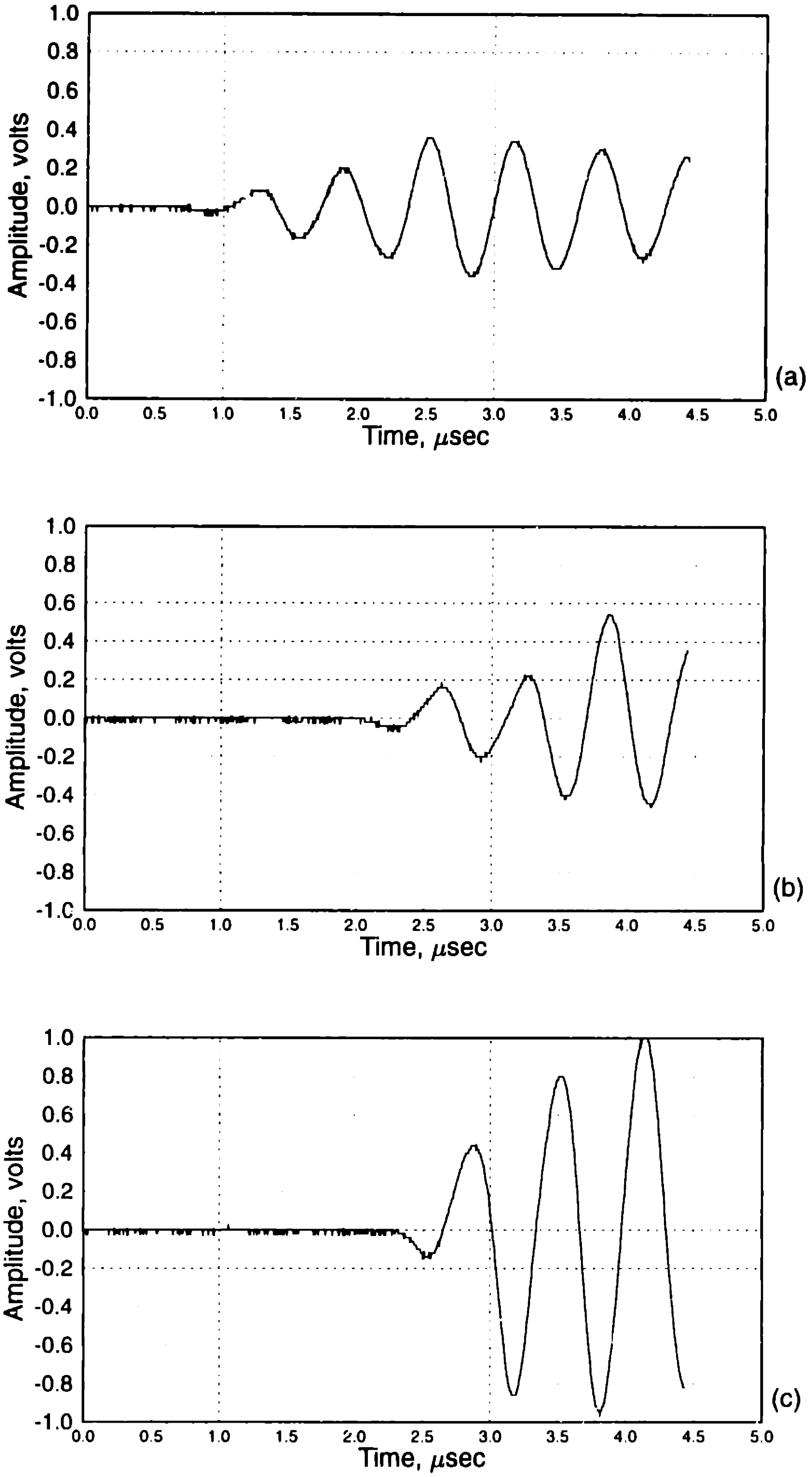

Figure 5.11: Waveform obtained during directivity experiment: (a) $\theta = -11°$, (b) $\theta = 18.5°$ and (c) $\theta = 27.5°$.

and written in the **Angle_degrees** field. Finally, the value for d/λ is entered in the **Ratio_d/Lambda** input field, line 6. The remaining lines are global settings; the definition of these parameter fields can be found in the Pilarry documentation.

```
Quality
512
Number_Elements
8
WaveSpeed_m/s
6320
Frequency_Hz
1800000
Angle_degrees
0
Ratio_d/Lambda
.40
Focus_1_or_Steer_2
2
Image_1_Directivity_2_Enter_3_Wave_4_Line_5
2
Ratio_a/d
.5
Odd_Points_that_make_up_a
1
Focal_Length_(meters)
.3
Directivity_Distance_(meters)
.3
Attenuation_Coefficient_(dB_per_meter)
0
number_of_decimal_places_for_time_delay(9_is_for_ns)
9
ratio_L/lambda
1
points_along_L
1
width_of_image
.3
X_min
-.1
```

5.3.4 Directivity Plots

This section provides the results of the experimental and simulated parameter study. The geometric parameters d and N were configured according to Fig. 5.12 for the sensor having a center-to-center spacing of $d = 0.055$ in. The second sensor had interelement spacing of $d = 0.080$ in and the arrangement of parameters is shown in Fig. 5.13. These configurations allowed for various parameter studies. For example, in both cases, all elements may be fired at the given spacing. If every other element is used, then we may explore the effect of $2d$ for the same transducer. Obviously, this can only be done for half the elements. At the same time, we may hold the spacing constant and see the effect of half the number of elements if the middle group of consecutive elements are activated and the outer elements are disconnected from their respective pulsers. This results in several combinations of N and d whose effects we can monitor in a controlled fashion while changing the steering angle. In this study, θ_s was set for three angles: 0°, 13°, and 27°.

For reference, the directivities may be grouped according to the same parameter settings for d and N as follows (element width a and elevation dimension L also included but not studied):

- Figs. 5.14–5.16: $N = 8$, $d = 0.4\lambda$, $a = 0.20$ in. (.51 mm), $L = 0.5$ in. (1.27 cm)
- Figs. 5.17–5.19: $N = 15$, $d = 0.4\lambda$, $a = 0.20$ in. (.51 mm), $L = 0.5$ in. (1.27 cm)
- Figs. 5.20–5.22: $N = 8$, $d = 0.8\lambda$, $a = 0.20$ in. (.51 mm), $L = 0.5$ in. (1.27 cm)
- Figs. 5.23–5.25: $N = 16$, $d = 0.6\lambda$, $a = 0.25$ in. (.635 mm), $L = 0.5$ in. (1.27 cm)
- Fig.5.26: $N = 8$, $d = 1.2\lambda$, $a = 0.25$ in. (.635 mm), $L = 0.5$ in. (1.27 cm)
- Fig.5.27: $N = 8$, $d = 0.6\lambda$, $a = 0.25$ in. (.635 mm), $L = 0.5$ in. (1.27 cm)

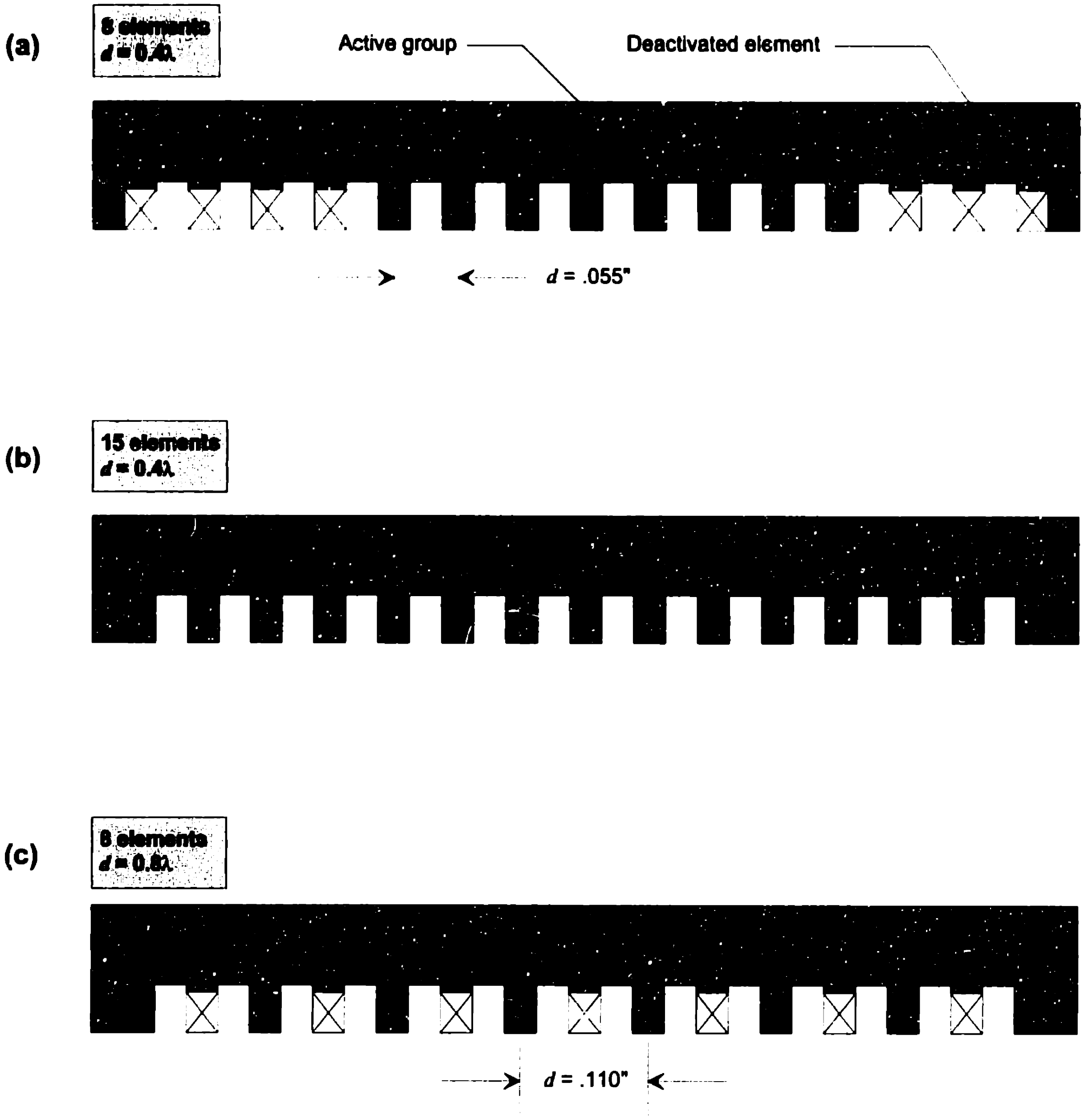

Figure 5.12: Transducer testing configurations for various parameter settings; 15 element sensor with elements spaced at 0.055 in.

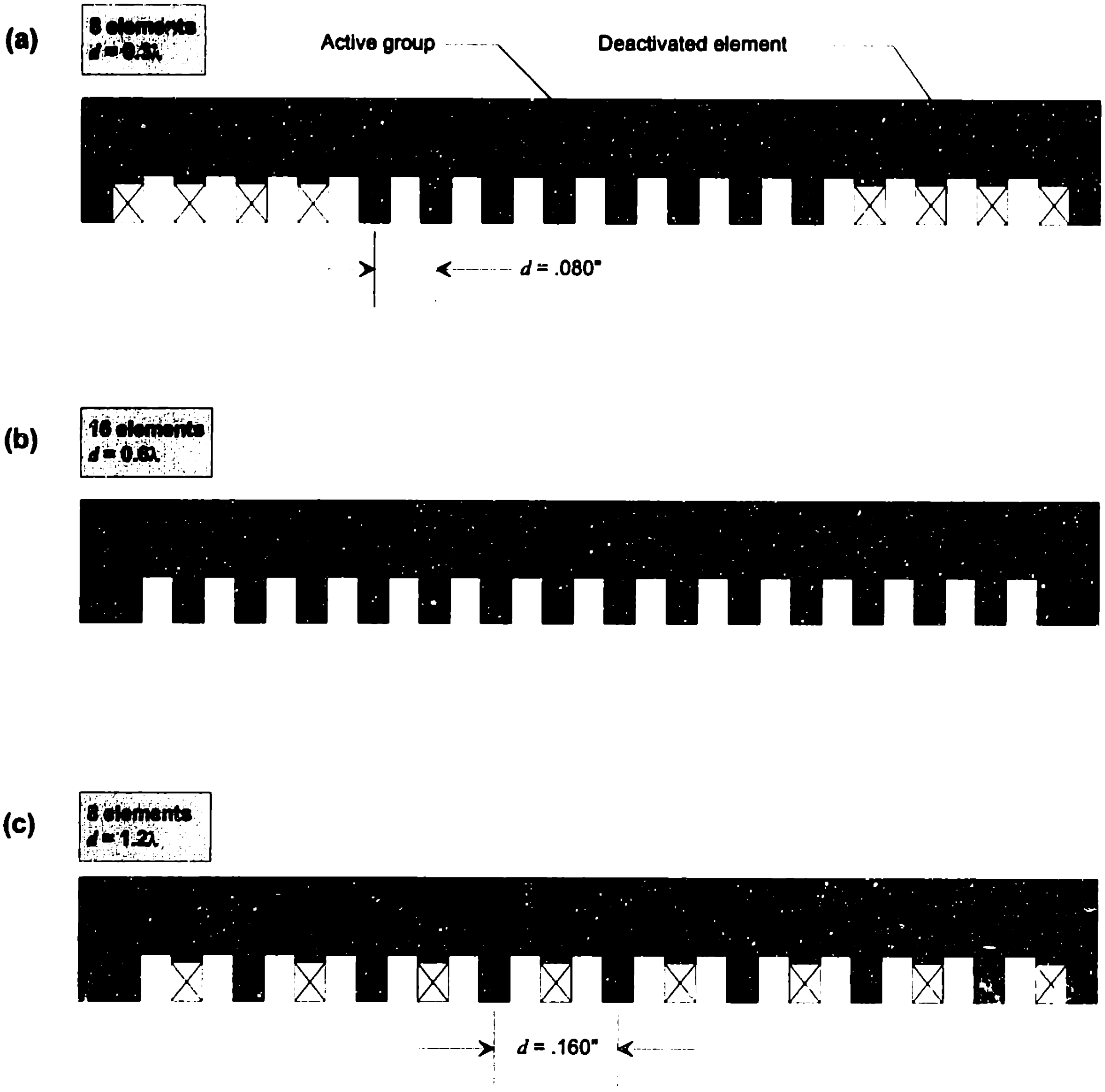

Figure 5.13: Transducer testing configurations for various parameter settings; 16 element sensor with elements spaced at 0.08 in.

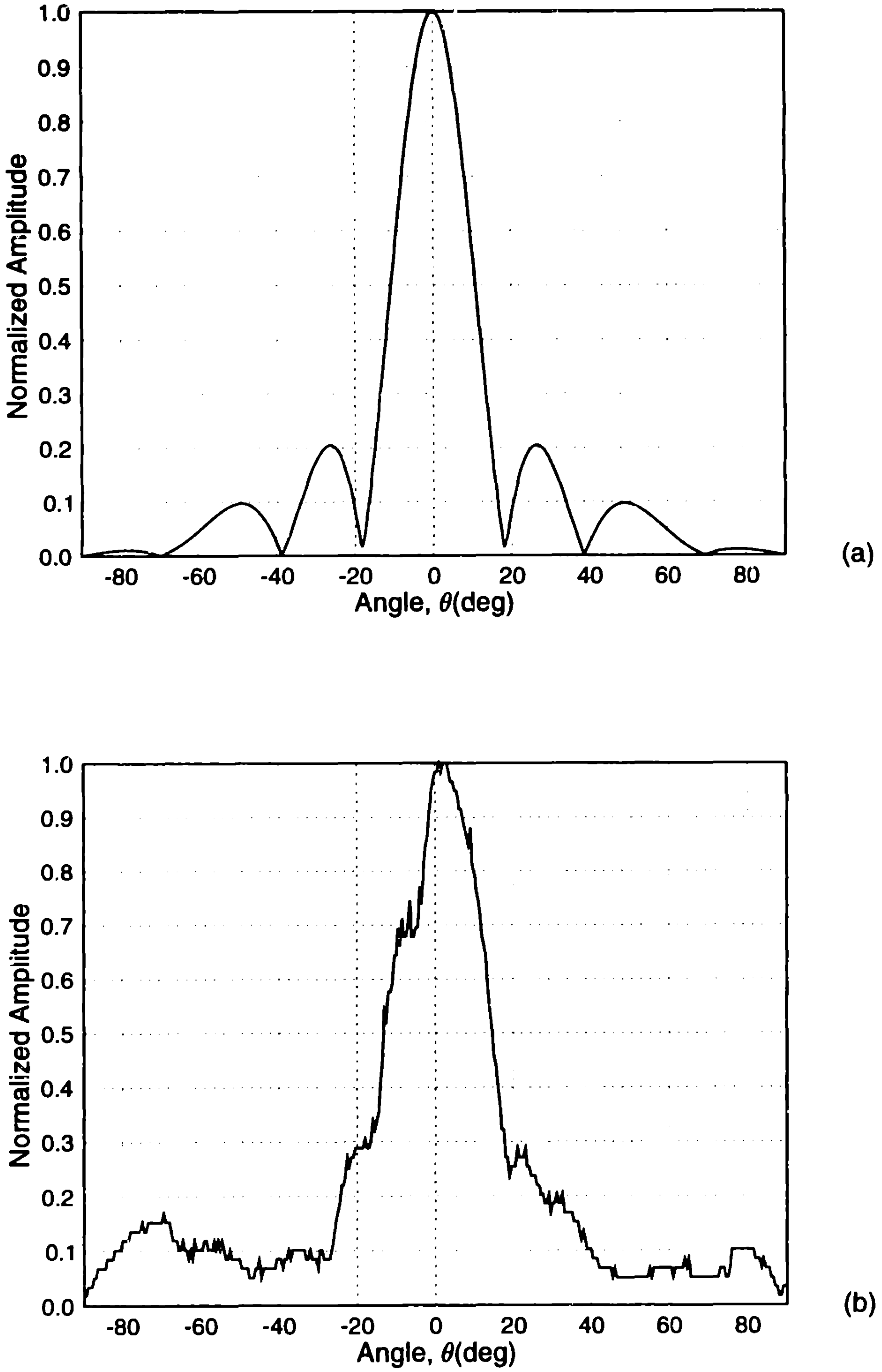

Figure 5.14: Directivity plots: (a) simulated and (b) experimental ($N = 8$, $d = 0.4\lambda$ and $\theta_s = 0°$).

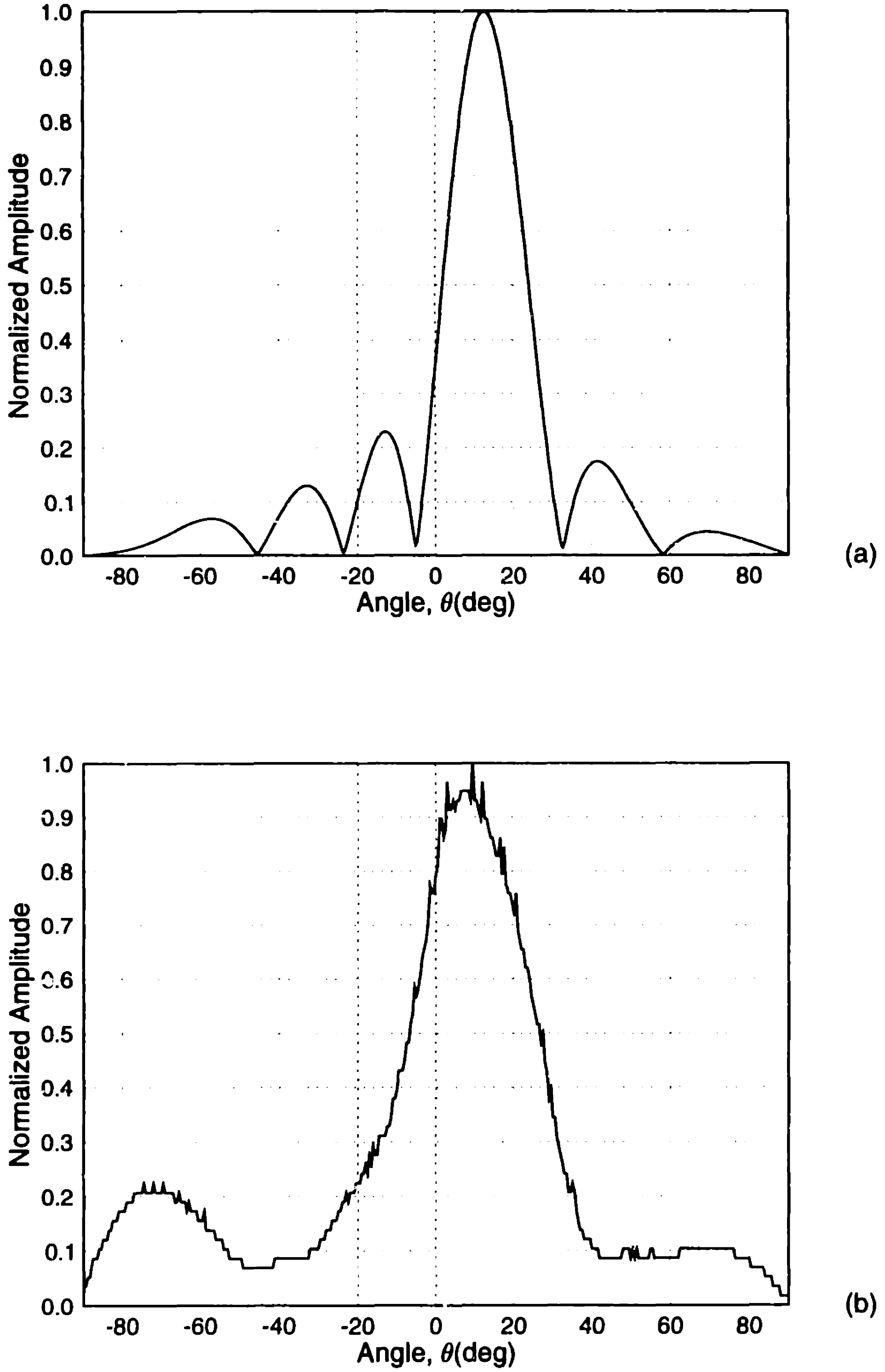

Figure 5.15: Directivity plots: (a) simulated and (b) experimental ($N = 8$, $d = 0.4\lambda$ and $\theta_s = 13°$).

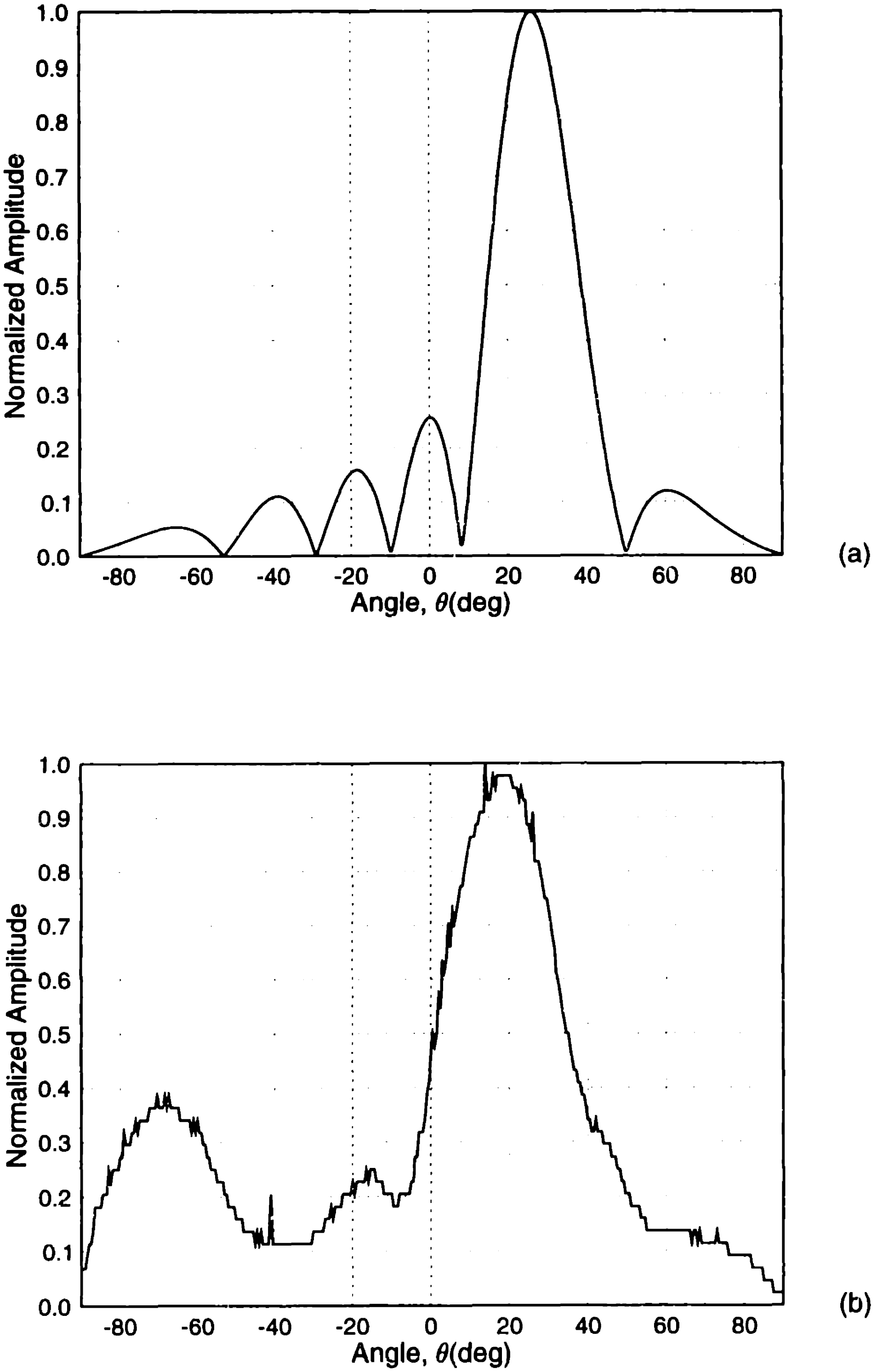

Figure 5.16: Directivity plots: (a) simulated and (b) experimental ($N = 8$, $d = 0.4\lambda$ and $\theta_s = 27°$).

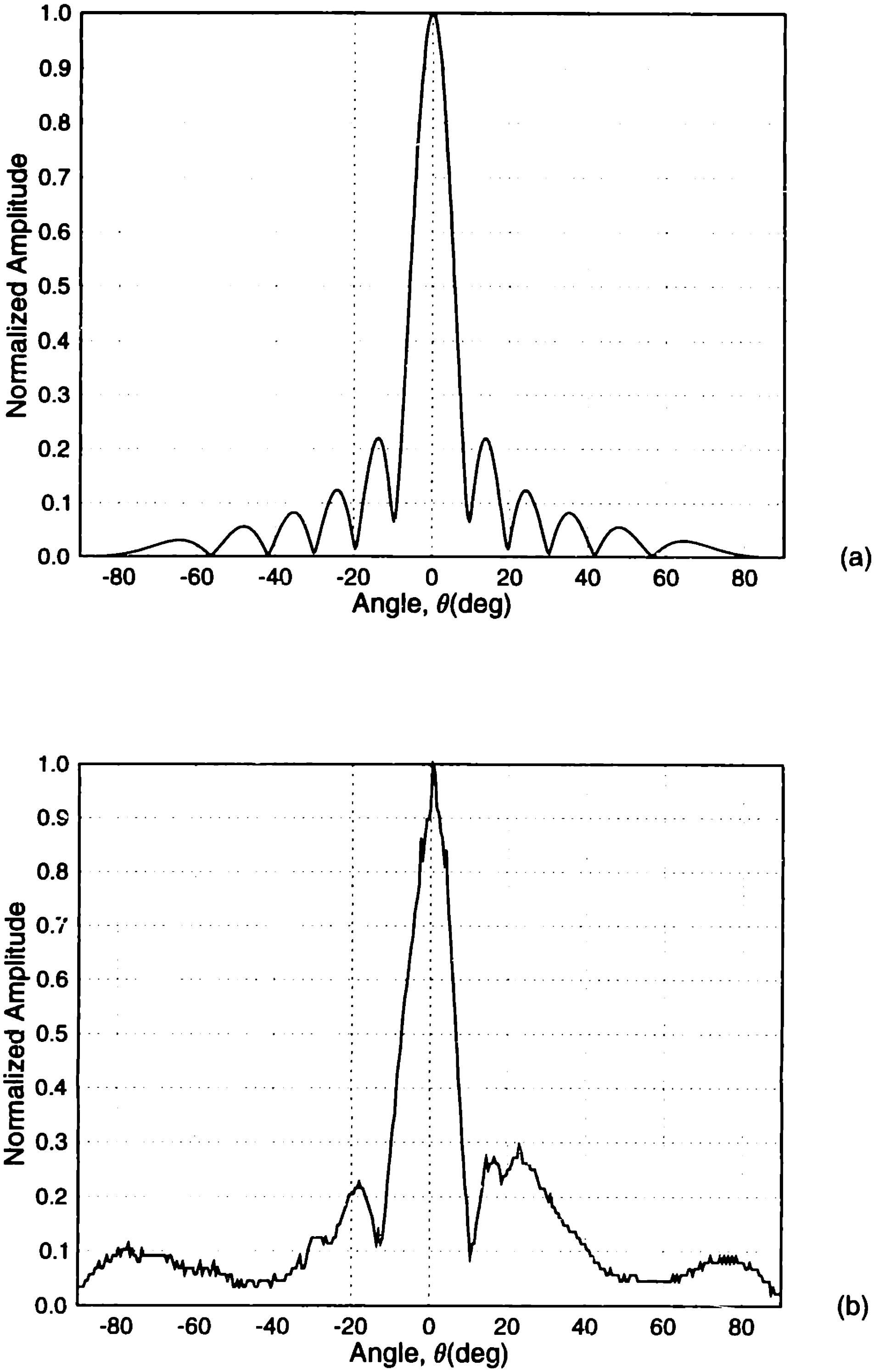

Figure 5.17: Directivity plots: (a) simulated and (b) experimental ($N = 15$, $d = 0.4\lambda$ and $\theta_s = 0°$).

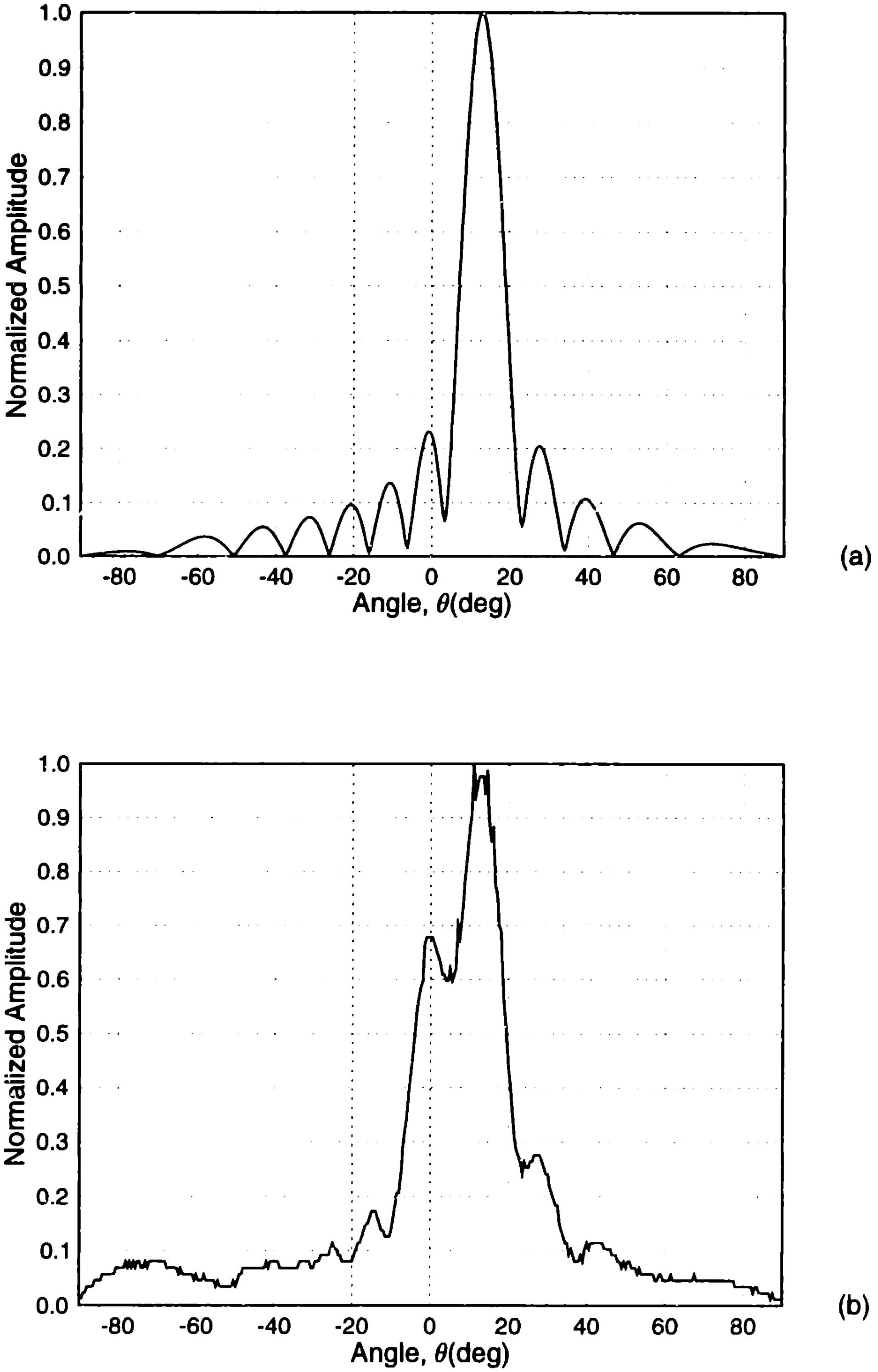

Figure 5.18: Directivity plots: (a) simulated and (b) experimental ($N = 15$, $d = 0.4\lambda$ and $\theta_s = 13°$).

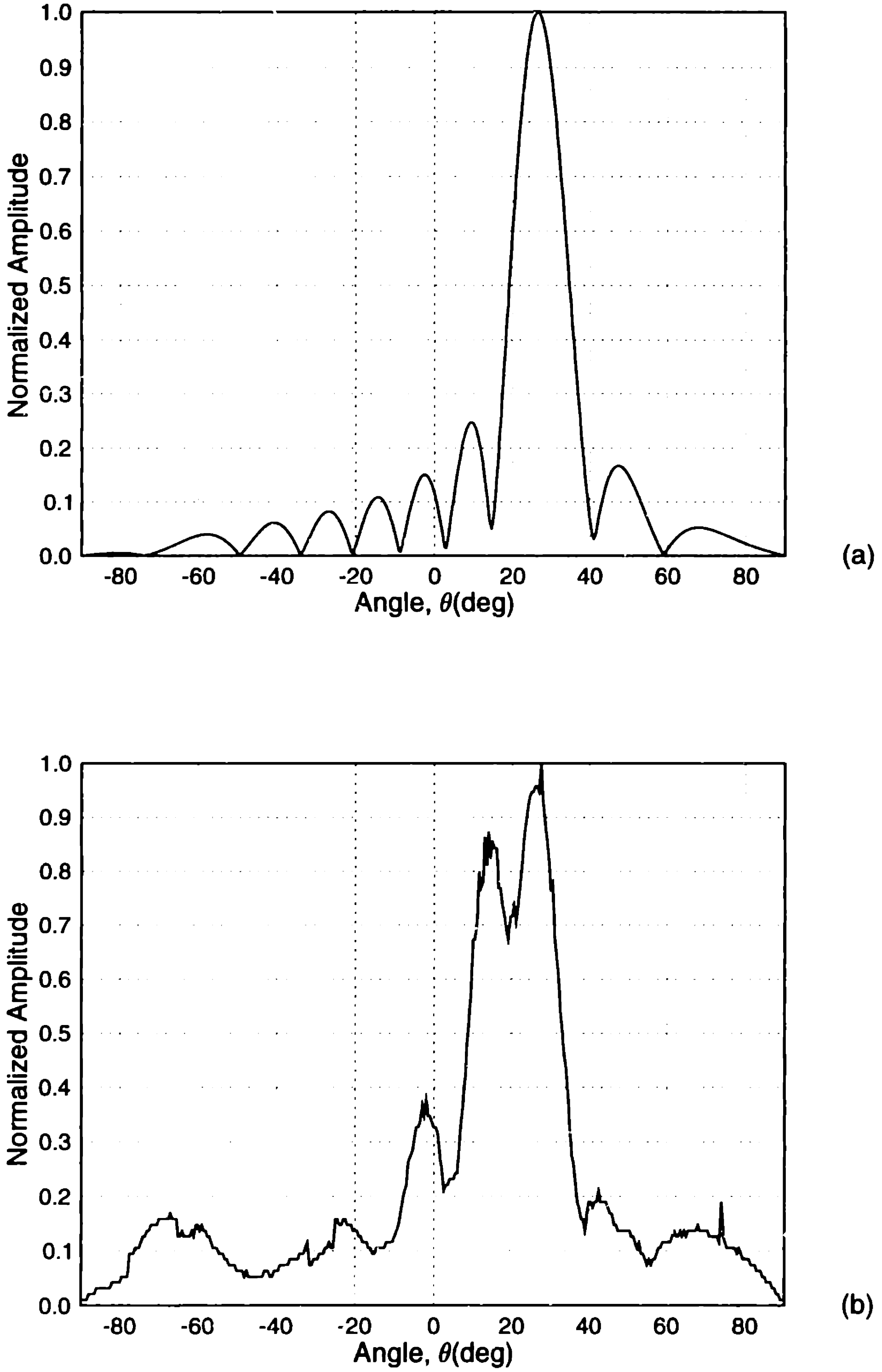

Figure 5.19: Directivity plots: (a) simulated and (b) experimental ($N = 15$, $d = 0.4\lambda$ and $\theta_s = 27°$).

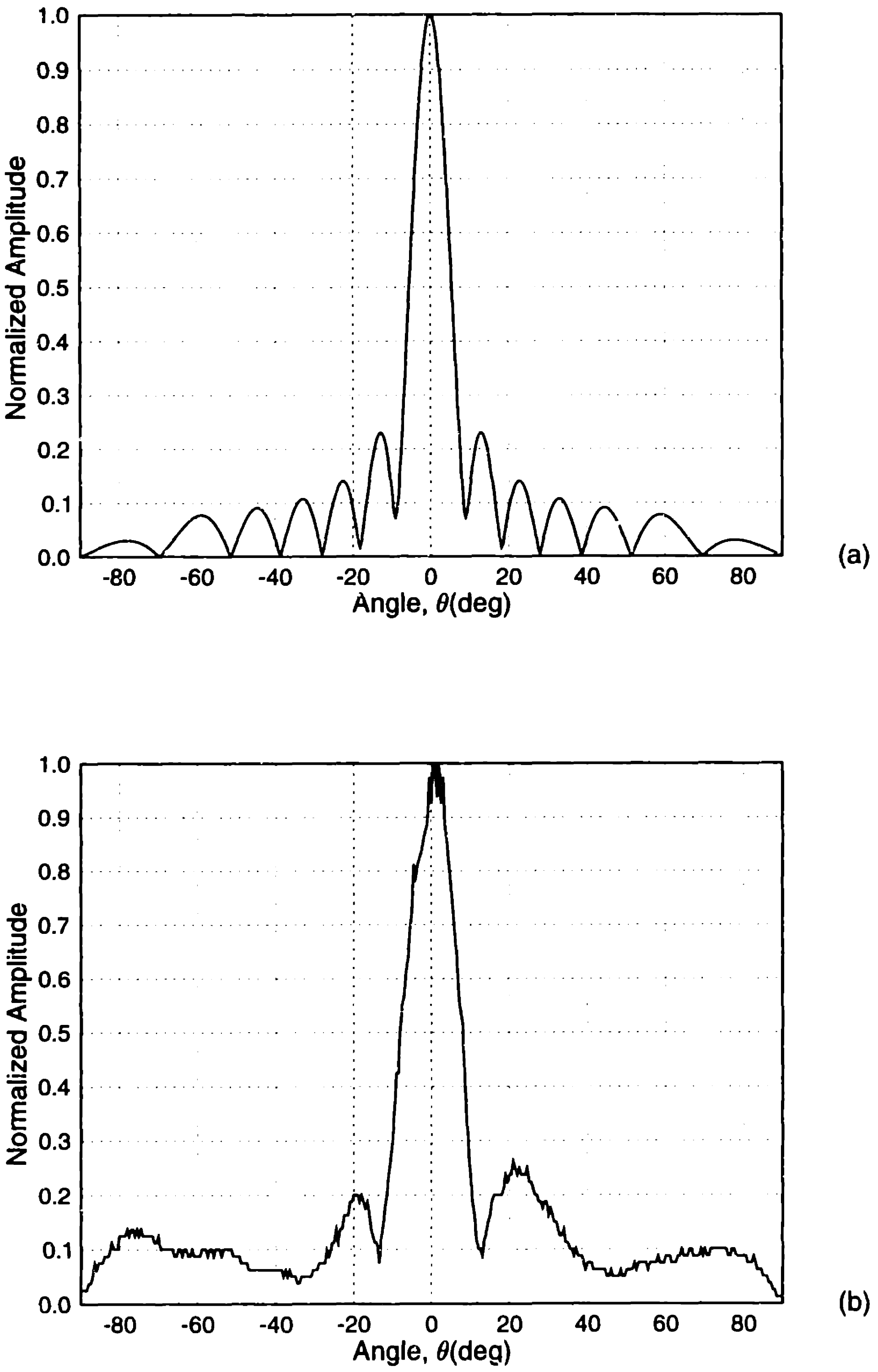

Figure 5.20: Directivity plots: (a) simulated and (b) experimental ($N = 8$, $d = 0.8\lambda$ and $\theta_s = 0°$).

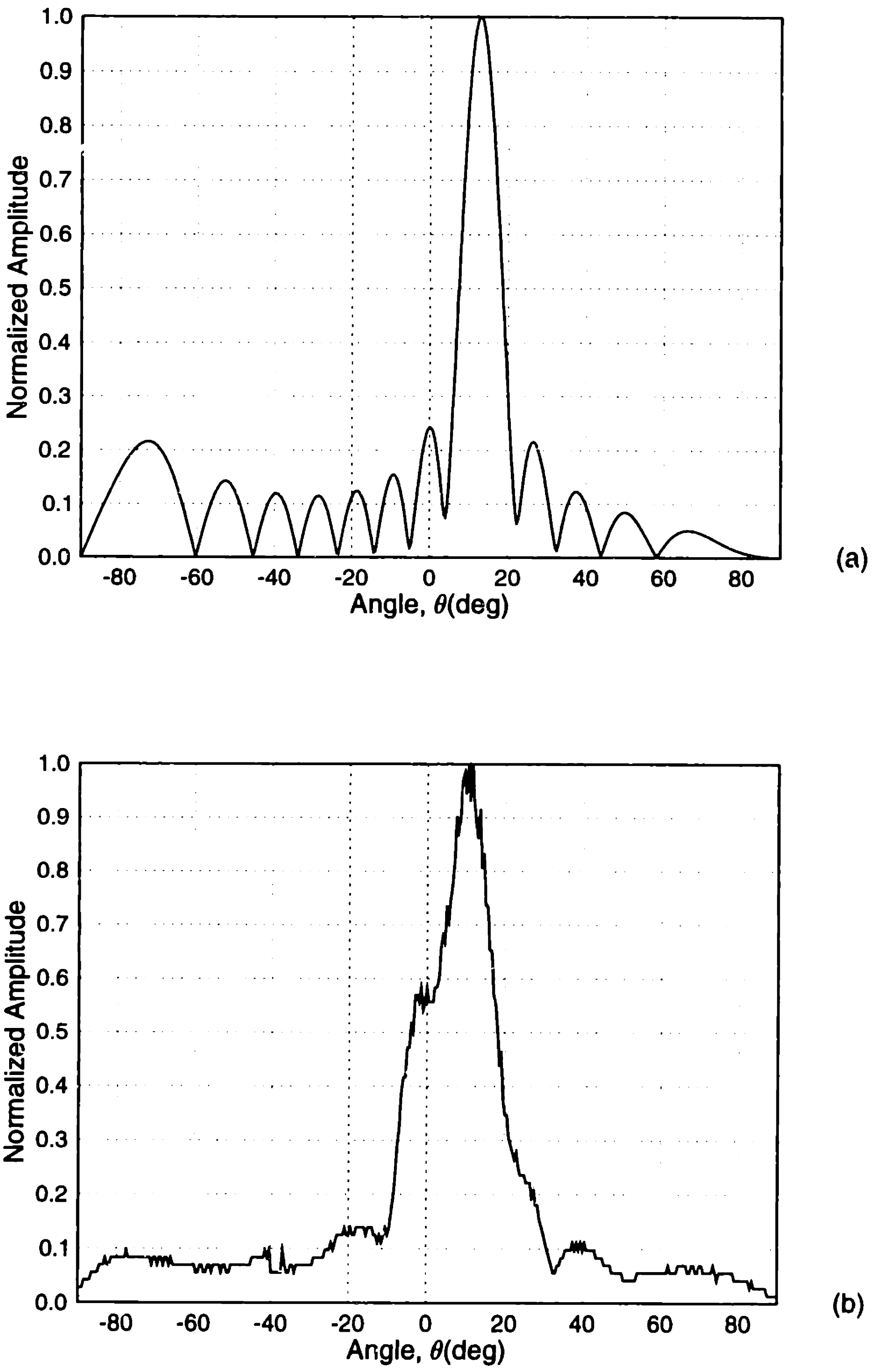

Figure 5.21: Directivity plots: (a) simulated and (b) experimental ($N = 8$, $d = 0.8\lambda$ and $\theta_s = 13°$).

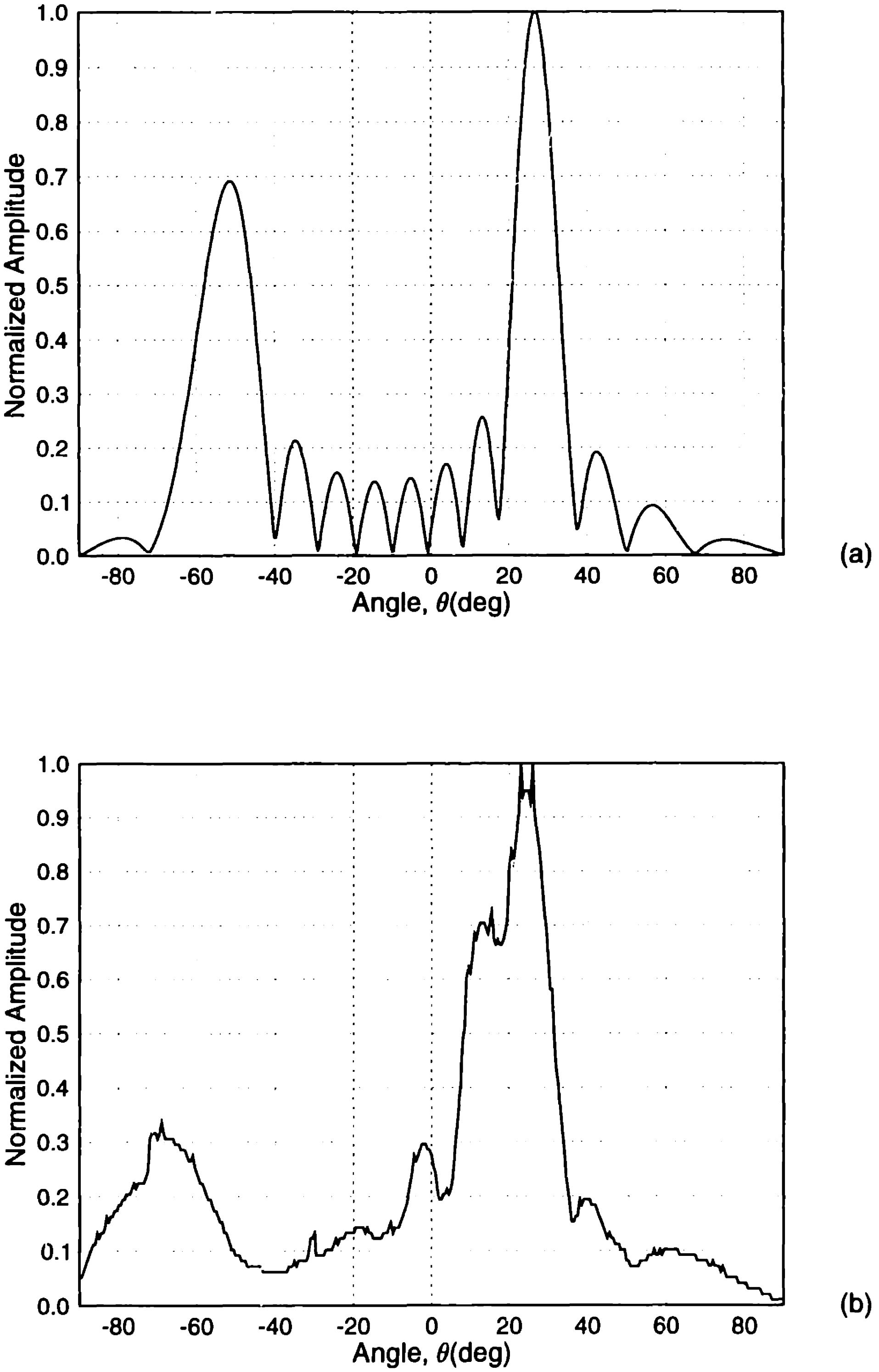

Figure 5.22: Directivity plots: (a) simulated and (b) experimental ($N = 8$, $d = 0.8\lambda$ and $\theta_s = 27°$).

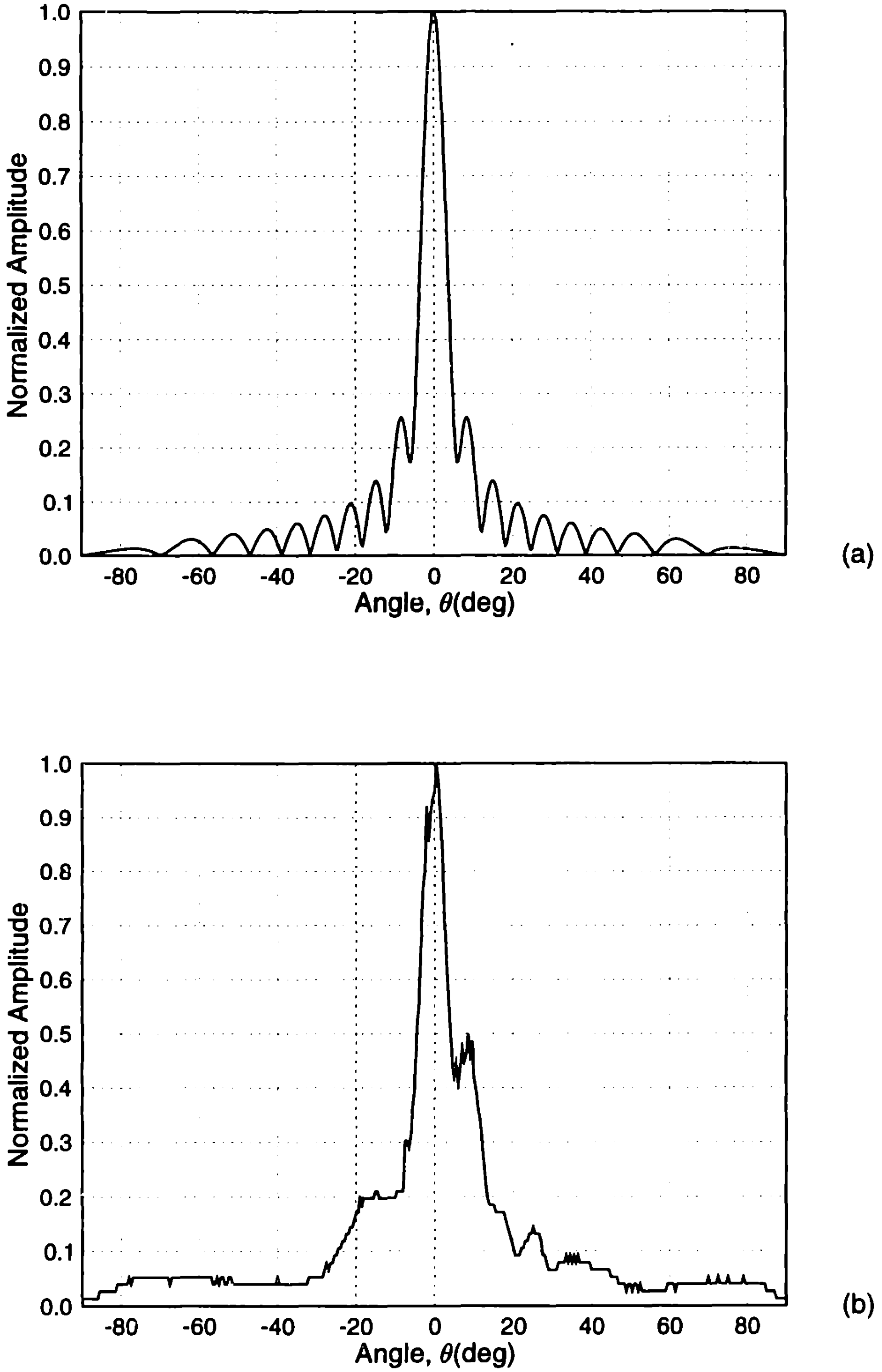

Figure 5.23: Directivity plots: (a) simulated and (b) experimental ($N = 16$, $d = 0.6\lambda$ and $\theta_s = 0^\circ$).

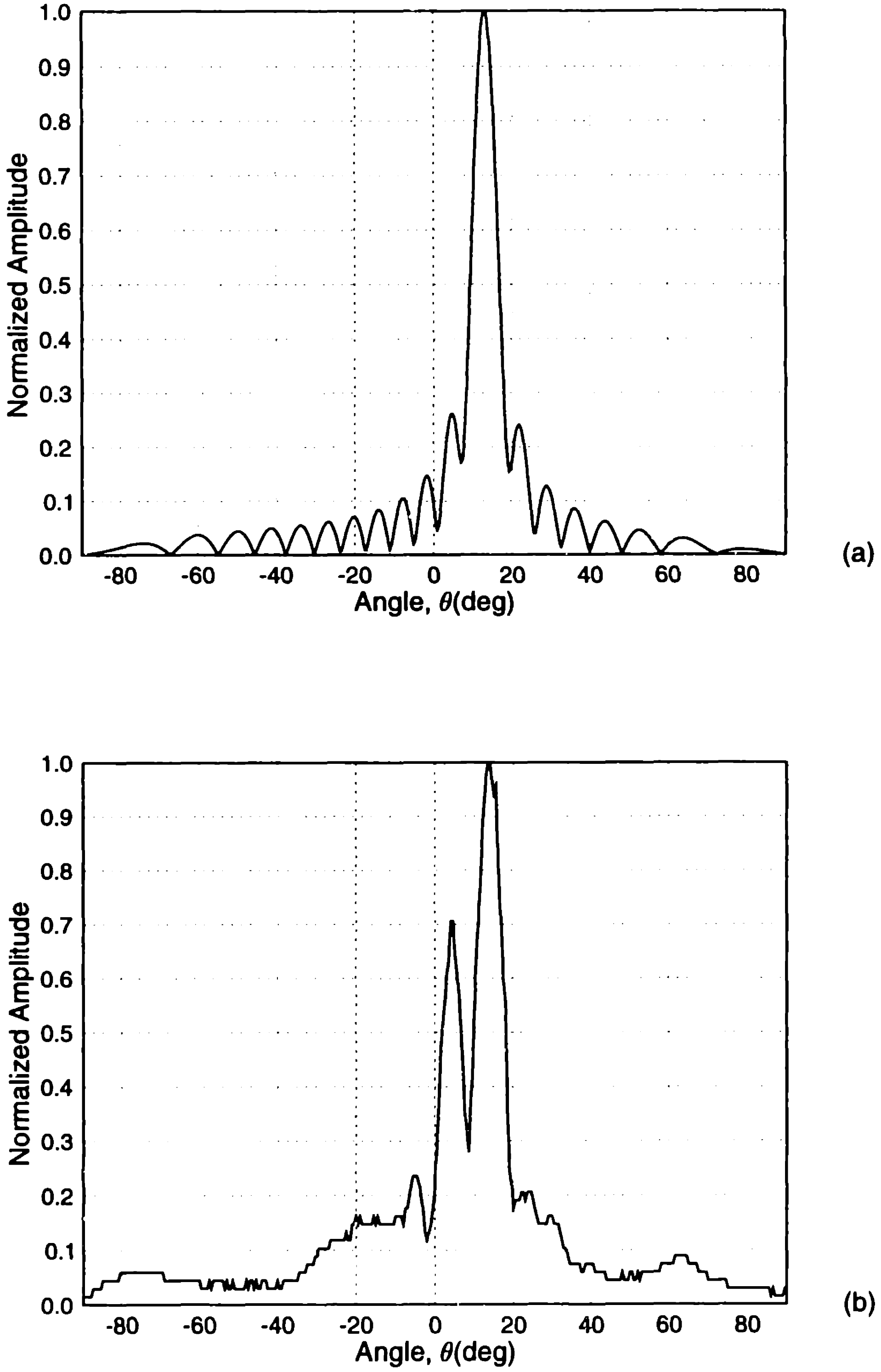

Figure 5.24: Directivity plots: (a) simulated and (b) experimental ($N = 16$, $d = 0.6\lambda$ and $\theta_s = 13°$).

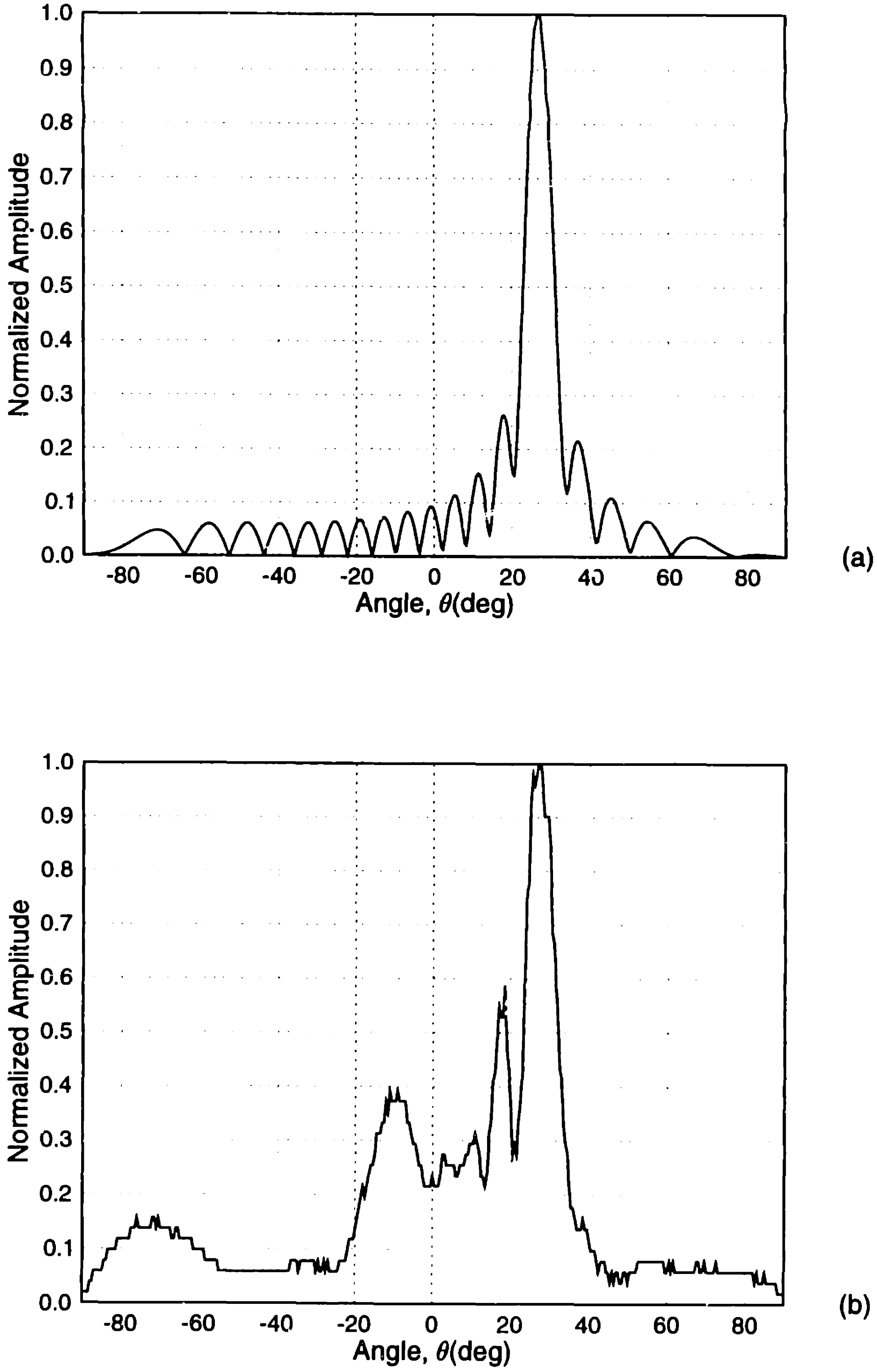

Figure 5.25: Directivity plots: (a) simulated and (b) experimental ($N = 16$, $d = 0.6\lambda$ and $\theta_s = 27°$).

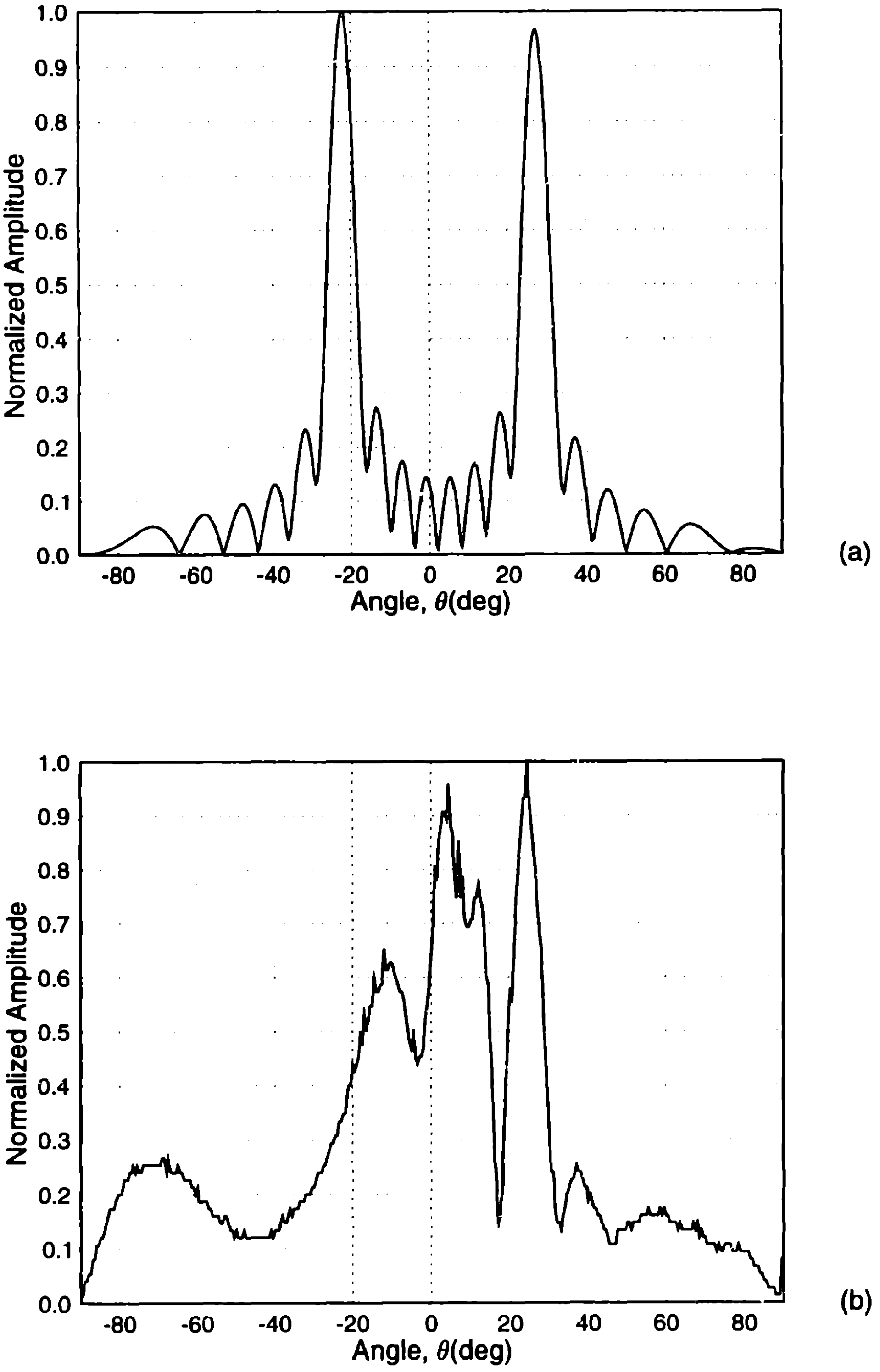

Figure 5.26: Directivity plots: (a) simulated and (b) experimental ($N = 8$, $d = 1.2\lambda$ and $\theta_s = 27°$).

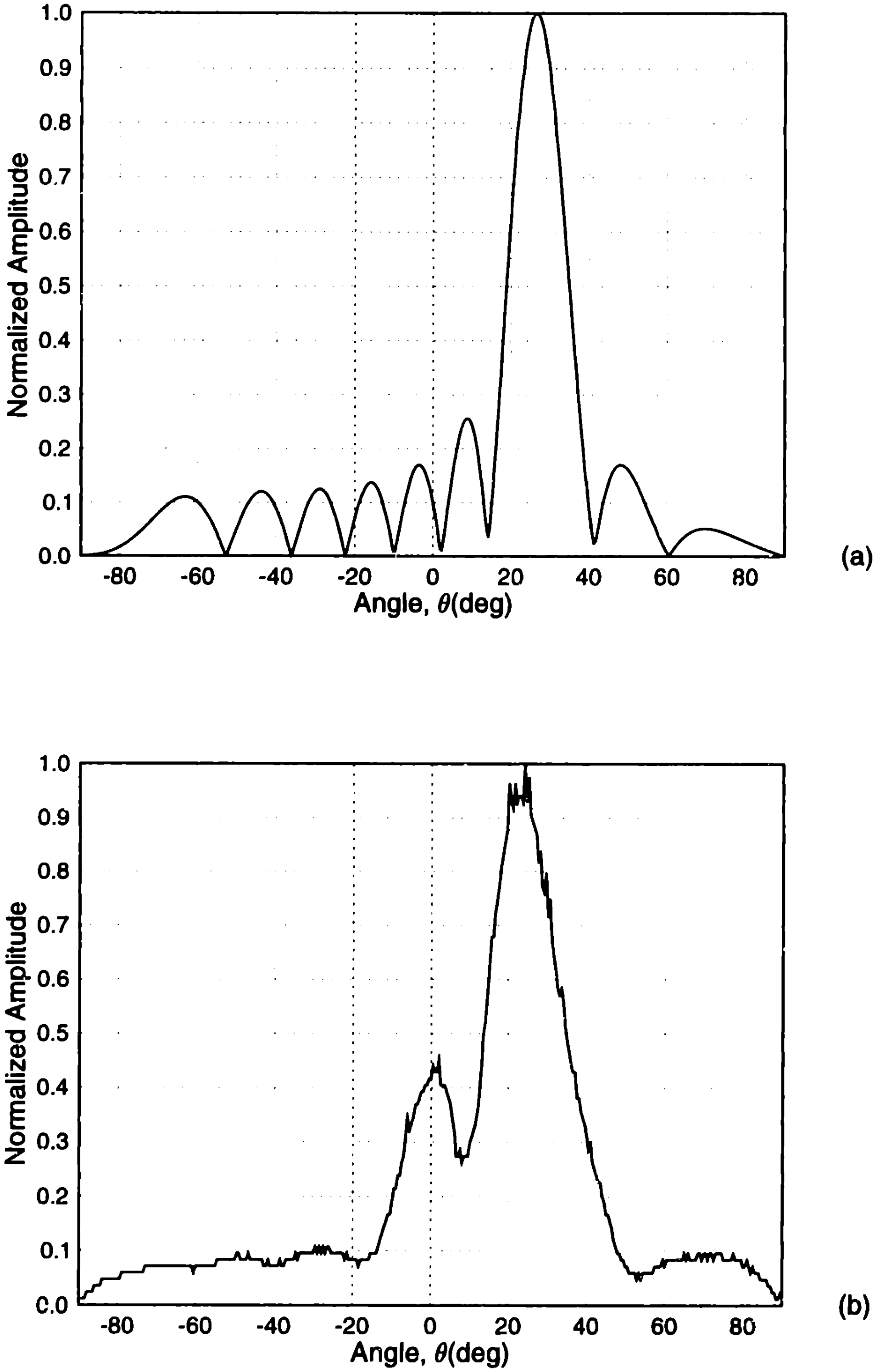

Figure 5.27: Directivity plots: (a) simulated and (b) experimental ($N = 8$, $d = 0.6\lambda$ and $\theta_s = 27°$).

Parameters			***Predicted Results***		***Measured Results***	
d	N	θ_s	θ_s	q_{-3dB}	θ_s	q_{-3dB}
0.4λ	8	0°	0°	15.8°	2°	16°
0.4λ	8	13	12.5	16.5	9.5	$23^{\dagger}$
0.4λ	8	27	25.9	17.8	14	$26^{\dagger}$
0.4λ	15	0	0	8.4	0.5	9.25
0.4λ	15	13	12.9	8.7	11	10.5
0.4λ	15	27	26.6	9.6	27.5	10
0.8λ	8	0	0	8.1	0.75	11
0.8λ	8	13	12.9	8.3	10.5	10.25
0.8λ	8	27	26.6	8.9	24.5	9.75
0.6λ	16	0	0	5.4	0.5	5.75
0.6λ	16	13	12.9	5.5	13.75	5.75
0.6λ	16	27	26.9	6.0	27.25	6.4
1.2λ	8	27	26.9	6.3	24.5	5.75
0.6λ	8	27	26.6	11.7	24	13.75

Table 5.1: Summary of simulated and experimental results for various parameters. († denotes bad result from excessive system or measurement error.)

5.3.5 Discussion

The results collected from these experiments, along with the numerical simulation results, are summarized in Table 5.1. The key results are the steering angle θ_s and the -3dB main lobe width q_{-3dB}. Since it is not possible to obtain the exact crossing points of the main lobe from the experimental plots, the -3dB drop (30% reduction in maximum amplitude) is a more a useful estimate of the beam directivity. The main lobe at -6dB (50%) would yield significant differences from the simulated results due to the interference of other lobes. It should be noted that the q value used in this quantitative comparison is not normalized by pi and therefore is measured in degrees.

There are several important observations that can be made by looking at the previous curves as well as the information summarized above. Overall, the experimental results seem to be in good agreement with the predicted simulation. Both the steering angle and main lobe width at -3dB seem to have good correlation between the simulation and experimentally measured results. The only notable exception is the steering angle in Fig. 5.16. The closest agreement occurs for $d = 0.6\lambda$ and $N = 16$. This is reasonable since increasing the number of elements will reduce the effect of noise and other artifacts in the system. Increasing N also will reduce the cosine effect, so that the desired steering angle will equal the actual steering angle.

The most interesting observation can be drawn from Figs. 5.17— 5.19 and Figs. 5.20—5.22. These figures show that we may obtain virtually the same steering capabilities and beam directivity for only half the required number of elements by simply doubling the spacing between elements. Since the cost of an array increases with the number of channels required, this result implies that fewer elements can be used to achieve the same effect and thus reduce the cost of the system. This is in strong agreeement with the equation for q which implies that if the product of Nd is kept constant, the main lobe width will remain unchanged.

The effect of d is also evident when the same number of channels are used. For example, Figs. 5.14–5.16 and Figs. 5.20–5.22 show that for $N = 8$, q_{-3dB} is reduced by a factor of two when the spacing is doubled from $d = 0.4\lambda$ to $d = 0.8\lambda$. Also note that the same is true for the case when $N = 15$ ($d = 0.4\lambda$) and $N = 16$ ($d = 0.6\lambda$), as shown in Figs. 5.17–5.19 and Figs. 5.23– 5.25. The needle-sharp directivity shown in Fig. 5.23 can only be achieved by increasing the number of elements when $d = \lambda/2$. This would be the type of directivity used in NDE applications that require controlled long distance steering.

Increasing the number of elements while holding d constant shows improved directivity and steering. Figs. 5.14–5.16 and Figs. 5.17--5.19 give testimony to this fact for the case where $N = 8$ and $N = 15$. The steering angles are in much closer agreement with the predicted angles, and the main lobe width is reduced by a factor of 2. A similar effect is seen in Fig. 5.27 and Fig. 5.25.

Fig. 5.26 shows the undesirable case when a large grating lobe exists. Although the experimental result gives good indication of the main lobe, the grating lobe is somewhat shifted and distorted. This is most likely due to additional interference from high-amplitude waves entering the gate due to drift along the time axis. The same interference may have caused similar thickening of the main lobe in other directivities. Nonetheless, the result clearly shows that increasing d beyond a half wavelength will lead to severe grating lobes.

Two phenomenon predicted by the simulation that were not observed experimentally are the downshift in steering angle due to the cosine envelope and the increase in main lobe width for increasing steering angle. It is likely that the sensitivity involved in making these measurements is embedded within the measurement error.

In summary, the following key points can be made:

- Increasing d improves the performance while using the same N.
- Increasing N improved the performance while using the same d.
- The same performance is achieved when d is doubled from 0.4λ to 0.8λ while N is reduced from 15 elements to 8 elements.
- Optimum results are obtained for $N = 16$ and $d = 0.6\lambda$.
- Worst results are obtained when $d >> \lambda/2$, which introduces large grating lobes.
- The effect of vs increasing q for increasing θ_s cannot be verified experimentally due to inherent error and sensitivity in measurement.
- The effect of downshifting in the steering angle due to the cosine envelope was also not evident due to the error in measurement.

Chapter 6

Conclusion

6.1 Summary and Commentary

At the core of this research, several important phased array parameters were investigated both theoretically and experimentally to determine their influence on the ultrasonic beam steering profile. The theoretical work developed by Wooh and Shi provides the backbone of this thesis as it identifies the fundamental parameters which have the greatest influence on the beam directivity, namely the interelement spacing d and the number of elements N.

In order to characterize the directivity, we introduced the term *main lobe sharpness factor*, q, which determines the width of the main lobe. For NDE purposes, particularly for long-distance defect detection, sharp and well directed beam profiles are mandatory. It was found that increasing the number of elements not only sharpens the beam, but also boosts the pressure and widens the aperture. Side lobes will also be suppressed with more elements employed. Larger spacing between elements can also be used to improve the directivity. However, this strategy should be employed up to the theoretical limit of $d = \lambda/2$, at which point grating lobes appear. Although the beam will continue to narrow, the grating lobes will become more pronounced in other directions, making the ultrasound unsteerable.

The experimental program was established to confirm the theoretical findings discussed above and also to perform general steering calibration of various phased array sensors. Testing was done by mounting the phased array onto an aluminum disk which was driven by a step motor. The phased array was programmed through delay-generating software from the PC to steer the beam at a specified angle. The disk was turned to obtain a full directivity of the beam profile. Amplitude for each point along the directivity curve was traced using an immersion receiver focused at the rim of the disk.

Two transducers were fabricated in a slotted fashion allowing for the effect of interelement spacing and number of elements on the beam steering profile to be tested. Experimental results were compared to a numerical model based on the theory. This model computed each element as a point source and applied a cosine envelope to provide more realistic behavior. Quantitative evaluation of the theoretical and experimental results was made by comparing the steering angle θ_s and the -3 dB drop in main lobe width q_{-3dB}.

Overall, the numerical simulation provided good agreement with the experiment. The directivity plots generally gave excellent testimony to the trends expected from the theory. Increasing elements resulted in a sharper directivity. Also, larger spacing produced improved directivity as well. Keeping the product Nd constant, we also observed the same value for the -3 dB drop in q. This result has perhaps the greatest practical implications: the same performance can be expected from an array with half the number of channels by simply doubling the spacing (provided d is not much larger than $\lambda/2$. This is an extremely cost efficient means of maximizing the performance.

The experimental results also showed evidence of grating lobes when the value of d exceeded 0.5λ. However, the expected downshift in steering angle due to the cosine envelope was not witnessed. It was also not possible to conclude that an increase in θ_s would lead to an increase in q. These features were probably not observed due to the combined effect of both system and measurement errors. With an increased system sensitivity it would be more likely to be able to detect both the downshift as well as the effect of steering angle.

6.2 Recommendations for Future Work

New roads must be paved for direct applications of phased array transducers to NDE and civil infrastructure. Having successfully proven through experimental verification the beam steering behavior, the future work should be directed towards implementing phased arrays in real applications such as welds, girders, dimensional loss due to corrosion, rail, bolted connections, and other members prone to damage.

In this regard, the system developed in this thesis would require some modification. Since the phased array transducer and supporting electronics was designed specifically for the purpose of confirming theory within a rather narrow range of implementation, it may not be suitable for testing under practical conditions. Consequently, there are several suggestions for enhancement:

- Improve the delay range and resolution
- Reduce the pulse width
- Increase the array aperture
- Employ higher frequency transducers
- Use matching layers
- Investigate new piezo-materials

Since the circuitry dictates the maximum steering angle as well as the angular resolution, high delay ranges and enhanced delay resolution are essential. For imaging purposes, particularly in long-distance NDE applications, a resolution of 0.1 ns and a range of 50 μsec would be recommended for excellent beam steering and control. This is entirely within the limits of current technology. A reduced pulse width will also improve the sensitivity of the signal and reduce the ring-down. A programmable pulse width ranging from 20 to 200 ns would be sufficient for matching to typical transducer frequencies.

This thesis introduced a new method for fabricating phased arrays quickly and reliably using a slotted technique. This resulted in perfectly isolated elements. However, further exploration of the effect of backing and matching layers should be done for optimum bandwidth and sensitivity. It is highly recommended that these effects be modeled using either a Mason or KLM approach to save time in fabricating transducers by trial and error.

Several relatively straightforward modifications of the transducer would lead to immediate improvement in performance. An increased aperture using more elements will provide excellent steering capability and also increase the near field, allowing for a greater range of focusing. Upgrading to 32 elements would be a good compromise in sharpening the directivity at large angles without a tremendous increase in pulser/receiver and delay channels. Also, higher frequency transducers, say 5–10 MHz will be required for practical NDE inspections in steel components.

Although PZT-5A proved to be a reliable ceramic in terms of its machinability and acoustic performance in this work, it is worth exploring new materials. Piezocomposites give excellent efficiency in transmission. PVDF is highly sensitive and works well in reception. The combination of these two materials into a dual-element transducer would give the best results for broadcasting and receiving.

Clearly the results obtained from this work show promise and direction for experimentally verifying the theoretical phased array pressure field. However, it may be interesting to perform a more comprehensive testing of other parameters in the future. It was assumed that element width had no influence on the directivity. Extreme cases, such as when $a \ll \lambda$ and $a \gg \lambda$, may be useful for comparing the tradeoffs between excellent directivity and steering versus acoustic power. The concept of effective element width should definitely be explored further to characterize crosstalk between elements. The elevation dimension as well as the thickness of the element should also be studied over a wide range of angles. This research should also be extended to planar arrays which will allow full volumetric imaging within a material. The effects of these parameters on combined focusing and steering must also be studied.

Bibliography

1. Achenbach, J. D., I. N. Komsky, Y. C. Lee, and Y. C. Angel (1992), "Self-calibrating ultrasonic technique for crack depth measurement," *Journal of Nondestructive Evaluation*, **11**(2), 103–107.

2. Armitage, A. D., N. R. Scales, P. J. Hicks, P. A. Payne, Q. X. Chen (1995), "An integrated array transducer receiver for ultrasound imaging," *Sensors and Actuators*, **A 46–47**, 542–546.

3. ASNT (1991), *Nondestructive Testing Handbook*, P. McIntire ed., American Society for Nondestructive Testing.

4. AWS (1985), *Guide for the Nondestructive Inspection of Welds*, ANSI/AWS B1.10-86, American Welding Society.

5. Beardsley, B., M. Peterson, and J. D. Achenbach (1995), "A simple scheme for self-focusing of an array," *Journal of Nondestructive Evaluation*, **14**(4), 169–179.

6. Berthelot, J.-M., M. Ben Souda, and J. L. Robert (1994), "Identification of signals in the context of acoustic emission in concrete," *Journal of Nondestructive Evaluation*, **13**(2), 63–73.

7. Bisbee, L. and S. Burns (1994), "Enhanced ultrasonic examination of feedwater pipe-to-nozzle welds," *Nuclear Plant Journal*, March–April 1994, 42–53.

8. Buchanan, M.T. and K. Hynynen (1994), "Design and experimental evaluation of an intracavity ultrasound phased array system for hyperthermia", *IEEE Transactions on Biomedical Engineering*, **41**(12), December, 1178–1187.

9. Charlesworth, J.P. and J.A.G. Temple (1989), *Ultrasonic Time-of-Flight Diffraction*, Research Studies Press LTD., Somerset, England.

10. Chinn, D.J. (1994), *Long-distance ultrasonic testing of steel structures*, Heron, (1).

11. De Silets, C. S. (1978), "Transducer arrays suitable for acoustic imaging," *Ph.D. Dissertation*, Stanford University, Stanford, CA, 1978.

12. Ditchburn, R.J., S.K. Burke and C.M. Scala (1996), "NDT of welds: state of the art," *NDT&E International*, **29**(2), 111–117.

13. Doyle, P. A. and C. M. Scala (1978), "Crack depth measurement by ultrasonics: a review," *Ultrasonics*, July, 164–169.

14. Dufour, I., D. Placko, and M. Geoffroy (1995), "Active shielding of eddy current sensors: a method to focus the magnetic field in order to improve lateral resolution and coupling coefficient," *NDT&E International*, 225–233.

15. FHWA (1986), *Nondestructive Testing Methods for Steel Bridges: Participants Training Manual*, Federal Highway Administration, U. S. Department of Transportation, FHWA-HI-88-006, June, 1986.

16. Fisher, J. W. (1984), *Fatigue and Fracture in Steel Bridges – Case Studies*, John Wiley & Sons, New York, NY.

17. Hatfield, J. V., N. R. Scales, A. D. Armitage, P. J. Hicks, Q. X. Chen, and P. A. Payne (1994), "An integrated multi-element array transducer for ultrasound imaging," *Sensors and Actuators A*, (41–42) 167–173.

18. Howard, B. D. (1994), "Focused array transducer system (FATS): ultrasonic testing applications at the Department of Energy's Savannah River Site," *Review of Progress in Quantitative Nondestructive Evaluation*, **13**, D. O. Thompson and D. E. Chimenti eds., Plenum Press, New York, 1053–1059.

19. Hsu, David K. and T.C. Patton (1993), "Development of ultrasonic inspection for adhesive bonds in aging aircraft," *Materials Evaluation*, 1390–1397.

20. Hsu, D. K., A. M. Ayres, M. Meng and G. Ma (1994), "Simultaneous determination of ultrasonic velocity, plate thickness and wedge angle using one-sided contact measurements," *NDT & E International*, **27**(2), 75–82.

21. Jessop, T. J., P. J. Mudge and J. D. Harrison (1989), *Ultrasonic Measurement of Weld Flaw Size*, Transportation Board, Report No. 242, Dec. 1989.

22. Kino, G. S. (1979), "Acoustic imaging for nondestructive evaluation," *Proc. IEEE*, **67**, April, 510–525.

23. Krautkämer, J. and H. Krautkrämer (1990), *Ultrasonic Testing of Materials*, 4th ed., Springer-Verlag, New York.

24. Lemon, D. K. and G. J. Posakony (1980), "Linear array technology in NDE applications," *Materials Evaluation*, July, 34–37.

25. Lethkiecq, M., C. Pejot, M. Berson, P. Guillemet and A. Roncin (1994), "An ultrasonic array-based system for real-time inspection of carbon-epoxy composite plates," *NDT & E International*, **27**(6), 311–315.

26. Lockwood, G.R., Pai-Chi Li, M. O'Donnell and F.S. Foster (1996), "Optimizing the radiation pattern of sparse periodic linear arrays", *IEEE Transactions on Ultrasonics, Ferroelectrics, and Frequency Control*, **43**(1), January, 7–14.

27. Lovejoy, A., P. Pedrick, A. Doran, T. A. Delchar, J. A. Mills, and A. Stamm (1995), "A novel 8-bit ultrasound phased-array controller for hyperthermia applications," *Ultrasonics*, **33**(1), 69–73.

28. Macovski, A. (1979), "Ultrasonic imaging using arrays," *Proc. IEEE*, **67**, April, 484–495.

29. Mak, D. K. (1985), "Ultrasonic methods for measuring crack location, crack height, and crack angle," *Ultrasonics*, September, 223–226.

30. Mak, D.K. (1991), "Ultrasonic imaging analysis using a multi-transducer technique," *Ultrasonics*, **29**, 308–311.

31. Masnata, A. and Sunseri, M. (1996), "Neural network classification of flaws detected by ultrasonic means," *NDT&E International*, 87–93.

32. McCurdy, M. (1989), "Ultrasonic inspection of pin assemblies in bridges," *Materials Evaluation*, December 1989, 1340–1341.

33. McNab, A. and M. J. Campbell (1987), "Ultrasonic phased arrays for nondestructive testing," *NDT International*, **20**(6), December, 333–337.

34. McNab, A. and I. Stumpf (1986), "Monolithic phased array for transmission of ultrasound in NDT ultrasonics," *Ultrasonics*, **24**, May, 148–155.

35. McNab, A. and J. Thomson (1995), "An eddy current array instrument for application to ferritic welds," *NDT&E International*, 103–112.

36. Mo, J.H., J.B. Fowlkes, A.L. Robinson and P.L. Carson (1992), "Crosstalk reduction with a diaphragm structure for intergrated ultrasound transducer arrays," *IEEE Transactions on Ultrasonics, Ferroelectrics, and Frequency Control*, **39**(1), January, 48–53.

37. Ogura, Y. (1983), "Height determination studies for planar defects by means of ultrasonic testing," *The Non Destructive Testing Journal, Japan*, **1**(1), 22–29.

38. Persson, H.W. and C. H. Hertz (1985), "Acoustic impedance matching of medical ultrasound transducer", *Ultrasonics*, March, 83–89.

39. Rosenthal, D. and J. Trolinger (1995), "Holographic Nondestructive Testing," *Materials Evaluation*, December, 1353–1355.

40. Scales, N.R., P.J. Hicks, A.D. Armitage, P.A. Payne, Q.X. Chen and J.V. Hatfield (1994) "A programmable multi-channel CMOS pulser chip to drive ultrasonic array transducers," *IEEE Journal of Solid-State Circuits*, **29**(8), August, 992–994.

41. Scalzi, J. B., K. P. Chong and W. Dillon (1990), "Overview of nondestructive evaluation in NSF," *Review of Progress in Quantitative Nondestructive Evaluation*, **9**, D. O. Thompson and D. E. Chimenti eds., Plenum Press, New York, 1921–1926.

42. Schueler, C. F. and H. Lee (1984), "Fundamentals of digital ultrasonic imaging," *IEEE Transactions on Sonics and Ultrasonics*, **SU-31**(4), July 1984, 195–217.

43. Schwartz, H.-P. (1987), "Development of a divided-ring array for three-dimensional beam steering in ultrasonic nondestructive testing: Theoretical and experimental results of a prototype," *Materials Evaluation*, August 1987, 951–957.

44. Selfridge, A.R., G.S. Kino and B.T. Khuri-Yakub (1980), "A theory for the radiation pattern of a narrow-strip acoustic transducer", *Appl. Phys. Lett.*, **37**(1), July, 35–36.

45. Silk, M. G. (1984), *Ultrasonic Transducerts for Nondestructive Testing*, Adam Hilger Ltd, Bristol.

46. Sison, M., J.C. Duke, Jr., G. Clemena and M.G. Lozev (1996), "Acoustic Emission: a tool for the bridge engineer," *Materials Evaluation*, August, 888-900.

47. Smith, S.W., O.T. Von Ramm, M.E. Haran and F.L. Thurstone (1979), "Angular response of piezoelectric elements in phased array ultrasound scanners", *IEEE Transactions on Sonics and Ultrasonics*, **SU-26**(3), May, 185–191.

48. Smith, S.W., H.G. Pavy, Jr. and O.T. Von Ramm (1991), "High-speed ultrasound volumetric imaging system—Part I: Transducer design and beam steering", *IEEE Transactions on ultrasonics, ferroelectrics, and frequency control*, **38**(2), March, 100–108.

49. Solomon, K., M. Luttrell and J. Long (1994), "The use of focused array transducers for improved titanium and other billet inspections," *Review of Progress in Quantitative Nondestructive Evaluation*, **13**, D. O. Thompson and D E. Chimenti eds., 1069–1074.

50. Supertex, Inc. (1996), "High Voltage Integrated Circuits and DMOS transistors," *Databook 1996*, Sunnyvale, CA, 3-29—3-32.

51. Sutton, J. L. (1979), "Underwater acoustic imaging," *Proc. IEEE*, **67**, April, 554–566.

52. Thollon, F., B. Lebrun, N. Burais and Y. Jayet (1995), "Numerical and experimental study of eddy current probes in NDT of structures with deep flaws," *NDT&E International*, 97–102.

53. Turnbull, D.H. and F.S. Foster (1991), "Beam steering with pulsed two-dimensional transducer arrays", *IEEE Transactions on Ultrasonics, Ferroelectrics, and Frequency Control*, **38**(4), July, 320–333.

54. Turnbull, D.H. and F.S. Foster (1992), "Fabrication and characterization of transducer elements in two-dimensional arrays for medical ultrasound imaging", *IEEE Transactions on Ultrasonics, Ferroelectrics, and Frequency Control*, **39**(4), July, 464–475.

55. United States Department of Transportation (USDOT, 1985), Federal Highway Administration, Secretary of Transportation: Report to Congress: The Status of the Nation's Highways: Condition and Performance, Technical Report Senate Document 99-6, U.S. Government Printing Office, Washington, D.C..

56. Von Ramm, O.T. and S.W. Smith (1983), "Beam steering with linear arrays", *IEEE Transactions on Biomedical Engineering*, **BME-30**(8), August, 438–452.

57. Weyman, A. E. (1994), *Principles and Practice of Echocardiography*, 2nd ed., Lee & Febiger, Philadelphia.

58. Wooh, S. C. and I.M. Daniel (1991), "Mechanical characterization of a unidirectional composite by ultrasonic methods," *J. of Acoust. Soc. Am.*, **90**(6), December, 3248–3253.

59. Wooh, S. C. and I.M. Daniel (1994), "Three-dimensional ultrasonic imaging of defects and damage in composite materials," *Materials Evaluation*, 1199–1206.

60. Wooh. S. C. (1995), "Role of NDE in civil infrastructure condition assessment'," present and future, Keynote Lecture, *International Workshop for Application of NDT Technology for Failure Prevention*, Jointly organized by Korean Society for Nondestructive Testing (KSNT) and Research Institute of Mechanical Technology (RIMT) of Pusan National University, Oct. 18–20.

61. Wooh, S.C. and A. Clay (1997), "High-speed monitoring of surface defects in rail tracks using ultrasonic Doppler effect," *Review of Progress in Quantitative Nondestructive Evaluation,* D. O. Thompson and D. E. Chimenti eds., Plenum Press, New York, 1997.

62. Wooh, S.C., A.C. Clay and C. Wei (1997), "Ultrasonic phased array transducers for nondestructive evaluation of steel structures", SEM Spring Conference, Bellevue, WA, Society for Experimental Mechanics, June 2-4, 1997.

63. Wooh, S.C. and Y. Shi (1997), "Optimization of ultrasonic phased arrays, Review of Progress in Quantitative Nondestructive Evaluation", San Diego, CA, 1997.

64. Wooh, S.C. and Y. Shi (1997), "Influence of phased array element size on beam steering behavior, *Ultrasonics*, accepted for publication.

65. Wüstenberg, H., B. Rotter, H. P. Klanke, and D. Harbecke (1993), "Ultrasonic phased arrays for nondestructive inspection of forgings," *Materials Evaluation*, June, 669–672.